A METHOD OF MOMENTS APPROACH FOR THE DESIGN OF RF COILS FOR MRI

by

Aghogho Obi

A Dissertation
Submitted to the Faculty
of the
WORCESTER POLYTECHNIC INSTITUTE
in partial fulfillment of the requirements for the
Degree of Doctor of Philosophy
in
Electrical and Computer Engineering

Aghogho Obi
March 1st, 2008

APPROVED:

Prof. Reinhold Ludwig, Research Advisor, ____________________
Electrical and Computer Engineering Department

Prof. Sergey Makarov, ____________________
Electrical and Computer Engineering Department

Prof. John M. Sullivan Jr., ____________________
Mechanical Engineering Department

Prof. Gene Bogdanov, ____________________
Electrical and Computer Engineering Department

Dr. Rosti Lemdiasov, ____________________
InsightMRI LLC

Abstract

Magnetic Resonance Imaging (MRI) is a widely used soft-tissue imaging modality that has evolved over the past several years into a powerful and versatile medical diagnostic tool capable of providing in-vivo diagnostic images of human and animal anatomies. Current research efforts in MRI system design are driven by the need to obtain detailed high resolution images with improved image signal-to-noise ratio (SNR) at a given magnetic field strength. Invariably, this requirement demands the development of high performance MRI radio frequency (RF) coils. However, the complexities and stringent requirements of modern clinical MRI systems necessitate the development of new modeling methodologies for the design of high performance RF coils.

This dissertation addresses this need by developing a distinct Method of Moments (MoM) modeling approach suitable for the simulation of RF coils loaded with biological tissues. The unique implementation utilizes two distinct basis functions in order to collectively describe the surface current density on the RF coil, and the sum of the volume current density and the displacement current density in the associated biological tissue. By selecting basis functions with similar properties to the actual physical quantities they describe, we avoided spurious solutions normally associated with MoM based implementations. The validity of our modeling method was confirmed by comparisons with analytical solutions as well as physical measurements, yielding good agreement.

Furthermore, we applied the MoM based modeling method in the design and development of a novel 4-channel receive-only RF coil for breast imaging in a clinical 1.5T system. The new coil design was inspired by the multi-channel array concept, where multiple conducting strips were arranged in an anatomically conforming profile with the intention of improving sensitivity and SNR. In addition, the coil structure featured an open breast coil concept in order to facilitate MRI-guided biopsy and patient comfort. A comparison of simulation results and actual physical measurements from the prototype RF coil demonstrated good agreement with one another. Also, imaging tests were conducted on a pair of MRI phantoms as well as on a human patient after obtaining proper authorization. The tests revealed good magnetic field homogeneity and a high SNR in the region of interest. In addition, performance comparisons between the prototype 4-channel RF coil and existing high end clinical 4-channel RF breast coils indicated an achievement of superior SNR in conjunction with very good magnetic field homogeneity. Currently, the prototype 4-channel RF coil has outperformed all existing high end clinical 4-channel RF coils used in comparison studies.

Acknowledgements

I would like to express sincere gratitude and appreciation to my advisor, Prof. Reinhold Ludwig, for his guidance, support and encouragement throughout my graduate career at the RF and Medical Imaging Lab. His advice, optimism and dedication were invaluable to the completion of this research. I would also like to thank the members of my dissertation committee, Prof. John Sullivan, Prof. Sergey Makarov, Prof. Gene Bogdanov and Dr. Rosti Lemdiasov, for their criticisms and suggestions, and also for the level of commitment demonstrated in spite of severe weather conditions.

Additional thanks go out to Matt Brevard for running all the human and phantom imaging, and Chris Refuse for machining all the prototypes. Also, I am very grateful to InsightMRI and the Department of Computer and Electrical Engineering for providing the financial support for this research project.

Finally, and most importantly, I would like to thank my parents, Dr. Gabriel Obi and Mrs. Ese Obi for the tremendous sacrifice they made for all their children.

Contents

List of Figures

List of Tables

Chapter 1

Introduction

1.1 Magnetic Resonance Imaging

The foundations of medical imaging systems are based upon the results of the interaction between an interrogating energy source and biological tissues. The form of the energy source employed is dependent on the particular imaging modality. For example, acoustic imaging methods employ ultrasonic sound waves as the intervening form of energy, while X-ray imaging techniques utilize high frequency electromagnetic radiation [1]. The result of the interaction can be used to discriminate between healthy and malignant tissues because of the differences in their spatial and material properties. Also, the various tissues that constitute the biological anatomy can clearly be distinguished based on differences in tissue-specific properties. Thus, imaging modalities with the most variations in tissue-specific properties are the most beneficial in the medical diagnosis of malignancy.

Magnetic Resonance Imaging (MRI) is a relatively new imaging modality that has evolved over the past several years into a powerful and versatile technique capable of providing in-vivo diagnostic images of human and animal anatomies [2]-[4]. Unlike other imaging modalities that utilize ionizing radiation such as X-ray based Computed

Tomography (CT), Positron Emission Tomography (PET) and Microwave Imaging, MRI is a noninvasive imaging technique that does not employ the use of potentially harmful radiation. Also, there exists a multitude of tissue-specific properties that affect and interact with the applied magnetic fields. The two most significant of these properties are the longitudinal (spin-lattice) relaxation and the transverse (spin-spin) relaxation mechanisms. They cover a broad range of values in normal and pathological tissues [5]. In addition, signal acquisition parameters can be manipulated in several ways in order to enhance the contrast of the image generated. Thus, MRI possesses considerably greater diagnostic capabilities when compared with X-ray CT in specific applications, and complements all other in-vivo medical imaging modalities. This in turn has led to a proliferation of MRI systems and has spurred up tremendous research in MRI instrumentation. The install base of clinical MRI systems in the US alone is well over 10,000. MRI belongs to a large group of imaging techniques that are based on the phenomenon of Nuclear Magnetic Resonance (NMR) [6]. This phenomenon was first discovered independently by F. Bloch and E. Purcell in 1946. In general, NMR exploits the resonance behavior exhibited by certain materials when placed in a strong magnetic field. These materials selectively absorb electromagnetic energy at a frequency that varies with the strength of the externally applied static magnetic field, and specific to their constituent nuclei. Absorption of electromagnetic energy places the nuclei of the materials in a state of resonance after which they return to their original thermodynamic equilibrium state through a process known as relaxation with the emission of energy. The use of signal encoding techniques together with spatially disposed magnetic field gradients to obtain information about the internal structures of biological specimens from the emitted energy, forms the basis of the MRI imaging modality.

1.2 MRI Methodology

As mentioned above, MRI exploits the phenomenon of NMR in order to create detailed high-resolution images of human and animal anatomies. First and foremost, the biological sample is placed in a strong static external magnetic field usually refered to as the $\mathbf{B}_0$ field. The $\mathbf{B}_0$ field is usually directed along the z–axis in coordinate space. In addition, a linear magnetic field gradient is superimposed on the $\mathbf{B}_0$ field so that there is a linear variation in magnetic field strength along the preferred spatial axis, in this case the z–axis. Thus, different parts of the sample will experience a variation in magnetic field strength along the z–axis. Since the frequency at which resonance occurs depends on the strength of the magnetic field, there will be a linear variation in resonant frequency across the sample longitudinal to the z–axis. With the application of an RF pulse of a particular frequency, only slices of the sample having a corresponding resonant frequency will be excited. The strength of the received signal will be proportional to the number of resonating nuclei in the excited slice. This process of selective excitation along the z–axis is referred to as *slice selection*. Thus, by superimposing a comparatively low magnetic field gradient on the main magnetic field, it is possible to encode the energy of the RF pulse in a particular slice orthogonal to the z–axis. A typical RF pulse is ideally rectangular in the frequency domain so as to clearly demarcate slice boundaries. The spectral width of the RF pulse and the strength of the magnetic field gradient determine the thickness of the slice. Also, the center frequency of the RF pulse defines the position of the slice along the z–axis. After confining the excitation to a single slice in the imaging volume, the next step is to encode the image information within the excited slice using additional gradient systems. These gradient fields are imposed along each of the two principal axes of the image plane, notably the x and y axes. With the RF pulse and z–gradient switched off, a gradient field is established along one axis of the image plane, the x–axis, to sub-divide the excited slice into narrow strips of distinct resonant frequencies. This process is known as frequency encoding and the x–axis is identified as the frequency encoding axis. After frequency encoding, the frequency of the signal received from the excited slice is a weighted sum of the distinct frequencies of the individual strips. The weight of each frequency component is proportional to the number of nuclei in each strip and can be determined in the frequency domain after a Fourier transform. Finally, a gradient is imposed along the one remaining principal axes of the image plane, the y–axis, to produce a systematic variation in the phase of the received signal which encodes the final spatial information. A more detailed description of the basic principles of MRI is presented in Chapter 2.

1.3 MRI RF Coils

MRI RF coils form an essential component of the MRI imaging system where they produce the necessary high-frequency homogeneous electromagnetic field, the $\mathbf{B}_1$ field, required to excite the nuclei of the sample being imaged into coherent precession. In addition, they serve to couple electromagnetic energy between the imaging sample and the MRI imaging system. They are usually designed around the notion of an electrical resonator since they possess an intrinsic inductance due mainly to the spatial arrangement of the conductors that constitute the RF coil. These conductors are strategically arranged in a geometric profile around the imaging volume to produce the uniform $\mathbf{B}_1$ field. The notion of resonance guarantees signal selectivity and provides rudimentary signal gains at the desired resonance frequency. Additional capacitive components are required to establish the resonance condition at the operating frequency. When the RF coil resonates at the desired frequency, large voltage and current oscillations are developed from the application of a small input signal. The strength of the resonance is described by the quality factor Q given by

$$Q = 2\pi \cdot \frac{\textit{maximum stored energy}}{\textit{energy dissipated per cycle}} \tag{1.1}$$

The quality factor is influenced by such parameters as the strength of the $\mathbf{B}_1$ field, the image signal-to-noise ratio (SNR) and the sensitivity of the RF coil. For a given coil configuration, a higher quality factor implies more available stored energy which invariably ensures larger $\mathbf{B}_1$ field strength, higher SNR and improved coil sensitivity. Another important parameter that strongly influences the SNR of an RF coil is the size of the illuminating volume or more appropriately the coil filling factor. The smaller the volume of the coil, the greater the sensitivity and SNR in the region of interest (ROI). Clearly, the volume of the sample governs the limit on the size of the illuminating volume. Thus, a more anatomically correct conductor profile is essential for an improved filling factor in the design of RF coils. Also, the strength of the main magnetic field plays an important role in the determination of MRI image quality but improved RF coil design techniques may provide greater image quality enhancements and less capital costs in system upgrades.

MRI RF coils are generally classified as volume coils and surface coils respectively. Volume coils are generally utilized as RF transmit coils although they can be used effectively as RF receiving coils. They are designed explicitly to produce a relatively homogeneous $\mathbf{B}_1$ field in the ROI. In addition, they enclose the entire ROI in order to achieve the highest possible field uniformity for a given coil configuration. Examples of volume RF coils include the birdcage coil [7], the saddle coil [6] and the Transverse Electromagnetic (TEM) resonator [8]. These volume coils are depicted in Fig.1.1. The most widely used volume coil for MRI imaging is the birdcage coil [7]. In the standard birdcage configuration of Fig.1.1(a), the straight conductors that are arranged in a circularly parallel profile are called rungs, while the circular conductors that connect

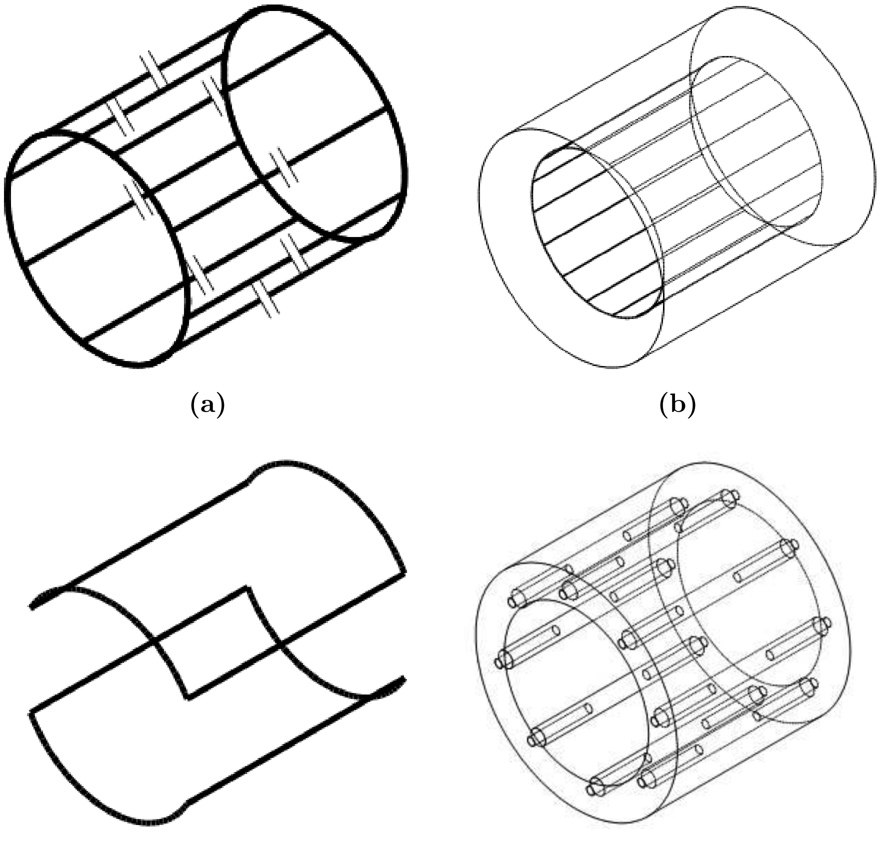

(a) (b) (c) (d)

Figure 1.1: Various MRI volumes coil configurations [9]: (a) birdcage coil, (b) shielded birdcage coil, (c) saddle coil, and (d) TEM resonator.

the rungs at the ends are called the end-rings. To establish resonance in the birdcage configuration, the rungs or end-rings are segmented by capacitors. As such, two possible birdcage coil configurations are possible. If only the rungs are segmented by capacitors, we have the traditional low-pass bird cage coil configuration. Similarly if only the end-rings are segmented by capacitors, we have the high-pass configuration. Hybrid configurations are also possible.

The operating mode of a birdcage coil is the resonant mode that produces a single circle sinusoidal current distribution in the rungs. This mode is capable of producing a true circularly polarized $\mathbf{B}_1$ field. The birdcage coil in a transmit configuration can be driven with either a linear drive or quadrature drive. A linear drive produces a uniform field with two circularly polarized components that rotate in opposite direction. Only one of these components can be effectively used for MRI imaging. On the other hand, a quadrature drive produces only one circularly polarized component. This is because the quadrature drive combines two perpendicular magnetic fields that are 90° out of phase to produce a circularly polarized magnetic field. Because only one circularly polarized magnetic field is produced by a quadrature driven birdcage coil, it requires half the input power and produces $\sqrt{2}$ times higher SNR when compared to a linear driven birdcage coil. Also, a birdcage coil can be shielded as in Fig.1.1(b) to help minimize radiation losses and reduce the interference of MRI gradient coils.

Another widely used volume coil is the TEM resonator [8]. A simple TEM configuration is shown in Fig.1.1(d). It consists of a shield with multiple inner conductors that are share a similar profile to the rungs of the birdcage coil. However, these inner conductors are connected to the shield by capacitors thus forming a transmission line. The transmission line design of the TEM coil is the key to achieving desired performance in high field MRI systems. Other traditional volume coil configurations, including the birdcage coil show a degradation in performance at high field strengths where the dimensions of the coil become comparable to half the wave length in free space. As such, the TEM coil is more efficient than a comparable sized birdcage coil [8]. In addition, the TEM resonator can be driven in quadrature to produce a truly uniform circularly polarized magnetic field.

Surface coils are primarily used as receive-only MRI RF coils because of their poor field uniformity [6]. Typical surface coil configurations are illustrated in Fig.1.2. They consist essentially of an arrangement of planar conductors and segmenting capacitors. The capacitors are required to establish the coil resonance at the desired operating frequency. Surface coils only cover a small region of the imaging volume and hence, provide a high SNR when compared to volume coils. The field strength is highest in the region closest to the coil, but it drops off very rapidly at increasing distances from the coil. Examples of surface coils include the single loop coil Fig.1.2(a), the

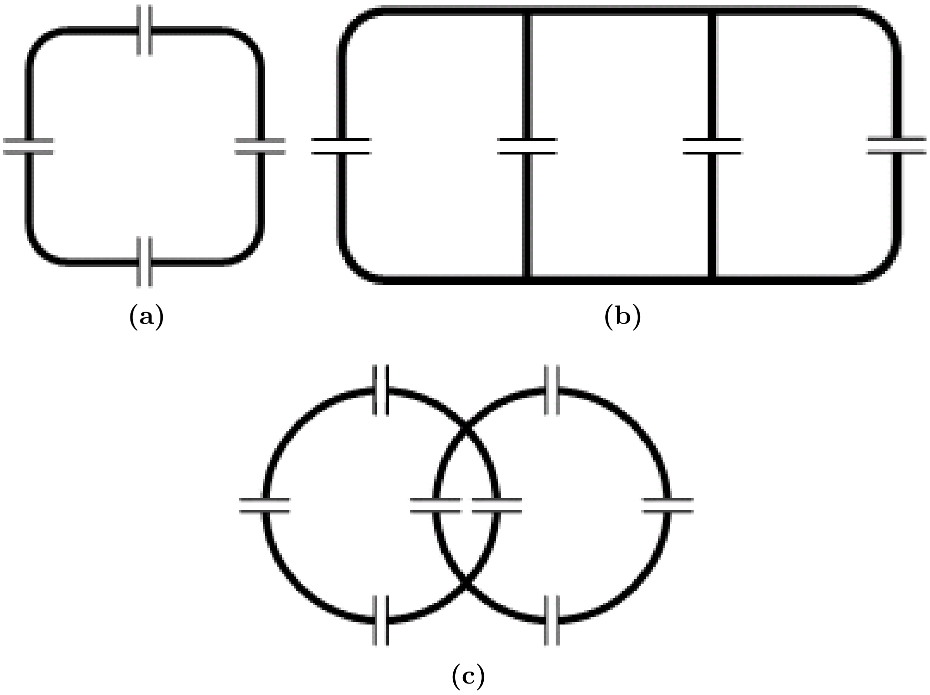

(a) (b)

(c)

Figure 1.2: Various MRI surface coil configurations [9]: (a) traditional single loop surface coil, (b) multiple loop surface coil, and (c) phased array.

multiple loop surface coil Fig.1.2(b), and the phased array coil Fig.1.2(c). In some MRI imaging systems, a dual coil configuration may exist where a volume coil is used as the RF transmit coil and the surface coil is used as the receiving coil. Such a configuration has the benefits of the uniformity of the $\mathbf{B}_1$ field produced by the volume coil, and the high sensitivity of the surface coil which translates to improved image quality. The multiple loop configuration of Fig.1.2(b) is an attempt to improve upon the poor $\mathbf{B}_1$ field uniformity of the single loop surface coil. Unfortunately, it has the disadvantage of being more difficult to incorporate into a dual coil system when compared to a simple single loop coil.

The phased array coil is another significant improvement in surface coil design technology [10]. A simple phased array designed is shown in Fig.1.2(c). It consists of individual single loop surface coils that operate independently from one another. It has the added advantage of providing greater field coverage around the imaging volume while maintaining the high SNR associated with single loop surface coils. Its major drawback is the need to provide multiple receiving channels on the MRI imaging system. Also, decoupling the individual single loop coils of the coil array poses a significant engineering challenge. The main design considerations in the development of RF coils include the desired operating frequency, the volume of the ROI, the uniformity of the required $\mathbf{B}_1$ field, the filling factor, and the Q or coil loss [7]. The desired operating frequency is determined by the strength of the main magnetic field, the $\mathbf{B}_0$ field, and the gyromagnetic ratio of the target nuclei. Hydrogen nuclei are of primary importance in MRI because of its great abundance in biological tissue. For most RF coils, as the desired ROI increases, the dimensions of the RF coil increase resulting in an increase in the inductance of the coil. The upper bound of the operating frequency is determined primarily by the inherent inductance and stray or parasitic capacitance of the coil. Hence, there exists a strong relationship between the desired operating frequency and the size of the ROI [11]. The filling factor defines how well the RF coil encloses the sample in the region of interest. For optimum signal quality, it is imperative that the RF coil covers as much of the imaging volume as possible. Hence, most coil designs incorporate a ROI that is anatomically shaped and closely encloses the biological sample. The RF field homogeneity is determined primarily by the spatial arrangement of the conductors that constitute the RF coil. The field homogeneity can be improved upon by enlarging the dimensions of the RF coil. This technique has the disadvantage of increasing coil losses and decreasing the filling factor.

1.4 Modeling Methods for MRI RF Coils

The rapid evolution in computational electromagnetics is due in part to the proliferation of the high-speed digital computer and its associated high-density memory units. As a result, physical problems that were unamenable to classical analytical methods can now be solved using a variety of computer-based techniques. One such problem is the modeling of MRI RF coils. The past several years have seen a multitude of numerical and analytical methods for modeling and analyzing MRI RF coils. Each method offers a variety of capabilities with various degrees of complexity and accuracy. The lumped-element circuit model is one of several modeling techniques that can be applied to the analysis of a variety of MRI RF coils at relatively low RF frequencies [12]-[15]. In this modeling method, the conductive elements or strips of the RF coils are modeled as lumped inductances in combination with mutual inductances arising from the interactions between strips. Any capacitive element added to the coil configuration to establish resonance is treated as a lumped capacitance. Thus, the entire coil configuration is modeled as a lumped equivalent circuit that can subsequently be analyzed using well established circuit analysis techniques. This invariably helped identify the lumped-element circuit model as the most established simulation technique for MRI RF coil analysis. It is very well suited for RF coil modeling in cases where the dimensions of the RF coil are small in comparison with the free-space wavelength at the operating frequency. It becomes grossly inaccurate at higher operating frequencies where the free-space wavelength becomes comparable to the dimensions of the RF coil. As such, it cannot be used in high-field MRI studies. Also, there is the added difficulty in the determination of the lumped self and mutual inductances of the coil profile. In addition, the model cannot be used to analyze the complex field interactions between RF coils and biological tissues. Although the lumped-element circuit model prides itself as being one of the fastest computational methods available for RF coil modeling, its shortcomings at high frequencies necessitate the use of other modeling techniques that satisfy the full set of Maxwell's wave equations. These alternative methods are generally classified as discretization methods because they discretize the geometric area or volume of the physical problem before providing an approximate solution. The most widely used discretization methods include the Finite Element Method (FEM), the Finite Difference Method (FDM) and the Method of Moments (MoM).

The Finite Difference Method is the oldest amongst the discretization methods, being originally developed to approximate the derivative operators in the differential equation being solved [16]. As a result, it is the simplest discretization method to implement numerically to solve the full set of Maxwell's equations. In addition, it has recently gained considerable recognition in the MRI research community because of the ease of creating complex biological models of living tissues for an FDM implementation [17]-[19]. A sophisticated grid-based model of the human head was developed in [17], in an effort to determine the specific absorption rate (SAR) and the $\mathbf{B}_1$ field inhomogeneity of a shielded birdcage coil loaded with a human head. In a typical FDM implementation, a computational domain is established and then discretized by a uniformly spaced two or three dimensional grid. The electric and magnetic fields are later determined directly at a point or a series of points in the grid space within the computational domain, and at each time step during an evolution in time in the case of a time domain implementation. The main advantages of the FDM technique include ease of implementation and the ability to model linear and non-linear dielectric and magnetic materials. Its major drawbacks include very large computational domains, requirement of finer grid spacing to improve accuracy, and the associated long solution times. In addition, it can be very computationally demanding even on powerful computing platforms with highly specialized architectures.

Another discretization method that has been successfully applied to the modeling of RF coils is the Finite Element Method [20, 21]. The FEM establishes and discretizes the computational domain into a collection of simple geometric polygons or polyhedra of various sizes. The electric and magnetic fields within each element is then interpolated using specially developed basis functions. This essentially converts the underlying partial differential equation into a sparse system of linear equations that can then be solved using established linear algebraic techniques. Since the computational domain of an FEM implementation can be discretized into simple geometric elements, the FEM can be used with geoemetric or mesh discretizations that conform more closely with complex biological tissues with heterogeneous electromagnetic properties. Unfortunately, the FEM still has the limitation of requiring a very large computational domain, especially in situations where high solution accuracies are required. Invariably, large computational domains equate to very long solution times.

The Method of Moments is yet another discretization method that has been applied extensively in the simulation of unloaded MRI RF coils [22]-[25]. The MoM essentially transforms a boundary integral equation, with a suitable choice of basis function in each geometric element of the mesh discretization into a linear system of equations. Since the MoM is based on an integral formulation rather than a differential formulation, it offers a progressively smaller computational domain in comparison with the FEM or the FDM. Also, reasonable accuracy can be obtained with the use of a less dense mesh discretization favoring fast solution times. The major disadvantages of the MoM includes an increase in implementation complexity and an inability to model accurately the complex interaction between RF coils and biological tissues [26]. As a result, a lot of hybrid MoM based implementations have been introduced to help ameliorate the difficulty in simulating an RF coil loaded with biological tissue. Chen *et al.* [17] utilized a hybrid MoM/FDTD (finite difference time domain) implementation to analyze the specific absorption rate and $\mathbf{B}_1$ field distribution of an RF coil loaded with a human head, but their implementation failed to account for the effects of the interaction between the head model and the current distribution on the RF coil. Feng Liu *et al.* [26] developed a hybrid approach that is very similar to [17], but utilized a current source distribution that considered only the internal average wave behavior in the biological tissue. Another hybrid approach was proposed by [27] in an effort to combine the FEM with an MoM based implementation. They successfully applied this hybrid approach in the analysis of simple dielectric structures attached to conducting bodies. However, it cannot be used to model loaded RF coils without introducing additional complexities in the hybrid formulation.

The difficulty in providing an MoM based implementation to the problem of modeling loaded MRI RF coils lies in the choice of an appropriate volumetric basis function in the computational domain. D. H. Schaubert *et al.* [28] introduced the Schaubert-Wilton-Glisson (SWG) volumetric basis function that is a three dimensional extension of the popular two dimensional Rao-Wilton-Glisson (RWG) surface basis function [29]. The SWG basis functions were used to approximate the electric flux density $\mathbf{D}$ in each volume element of the mesh discretization of an inhomogeneous body. But the electric flux density $\mathbf{D}$ in a pure dielectric is divergence-free while the SWG volumetric basis have non-zero divergence. This will inevitably lead to spurious charges which are the primary sources of numerical inaccuracies in an MoM volumetric formulation [26]. In order to overcome this apparent difficulty, S. A. de Carvalho *et al.* [30] introduced the divergence-free solenoidal basis function. These basis functions were used to approximate the equivalent polarization currents in each volume element of the mesh discretization.

In this dissertation, we propose a unique MoM based implementation that is well suited for modeling loaded MRI RF coils. The proposed method uses two distinct basis functions to describe the surface current density on the RF coil, and the sum of the volume current density and the displacement current density in the inhomogeneous biological tissue. These basis functions conform very well with the physical properties they describe resulting in a more stable numerical implementation. Furthermore, we will discuss the application of our MoM based implementation in the design and development of a new 4-channel receive-only MRI RF coil for breast imaging in a clinical 1.5T system.

1.5 Objectives

The main objective of this dissertation is to develop a distinctive MoM methodology that can be used in the design of MRI RF coils loaded with biological tissues. The goal is to overcome existing limitations in the use of hybrid MoM formulations as well as other volume MoM only implementations. Our approach to formulating an MoM implementation combines two distinct basis functions: the RWG basis function, and the divergence-free solenoidal basis function. The surface conductors of the RF coil will be discretized into triangular surface elements while the volume of the biological tissue will be discretized into tetrahedral volume elements. The RWG basis function is associated with each interior edge of the triangular mesh domain where it is used to describe the surface current density on the surface conductors of the RF coil. In the inhomogeneous biological tissue, the divergence-free solenoidal basis function is used to describe a new vector quantity that represents the sum of the volume current density and the displacement current density. This new vector quantity is the total current density, and it is always divergence-free as dictated by the continuity equation irrespective of the electrical properties of the tissue. Thus, spurious charges which are the main source of numerical problems in MoM volume formulations are not generated [29], since the basis function describes the physical property of being divergence-free exhibited by the total current density.

In addition, we utilized our MoM methodology in the design of a novel 4-channel MRI RF coil for breast imaging in a 1.5T clinical MRI system. The new coil design was inspired by the multi-channel array concept where multiple conducting strips are arranged in an anatomically conforming profile with the intention of improving sensitivity and filling factor. The 4-channel receive-only array system is made up of two RF coils each providing two independent receive channels. The unique design facilitates its operation in a dual-channel configuration where each RF coil provides two resonant modes that can be combined in single-channel quadrature, thus providing high SNR in conjunction with good $\mathbf{B}_1$ field coverage across the region of interest. A comparison of simulation results and actual physical measurements from the prototype RF coil will be presented, along with bilateral images of an MRI phantom and a human patient in a clinical MRI system.

1.6 Organization

This dissertation is organized in six chapters highlighting the different aspects of this work. Following the introductory chapter, Chapter 2 discusses discusses the basic principles of MRI and MRI systems, including a brief discussion on the fundamentals of image encoding techniques. In Chapter 3, we present a detailed discussion on the formulation of our distinct MoM implementation along with the properties of the basis functions that were utilized. Chapter 3 also discusses a prominent singularity extraction technique that was used in extracting the singular kernels from the resulting potential integrals in our MoM implementation. In Chapter 4, we provide the necessary validation to ascertain the capability our MoM implementation as an effective modeling methodology for RF coil analysis. We also discussed its implementation in software as well as introduced several circuit models that can be realized from the simulation results obtained. The design of a novel 4-channel receive only RF coil for breast imaging is presented in Chapter 5. We introduce its unique anatomical profile, and showcase our MoM implementation in the determination of the equivalent circuit parameters of the RF coil. Chapter 5 also presents comparisons between RF coil characteristics obtained using simulation and actual physical measurement from a network analyzer. In addition, we discuss the construction of a prototype and present bilateral images from MRI phantoms as well as a human patient. We conclude with a summary of our findings and future work in Chapter 6. Additional information on the construction of the RF coil can be found in the Appendices.

Chapter 2

Basic Principles of MRI

2.1 Nuclear Magnetic Moment

Associated with most atomic nuclei is a property known as spin angular momentum; this constitutes the foundation of nuclear magnetic resonance. An MRI system utilizes variations in the spin angular momentum of certain atomic nuclei in biological tissues to derive images that contain valuable information concerning their spatial distribution. The variations in spin angular momentum result from interactions with an applied static magnetic field and electromagnetic radiation. From a classical mechanics point of view, spin angular momentum originates from the motion of elementary particles in the nucleus of the atoms as they rotate about their axis. These particles have mass and thus generate angular momentum as they rotate. Positively and negatively charged particles can be regarded as spheres of distributed positive or negative charges, while neutral electrical particles such as the neutron can be thought of as a combination of distributed positive and negative charges. The rotation of these distributed charges generates small magnetic fields that are collinear with the direction of the spin axes. This magnetic field is termed the magnetic moment and has features similar to a bar magnet. The strength of the magnetic moment determines

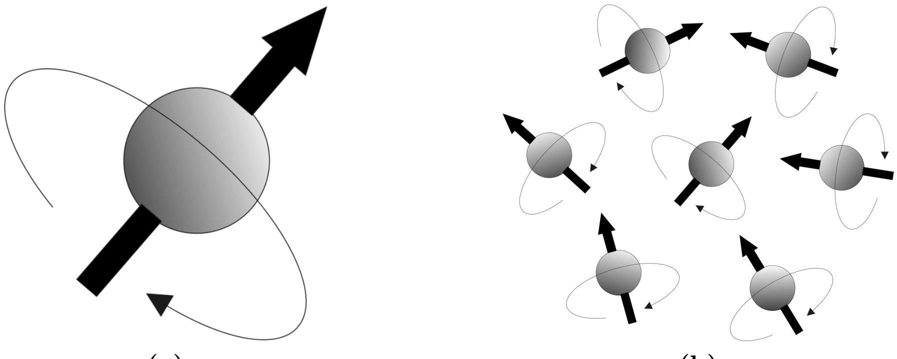

(a) (b)

Figure 2.1: Nuclear magnetic moment: (a) Elementary magnetic dipole, (b) Collection of magnetic dipoles in the absence of an applied magnetic field.

the sensitivity of detection in magnetic resonance and it is dependent on the type of nucleus. Most frequently, the hydrogen nucleus with one proton is the nucleus of choice in MRI because it possesses the strongest magnetic moment and its abundance in organic tissues. Fig.2.1(a) shows a hydrogen nucleus spinning about its axis. The basic principles of magnetic resonance can be explained using the collection of hydrogen nuclei shown in Fig.2.1(b). As can be seen, the individual magnetic moments have no preferred orientation in the absence of an external magnetic field. With the application of an external magnetic field $\mathbf{B}_0$, quantum mechanics dictates that the magnetic moments will align with the external field in two possible orientations: parallel or anti–parallel, as shown in Fig.2.2(a). Parallel alignment with the magnetic

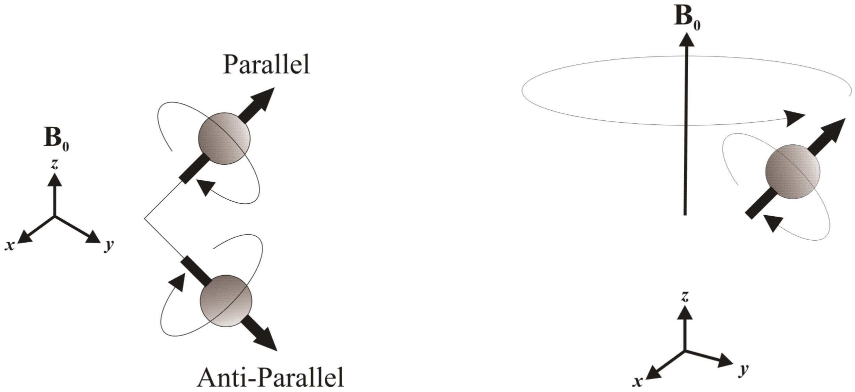

(a) (b)

Figure 2.2: (a) Alignment orientation of the hydrogen nucleus in an external magnetic field, (b) precession of the hydrogen nucleus in the B_0 field.

field is the preferred orientation because it guarantees the lowest energy state. Generally, thermal energy causes the energy difference between the two orientations to be minimal, with the two orientations almost equally populated resulting in a net bulk magnetization $\mathbf{M}$. Naturally, the nucleus can change from one orientation to another by absorbing or emitting photons with energy equal to the energy difference. In both orientations, the spin angular momentum causes the magnetic moment to precess about the $\mathbf{B}_0$ axis as shown in Fig.2.2(b). Since there are more nuclear spins in parallel alignment with the field, the net bulk magnetization $\mathbf{M}$ is also aligned with the $\mathbf{B}_0$ field. The frequency of precession is governed by the Larmor equation as

$$f = \gamma B_0 \tag{2.1}$$

where f is the frequency of precession, γ is a characteristic constant that depends on the given nucleus, and B_0 is the strength of the externally applied $\mathbf{B}_0$ field. For hydrogen nuclei, γ is given as 4257 Hz/Gauss. Thus, in a field strength of 1.5 T, the hydrogen nucleus will precess with at a frequency of 63.85 MHz.

2.2 Application of Radio Frequency Pulses

The detection of an NMR signal is facilitated by the establishment of a resonance condition [5]. The resonance condition represents a state of alternating absorption and dissipation of energy. Energy absorption is achieved through the application of RF pulses, while energy dissipation is caused by relaxation processes. Consider the application of RF radiation at the Larmor frequency to a bulk sample of non-magnetic material in an applied static magnetic field. The applied RF radiation is composed of coupled electric and magnetic field components. The magnetic field component is denoted by $\mathbf{B}_1$, and it resides in a plane perpendicular to $\mathbf{B}_0$ while rotating about $\mathbf{B}_0$ at the Larmor frequency as shown in Fig.2.3. During the period when the RF

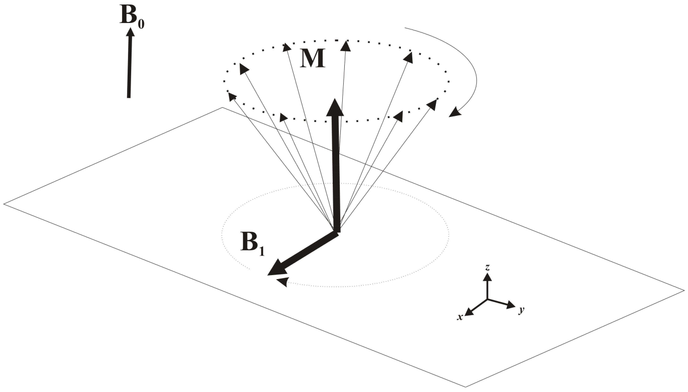

Figure 2.3: Net bulk magnetization **M** rotating about $\mathbf{B}_1$ when the RF pulse is present [5].

radiation is present, the net bulk magnetization **M** starts to rotate about the axis of $\mathbf{B}_1$. Since both $\mathbf{B}_1$ and **M** are rotating about $\mathbf{B}_0$ at the Larmor frequency, they appear stationary relative to one another as depicted in Fig.2.3. The consequence of the application of $\mathbf{B}_1$ is to rotate **M** by a certain angle away from the $\mathbf{B}_0$ axis. This angle is called the flip angle, and it is directly proportional to the duration of the applied RF radiation. Hence, if $\mathbf{B}_1$ persists for the appropriate duration of time, **M** can be made to rotate onto the transverse plane. While in the transverse plane and rotating at the Larmor frequency, **M** will induce an NMR signal in the RF receiver coil which is oriented in the transverse plane as shown in Fig.2.4. This signal can be used to observe the characteristics of **M** in the transverse plane. The RF radiation that brings **M** unto the transverse plane is usually referred to as the 90° RF pulse.

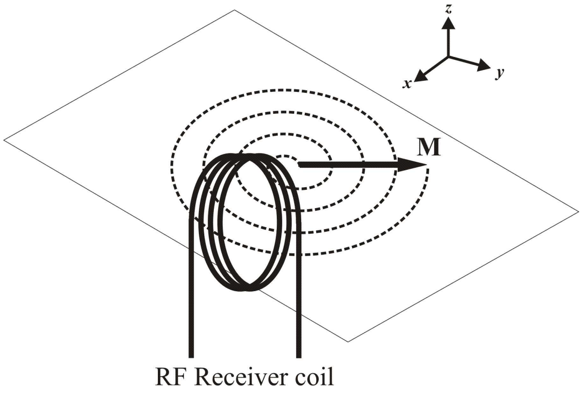

Figure 2.4: **M** rotates on the transverse plane after the application of a 90° RF pulse [5].

The 90° and 180° refers to the resulting flip angle after the application of the RF radiation. The 90° flip angle is very important because the strongest NMR signal is obtained when $\mathbf{M}$ rotates in the transverse plane. The 180° flip angle is primary important in spin-echo imaging techniques where it is used to reverse the direction of $\mathbf{M}$ once it is on the transverse plane.

2.3 Relaxation

After the application of a 90° RF pulse, $\mathbf{M}$ rotates in the transverse plane at the Larmor frequency and gradually decays to zero. The decay of $\mathbf{M}$ is governed by an exponential process with time constant $T_2^\star$ referred to as the transverse relaxation time. The transverse relaxation time is dependent on the material characteristics of the sample. The decay of transverse magnetization is due to the lost in synchronization of the precessing nuclei that make up the sample. This is known as dephasing in the transverse plane [5]. Since the NMR signal observed is the sum of all the transverse components, sufficient dephasing will eventually lead to complete signal cancellation. The dephasing phenomenon arises because of the inhomogeneity in the $\mathbf{B}_0$ field and the mutual interactions between the magnetic moments of the atoms and molecules that constitute the sample. As $\mathbf{M}$ decays to zero in the transverse plane, there is an exponential build up of magnetization along the $\mathbf{B}_0$ axis. This is referred to as longitudinal or T_1 relaxation, and it is also material dependent. Eventually, the longitudinal magnetization would return to its maximum value of $\mathbf{M}$ aligned with the $\mathbf{B}_0$ field. The build up of longitudinal magnetization is inevitable and is due mainly to the persistent $\mathbf{B}_0$ field.

2.4 Magnetic Field Gradients

In MRI image acquisition, there is a need to introduce spatial variations in the received NMR signal. This is necessary in order to distinguish between signals from several regions of the sample. Spatial localization is achieved by the application of a linearly varying gradient magnetic field that modifies the main $\mathbf{B}_0$ field in the region of interest (ROI) containing the sample. According to (2.1), this variation in the $\mathbf{B}_0$ field would cause a variation in the precession frequencies of the different nuclei that constitute the sample. In effect, the detected NMR signal would be an interference combination of the different precession frequencies from various spatial locations within the sample. These frequencies can then be separated in the frequency domain using the Fourier Transform. Hence by using a set of three orthogonal gradient magnetic fields along the three physical spatial axes, the position of a voxel of the sample in the ROI can be acquired.

2.5 Image Encoding Techniques

Selective slice excitation refers to the process of restricting the signal response in the third spatial dimension in order to create a 2D image of the sample. This is achieved by selectively exciting only a well defined slice of the sample within the ROI. If a magnetic field gradient is applied along an axis normal to the chosen slice plane, (2.1) dictates that there will be a linear variation in resonance frequencies along that axis. This forms the basis of the selective slice exciation process in MRI imaging. The relationship between the thickness of the excited slice d, the RF pulse bandwidth Δf and the applied field gradient amplitude G is given by

$$\Delta f = \gamma G d \tag{2.2}$$

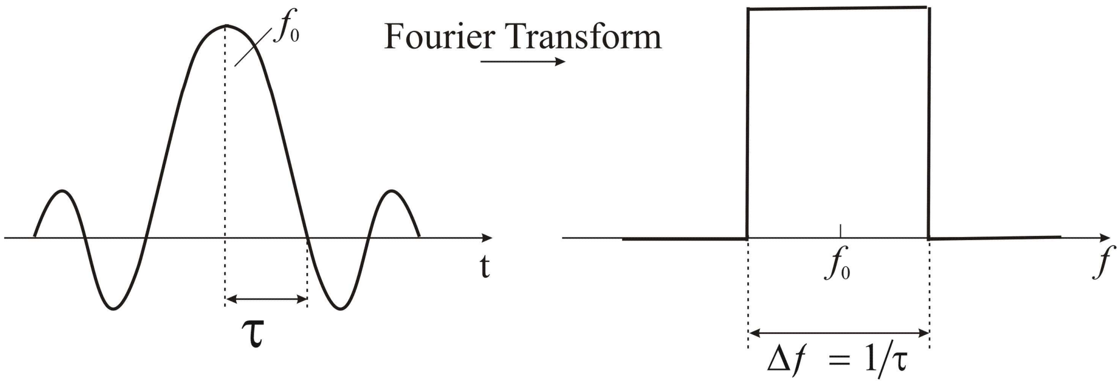

Figure 2.5: An RF sinc pulse and its fourier transform. The RF pulse excites a band of frequencies of width Δf centered around the frequency f_0.

The RF pulse is generally a sinc pulse because of the desirable properties of its fourier transform as shown in Fig.2.5. Thus, only the desired band of frequencies will be generated for slice excitation. The location of the slice z_d along the axis can be found using

$$f = \gamma(\mathbf{B}_0 + z_d G) \tag{2.3}$$

After the selective excitation process, the next step is to encode the image information within the desired slice. The image information sought is made up of the amplitude of the NMR signal generated within the various locations in the excited slice. The two spatial axes of the image plane are encoded using two distinct processes referred to as frequency encoding and phase encoding. In frequency encoding, a gradient field G_f is imposed along one of the two principal axes of the image plane. This causes the received signal to be a linear combination of the various NMR signals from different parts of the slice along the normal to the slice plane. The principal axis along which the field gradient is applied is called the frequency encoding axis. The bandwidth BW of the received signal and the field of view FOV_f along the frequency encoding axis are related by

$$BW = \gamma G_f FOV_f \tag{2.4}$$

In order to encode the spatial information along the remaining principal axis, a

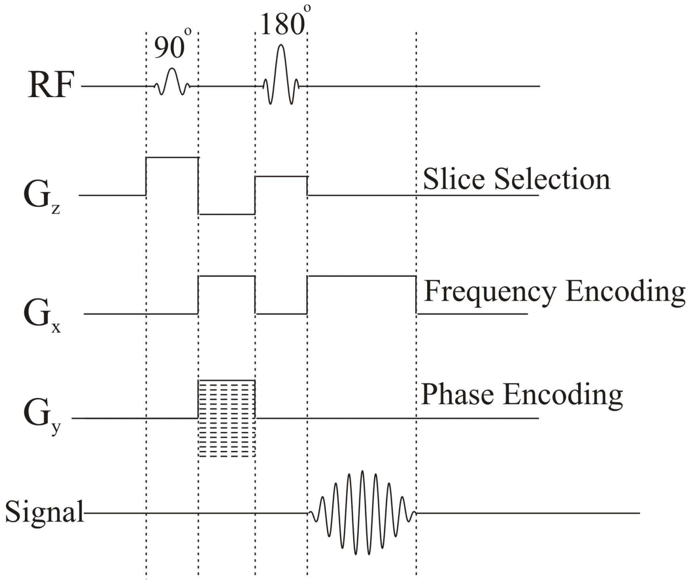

Figure 2.6: A general MRI image acquisition sequence [5].

systematic variation in the phase of the signal is incorporated along the axis. This is referred to as phase encoding, and the axis on which it is implemented is called the phase encoding axis. A gradient field G_p is applied along the phase encoding axis to systematically vary the phase of the NMR signal. The maximum change in phase between the two extremes in the field of view FOV_p of the phase encoding dimension is 180°. The variation in phase of the signal is proportional to the amplitude and duration of the applied gradient as well as the position along the phase encoding axis. This can be expressed quantitatively by

$$\gamma G_p FOV_p T_p = N_p \pi \tag{2.5}$$

The complete acquisition sequence is shown in Fig.2.6. This sequence is repeated several times to encompass the FOV_p while varying the amplitude of the phase encoding gradient. The resulting NMR signals are used to create a 2D image of the slice plane.

2.6 The MRI System

The basic hardware components of an MRI System are illustrated in Fig.2.7. These components include a main magnet, a set of gradient coils, RF coils (both transmitter and receiver) and a computer system. The main magnet produces the primary magnetic field, the $\mathbf{B}_0$ field, over the ROI. $\mathbf{B}_0$ fields of 1.5T are common in the medical imaging field, while fields as high as 19T exist in research systems. It is desirable that the primary magnetic field be uniform throughout the desired ROI. The main magnet is usually a solenoid-type electromagnet with a cylindrical bore. Such high-field magnets are almost exclusively superconducting. The superconductors are cooled to a temperature near absolute zero by using liquid helium and liquid nitrogen combination. This ensures that the superconductor retains its superconducting properties. The gradient coil system consists of a set of three orthogonal coils that provide the

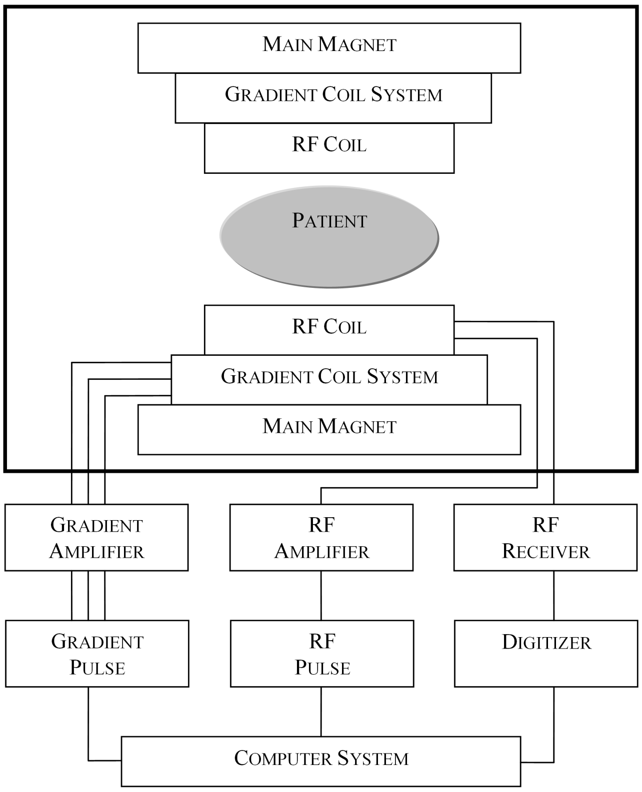

Figure 2.7: Block diagram of a generic MRI System [6].

orthogonal field gradients along the x, y and z axes. By superimposing these field gradients on the main $\mathbf{B}_0$ field, layered selection and spatial encoding are realized. Strong field gradients that are highly uniform in the ROI are desirable in order to minimize image distortions. Besides producing strong uniform field gradients, the gradient coils must be able to switch on and off rapidly in order to avoid image obscurity due to motion effects that occur in real-time imaging such as the cardiac cycle. Hence, gradient coils are optimized for low inductance. The RF coil produces the high-frequency homogeneous electromagnetic field, the $\mathbf{B}_1$ field, necessary to excite the nuclei of the sample being imaged into coherent precession. By reciprocity, the coil can be used to couple emitted RF energy from the nuclei into an external circuitry. A single RF coil can be employed as a transmitter and a receiver, or separate coils can be provided for transmitting and receiving. The $\mathbf{B}_1$ field generated by the RF transmit coil must be uniform across the entire ROI. The sensitivity of the RF receiver coil is important to obtain a high image signal-to-noise ratio, but it does not necessarily have to be uniform in the ROI. The gradient amplifier, gradient pulse generator, RF amplifier, RF pulse generator, RF receiver and digitizer constitute the drive electronics for the MRI system. The various amplifiers are typically housed separately, and drive all the coils in the MRI system. The computer system sets up the pulse sequences, controls all the coils drivers, and reconstructs the image for display.

Chapter 3

Method of Moments Formulation for MRI RF Coil Modeling

As previously mentioned, the modeling of RF coils in MRI is important in RF coil design and development as well as in describing the interaction between RF energy and biological tissue, particularly at high magnetic field strengths where considerable engineering challenges exist in the delivery of RF energy [31]. Consequently, these challenges necessitate the need to develop a full wave analysis method based on the complete set of Maxwell equations. We have addressed such a need by proposing a frequency domain approach based on the Method of Moments (MoM) that combines two sets of basis functions in order to conveniently model highly conductive surfaces and inhomogeneous biological bodies. The conductive strips of the RF coil are discretized into triangular surface elements, while the biological body of interest is discretized into tetrahedral volume elements. A modified version of the Rao-Wilton-Glisson (RWG) [29] basis function is associated with each interior edge of the triangular elements, where it is used to describe the surface current density on the surface of the RF coil. For the case of the biological body, the divergence-free solenoidal basis function [30] is used to describe a new vector quantity that represents the linear combination of the volume current density and the displacement current density [32]. This new vector quantity is termed the total current density; it is always divergence-free as dictated by the continuity equation, irrespective of the electrical properties of the biological body.

The divergence-free nature of the solenoidal basis function guarantees that spurious charges which are the main source of numerical inaccuracies in most MoM volume integral formulations are not generated [29]. As such, the MoM formulation developed using this new approach is very robust and can be applied to provide solutions to a wide variety of electromagnetic problems.

3.1 Governing Equations

All macroscopic electromagnetic phenomena that occur in linear, isotropic media are governed by Maxwell equations, the constitutive relationships and the boundary conditions that exist in the environment around the media. For time harmonic electromagnetic fields with a $e^{j\omega t}$ dependence, Maxwell equations can be specified in differential form as

$$\nabla \times \mathbf{E} = -j\omega \mathbf{B} \tag{3.1}$$

$$\nabla \times \mathbf{H} = j\omega \mathbf{D} + \mathbf{J} \tag{3.2}$$

$$\nabla \cdot \mathbf{B} = 0 \tag{3.3}$$

$$\nabla \cdot \mathbf{D} = \rho \tag{3.4}$$

where

$\mathbf{H}$ = magnetic field intensity, in A/m

$\mathbf{B}$ = magnetic flux density, in T or Wb/m^2

$\mathbf{D}$ = electric flux density, in C/m^2

$\mathbf{E}$ = electric field intensity, in V/m

$\mathbf{J}$ = total electric current density, in A/m^2

ρ = electric charge density, in C/m^3

The linear interaction of electric and magnetic fields with various media are described by the constitutive relationships

$$\mathbf{B} = \mu \mathbf{H} \tag{3.5}$$

$$\mathbf{D} = \epsilon \mathbf{E} \tag{3.6}$$

$$\mathbf{J} = \sigma \mathbf{E} \tag{3.7}$$

where σ, ϵ and μ denote the electrical conductivity, the electric permittivity, and the magnetic permeability of the respective medium. For these expressions to be physically valid, the electric and magnetic field vectors must be single-valued, bounded, and continuous in space and time with continuous derivatives [33]. These conditions are generally satisfied by field vectors associated with electromagnetic waves except where there are discontinuous distribution of charge and current densities. These discontinuities in charge and current densities usually occur at the boundaries between media interfaces where there discrete changes in material properties across the boundary. Consequently, a complete description of the electric and magnetic field vectors not only requires (3.1)–(3.7), but also the associated boundary conditions at the media interfaces.

3.2 Method of Vector and Scalar Potentials

The introduction of potential functions in electromagnetic field problems serve as a means to obtain solutions to problems involving radiation and scattering of electromagnetic waves in an unbounded region. The magnetic vector potential is one such potential formulation that is used extensively in electromagnetics. Over the past several years, various magnetic vector potential formulations have been implemented [34]–[35]. Although the Green's function method is general and often easier to apply, the method of vector potentials possess certain advantages when used with the generalized MoM [16]. The method employed in this work defines the condition under which the magnetic vector potential is unique and hence facilitates consistency in the formulation and stability in the numerical implementation. The magnetic vector potential **A** is introduced into our formulation by utilizing the fact that the divergence of the curl of a vector must be zero. Using (3.3), we define the magnetic vector potential **A** as

$$\mathbf{B} = \nabla \times \mathbf{A} \tag{3.8}$$

Now substituting (3.8) into (3.1) yields

$$\nabla \times (\mathbf{E} + j\omega\mathbf{A}) = 0 \tag{3.9}$$

The quantity within the parentheses must be equal to a quantity whose curl is zero, namely a gradient [36]. This quantity is the electric scalar potential Φ. Thus, we can define the electric field **E** in terms of both a scalar and vector potential function as

$$\mathbf{E} = -\nabla\Phi - j\omega\mathbf{A} \tag{3.10}$$

Eq.(3.10) represents the general expression for **E**, and it affirms that the electric field intensity is the result of accumulating charges and changing magnetic fields. Under static conditions, (3.10) reduces to the familar

$$\mathbf{E} = -\nabla\Phi \tag{3.11}$$

In a linear, isotropic medium, the constitutive relationships defined in (3.5)–(3.7) can be used together with the definition of the magnetic vector potential and (3.10) to simplify (3.2) into

$$\nabla \times \nabla \times \mathbf{A} - \omega^2\epsilon\mu\mathbf{A} = \mu\mathbf{J} - j\omega\epsilon\mu\nabla\Phi \tag{3.12}$$

From the definition of the vector triple product, (3.12) can be written in the more familiar form

$$\nabla^2\mathbf{A} + \omega^2\epsilon\mu\mathbf{A} = \nabla(\nabla\cdot\mathbf{A}) + j\omega\epsilon\mu\nabla\Phi - \mu\mathbf{J} \tag{3.13}$$

This is one of the free space wave equations for the potential fields derived from Maxwell equations [37]. The other wave equation can be obtained by substituting (3.10) in (3.6) yielding

$$\nabla^2\Phi + j\omega\nabla\cdot\mathbf{A} = -\frac{\rho}{\epsilon} \tag{3.14}$$

Eq. (3.13) and (3.14) are the coupled potential wave equations. In order to decouple these equations, a so called gauge can be chosen. The choice of a particular gauge is arbitrary and purely for mathematical convenience. The gauge condition as it is also known results from the fact that the divergence of the magnetic vector potential **A** is not specified in its definition [37]. According to Helmholtz's theorem, if **A** is to be determined to within an additive constant, $\nabla\cdot\mathbf{A}$ and $\nabla\times\mathbf{A}$ must be specified. Since Φ is an arbitrary scalar function, we can choose a gauge that satisfies

$$\nabla\cdot\mathbf{A} = -j\omega\epsilon\mu\Phi \tag{3.15}$$

This is the Lorentz gauge condition and it reduces (3.13) and (3.14) into the following vector and scalar Helmholtz equations

$$\nabla^2\mathbf{A} + \omega^2\epsilon\mu\mathbf{A} = -\mu\mathbf{J} \tag{3.16}$$

$$\nabla^2\Phi + \omega^2\epsilon\mu\Phi = -\frac{\rho}{\epsilon} \tag{3.17}$$

From (3.17) and (3.16), we can see that the source of the scalar potential Φ is the charge density ρ, and the source of the vector potential **A** is the current density **J**. These equations are the general representation of fields in terms of the magnetic vector and electric scalar potentials. The usefulness of these equations stems from the fact that in an unbounded region, $\mathbf{A}$ and Φ are solutions to (3.16) and (3.17) [16], and they can be expressed in terms of their sources as

$$\mathbf{A}(\mathbf{r}) = \mu \int\limits_V \mathbf{J}(\mathbf{r}')G(\mathbf{r},\mathbf{r}')\ dV' \tag{3.18}$$

$$\Phi(\mathbf{r}) = \frac{1}{\epsilon} \int\limits_V \rho(\mathbf{r}')G(\mathbf{r},\mathbf{r}')\ dV' \tag{3.19}$$

where $\mathbf{r}'$ and $\mathbf{r}$ are the source and field position vectors, k represents the wave number, and $G(\mathbf{r},\mathbf{r}')$ is the scalar Green's function given by

$$G(\mathbf{r},\mathbf{r}') = \frac{e^{-jk|\mathbf{r}-\mathbf{r}'|}}{4\pi|\mathbf{r}-\mathbf{r}'|} \tag{3.20}$$

It should be noted that there is little difficulty with kernel singularity in the method of vector potential [16] since the source singularity of $G(\mathbf{r},\mathbf{r}')$ at $\mathbf{r} = \mathbf{r}'$ is integrable. The functions $G(\mathbf{r},\mathbf{r}')$ and $\mathbf{J}(\mathbf{r}')$ must satisfy the Lorentz gauge condition since $G(\mathbf{r},\mathbf{r}')$ is a solution to the following inhomogeneous scalar wave equation

$$\nabla^2 G(\mathbf{r},\mathbf{r}') + \omega^2\epsilon\mu G(\mathbf{r},\mathbf{r}') = -\delta(\mathbf{r}-\mathbf{r}') \tag{3.21}$$

Consequently, the Lorentz gauge condition for the case of a finite volume V in an unbounded region is equivalent to

$$\nabla \int\limits_V \nabla' \cdot \left[G(\mathbf{r},\mathbf{r}')\mathbf{J}(\mathbf{r}')\right]\ dV' = 0 \tag{3.22}$$

For the case of a finite V in a bounded region, the Lorentz gauge condition can only be satisfied by proper selection of the current distribution and the Green's function because of the existence of non-zero equivalent currents on the surface of V [16].

Finally, we can express (3.10) using the Lorentz gauge condition in (3.15) to get

$$\mathbf{E} = \frac{1}{j\omega\epsilon\mu}\nabla(\nabla\cdot\mathbf{A}) - j\omega\mathbf{A} \tag{3.23}$$

3.3 Basis Functions

Our numerical MoM model is based on formulating an electromagnetic scattering problem using (3.23) and providing a solution to the electric field in terms of the current density. In our model, there are two types of current densities involved: the surface current density of the conductive strips that make up the RF coil, and the volume current density in the inhomogeneous biological body. Two distinct sets of basis functions were implemented to model these current densities. The surface current density was modeled using a modified version of the RWG basis function [29], while the volume current density was modeled using the divergence-free solenoidal basis function [30]. With both basis functions, an accurate model of a loaded MRI RF coil system together with the effects of coil-tissue interactions can be implemented using the MoM.

3.3.1 Modified RWG Basis function

Of the various sets of basis functions used for surface current modeling, we decided upon a modified version of the RWG basis function [29]. These basis functions are well suited for use with the Electric Field Integral Equation (EFIE) and triangular surface discretization. For arbitrary surface modeling, the EFIE has the advantage of being applicable to both open and closed surfaces, as well as shell structures with sharp edges. Also, the use of triangular surface discretization to approximate the solution domain is particularly appropriate because of its conformability to arbitrarily shaped surfaces. We begin by assuming that the solution domain has been approximated into

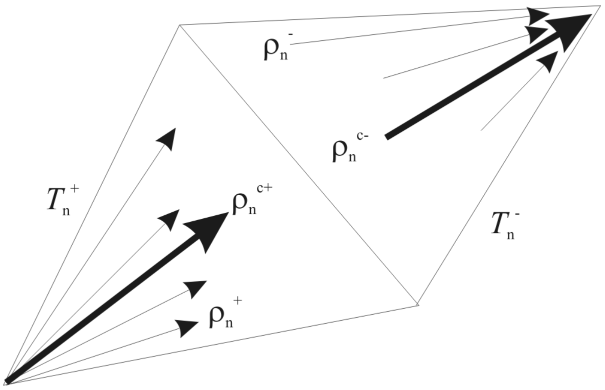

Figure 3.1: The geometrical parameters of the triangular element.

a defined set of triangular patches in terms of an appropriate enumeration of nodes, edges, faces and interior edges. The modified RWG basis function is associated with each interior edge n of the discretization domain, and defined on a pair of triangular elements T_n^+ and T_n^- sharing the edge n as shown in Fig.3.1. The designation of points on triangle T_n^+ can be either by a position vector $\mathbf{r}$ defined with respect to the origin, or by a position vector $\boldsymbol{\rho}_n^+$ defined with respect to and away from the free vertex of T_n^+. Similar designation of points apply to triangle T_n^-, but in this case $\boldsymbol{\rho}_n^-$ is directed towards the free vertex of T_n^-. The sign designation of T_n^+ and T_n^- is such that the positive current reference for edge n is chosen to be from T_n^+ to T_n^- as shown in Fig.3.1. The basis function associated with the n^{th} edge is defined as

$$\mathbf{f}_n(\mathbf{r}) = \begin{cases} \dfrac{\boldsymbol{\rho}_n^+}{2A_n^+} & \mathbf{r} \in T_n^+ \\ \dfrac{\boldsymbol{\rho}_n^-}{2A_n^-} & \mathbf{r} \in T_n^- \\ 0 & \text{otherwise} \end{cases} \tag{3.24}$$

where A_n^+ is the area of triangle T_n^+ and A_n^- is the area of triangle T_n^-. The basis function $\mathbf{f}_n(\mathbf{r})$ is a vector field that is radially diverging from the free vertex point of T_n^+, and radially converging to the free vertex point of T_n^-. Several unique properties of $\mathbf{f}_n(\mathbf{r})$ make it ideal for approximating the surface current density on triangular elements. First and foremost, $\mathbf{f}_n(\mathbf{r})$ and hence the surface current density is tangential to all edges of T_n^+ and T_n^- except the common edge n. Secondly, the normal component of $\mathbf{f}_n(\mathbf{r})$ is continuous across edge n, and thus there is no accumulation of charges on edge n. Lastly, the surface divergence of $\mathbf{f}_n(\mathbf{r})$ denoted by ∇_S can be simplified as

$$\nabla_S \cdot \mathbf{f}_n(\mathbf{r}) = \frac{\partial\big(\boldsymbol{\rho}_n^{\pm}\mathbf{f}_n(\mathbf{r})\big)}{\boldsymbol{\rho}_n^{\pm}\partial\boldsymbol{\rho}_n^{\pm}} = \begin{cases} \dfrac{1}{A_n^+} & \mathbf{r} \in T_n^+ \\ \dfrac{-1}{A_n^-} & \mathbf{r} \in T_n^- \\ 0 & \text{otherwise} \end{cases} \tag{3.25}$$

Thus from (3.25), the surface divergence of $\mathbf{f}_n(\mathbf{r})$ is constant in T_n^+ and T_n^-, and hence the total charge accumulation in the element pair T_n^+ and T_n^- is zero. The surface current density $\mathbf{J}_S(\mathbf{r})$ may be approximated in terms of $\mathbf{f}_n(\mathbf{r})$ as

$$\mathbf{J}_S(\mathbf{r}) = \sum_{n=1}^{N} I_n \mathbf{f}_n(\mathbf{r}) \tag{3.26}$$

where N is the total number of interior edges in the discretization domain. In each triangular face, a maximum of three basis functions can have nonzero values since each basis function is only associated with an interior edge. Furthermore, since the normal component of the flux of $\mathbf{f}_n(\mathbf{r})$ is unity at edge n, then the coefficient I_n in (3.26) represents the normal component of the surface current density flowing past edge n. Also, we can see that $\mathbf{f}_n(\mathbf{r})$ is independent in each element pair since the normal component of the surface current density at edge n is an independent quantity. Finally, the sum of the normal component of the surface current density at surface boundary edges on opposite sides cancel out because of continuity. Thus, we do not consider contributions from basis functions associated with such edges in (3.26).

3.3.2 Solenoidal Basis function

The solenoidal basis function is a volumetric edge-based basis function originally introduced by de Carvalho et al [30] for modeling the scattering of electromagnetic waves by inhomogeneous dielectrics. The divergence–free attribute of this basis function makes it well suited for approximating the electric flux density in inhomogeneous dielectrics since the electric flux density is solenoidal in a dielectric body. This technique was successfully implemented by [38] for modeling isolated metal-dielectric resonators. We have since expanded its use to include inhomogeneous lossy biological bodies [32]. In this case, the electric flux density is no longer divergence–free, and as such, the solenoidal basis function cannot be used to approximate it without introducing errors in the final solution. We overcame this apparent difficulty by using the solenoidal basis function to approximate the total current density in an inhomogeneous lossy body since this quantity is always divergence–free.

The divergence–free solenoidal basis function is defined within a tetrahedron as shown in Fig.3.2. It is inherently a constant vector field of the vector $\vec{AB}$ about the base edge vector $\vec{CD}$. However, this constant vector field is essentially perpendicular to the base edge vector $\vec{CD}$. As shown in Fig.3.2, the vector $\vec{CD}$ can be related to its associated tetrahedron via vectors $\vec{AB}$ or $\mathbf{e}$ and $\mathbf{d}$, where vector $\mathbf{e}$ is opposite to vector $\vec{CD}$ and vector $\mathbf{d}$ is along the minimum distance between vectors $\vec{CD}$ and $\mathbf{e}$. Also, vector $\mathbf{e}$ prescribes a counter-clockwise rotation about the base edge vector $\vec{CD}$. Thus, the basis function can be defined within a tetrahedron as a constant vector field given by

$$\mathbf{f}^V(\mathbf{r}) = \begin{cases} \dfrac{\mathbf{e}}{3V} & \mathbf{r} \in V \\ 0 & \text{otherwise} \end{cases} \tag{3.27}$$

where $\mathbf{r}$ is the position vector of a point within the tetrahedron, and V is the volume of the tetrahedron. The basis function $\mathbf{f}^V(\mathbf{r})$ as defined in (3.27) is such that its

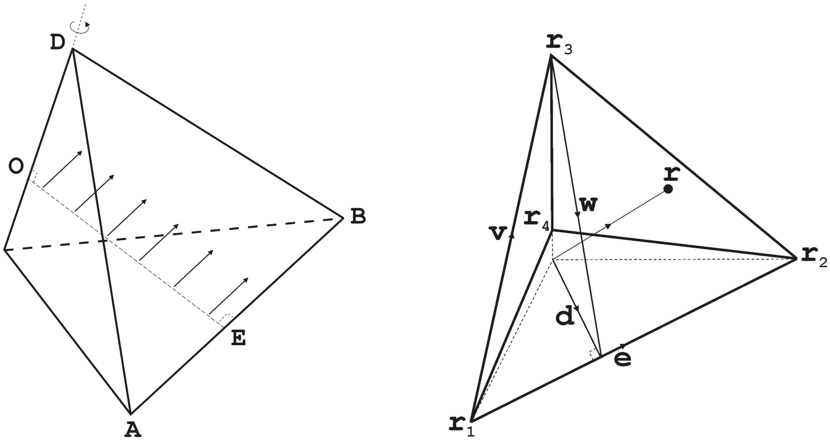

(a) **(b)**

Figure 3.2: Definition of the solenoidal basis function showing: (a) the constant vector field within the tetrahedron, (b) the individual vectors that define the basis function.

divergence within each tetraheron is zero, i.e $\nabla \cdot \mathbf{f}^V(\mathbf{r}) = 0$. Also, $\mathbf{f}^V(\mathbf{r})$ has the desired properties that the normal component of its flux is continuous across any face boundary, and the total flux of its normal component through any face is equal to one. These properties allow for the definition of a soleniodal edge element. A solenoidal edge element can thus be defined as consisting of all neighboring tetrahedra that share a common base edge vector. The basis function associated with the base edge vector is non-zero only in each tetrahedron that shares this common edge vector. A typical solenoidal edge element defined on edge *EF* is shown in Fig.3.3. In such a case where more than one tetrahedron shares an edge element, we can express the basis function

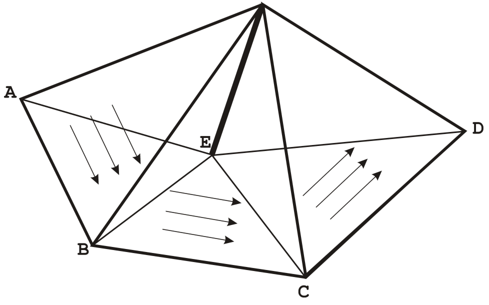

Figure 3.3: Solenoidal edge element *EF* emphasizing the divergence-free property of $\mathbf{f}_m^V(\mathbf{r})$.

associated with the edge m as

$$\mathbf{f}_m^V(\mathbf{r}) = \begin{cases} \dfrac{\mathbf{e}_n}{3V_k} & \mathbf{r} \in V_k \\ 0 & \text{otherwise} \end{cases} \tag{3.28}$$

where $k = 1, 2, \ldots, N$, V_k is the volume of the k^{th} tetrahedron, and N is the total number of tetrahedra that share the edge m. We can now define a basis set on a discretization domain consisting of tetrahedra units using (3.28). We seek to approximate the total current density by using the fact that this quantity is always solenoidal. We can show this fact by taking the divergence of (3.2) yielding

$$\begin{aligned} \nabla \cdot (\nabla \times \mathbf{H}) &= \nabla \cdot (j\omega\mathbf{D} + \mathbf{J}) \\ &= \nabla \cdot \mathbf{C} = 0 \end{aligned} \tag{3.29}$$

where we have introduced a vector quantity $\mathbf{C}(\mathbf{r})$ such that $\mathbf{C}(\mathbf{r}) = j\omega\mathbf{D}(\mathbf{r}) + \mathbf{J}(\mathbf{r})$. The quantity $\mathbf{C}(\mathbf{r})$ is the total current density which is the sum of the displacement and volume current densities. Inherently, (3.29) is a statement of the conservation of charge as expressed in the continuity equation. Thus, $\mathbf{C}(\mathbf{r})$ can conveniently be described by the solenoidal edge element. Using (3.28), we obtain

$$\mathbf{C}(\mathbf{r}) = \sum_{m=1}^{M} C_m^V \mathbf{f}_m^V(\mathbf{r}) \tag{3.30}$$

where C_m^V is the net flux of $\mathbf{C}(\mathbf{r})$ through the faces included in the elements of V_k, and M is the total number of elements in the discretization domain.

3.3.3 Selection of Linearly Independent Solenoidal Basis

It was shown in [38] that the size of the solenoidal basis set is far smaller than the total number of edges in the discretization domain. The number of linearly independent basis functions in a given discretization was shown to be

$$N_B \leq N_F - N_T \tag{3.31}$$

where N_B is the number of linearly independent basis functions, N_F is the total number of faces, and N_T is the total number of tetrahedra in the discretization. Several approaches have been reported to eliminate the linear dependence of the function set. In one approach reported in [38], the Gram or covariance matrix of a set of basis of size N was formed and reduced by row operations to an echelon form using Gauss-Jordan elimination with partial pivoting. Because this method is based on floating point arithmetic, it is particularly prone to numerical inaccuracies due to the machine precision of its implementation. As such, a non-algebraic method was proposed by [39] where the edges of the discretization are counted and tested with a set of established criteria. Unfortunately, this method cannot handle situations involving domains with holes. In order to accommodate such situations, we expanded on the work reported in [39] by including a modified algorithm with additional test criteria.

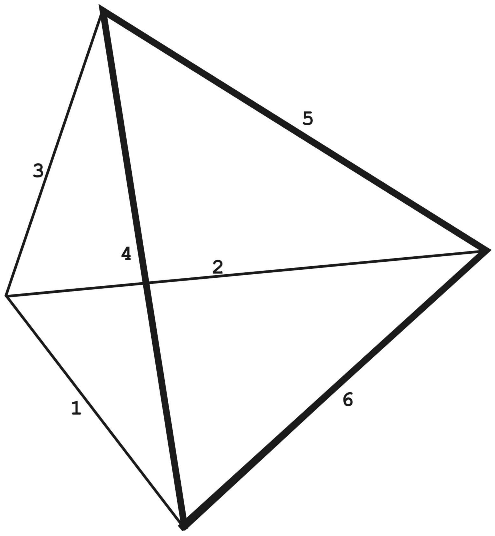

Figure 3.4: Basis set defined on a tetrahedron with bold lines denoting the independent basis edges.

In order to facilitate the selection of independent basis edges, consider a mesh with a single tetrahedron as shown in Fig.3.4. Formally, there are six defined edge elements corresponding to the six labeled edges. In $\Re^3$ space only three of these edges are truly linearly independent, and a more natural choice of these basis edges would be $\mathbf{f}_4^V(\mathbf{r})$, $\mathbf{f}_5^V(\mathbf{r})$ and $\mathbf{f}_6^V(\mathbf{r})$ as shown in Fig.3.4. These three basis edges correspond to constant vector fields defined along vectors $\mathbf{e}_1$, $\mathbf{e}_2$ and $\mathbf{e}_3$ respectively. It can be easily seen that all other edge vectors are linear combinations of these base vectors. We will introduce a more suitable expression for $\mathbf{f}_m^V(\mathbf{r})$ in (3.28) giving

$$\mathbf{f}_m^V(\mathbf{r}) = \sum_{k=1}^{N} \frac{\mathbf{e}_n}{3V_k} \mathrm{u}(\mathbf{r} \in V_k) \tag{3.32}$$

and

$$\mathrm{u}(\mathbf{r} \in V_k) = \begin{cases} 1 & \mathbf{r} \in V_k \\ \\ 0 & \text{otherwise} \end{cases} \tag{3.33}$$

where the function $\mathrm{u}(\mathbf{r} \in V_k)$ is termed the volumetric unit pulse since it has properties closely related to those of the one dimensional unit pulse function. Thus, we can express all six edge elements in Fig.3.4 using (3.32) as

$$\begin{aligned}
\mathbf{f}_1^V(\mathbf{r}) &= \frac{\mathbf{e}_5}{3V_1} \mathrm{u}(\mathbf{r} \in V_1) \\
\mathbf{f}_2^V(\mathbf{r}) &= \frac{\mathbf{e}_4}{3V_1} \mathrm{u}(\mathbf{r} \in V_1) \\
\mathbf{f}_3^V(\mathbf{r}) &= \frac{\mathbf{e}_6}{3V_1} \mathrm{u}(\mathbf{r} \in V_1) \\
\mathbf{f}_4^V(\mathbf{r}) &= \frac{\mathbf{e}_2}{3V_1} \mathrm{u}(\mathbf{r} \in V_1) \\
\mathbf{f}_5^V(\mathbf{r}) &= \frac{\mathbf{e}_1}{3V_1} \mathrm{u}(\mathbf{r} \in V_1) \\
\mathbf{f}_6^V(\mathbf{r}) &= \frac{\mathbf{e}_3}{3V_1} \mathrm{u}(\mathbf{r} \in V_1)
\end{aligned} \tag{3.34}$$

A typical mesh of the discretization domain can be constructed by the addition of more tetrahedra to the single mesh system shown in Fig.3.4. When tetrahedra are added, they will share nodes, edges or faces depending on the geometry being approximated. According to the definition in (3.32), the basis edges of each tetrahedron will be modified as tetrahedra are added that share their edges or faces, but not their nodes. Now consider a situation involving the addition of a single tetrahedron to the simple mesh system of Fig.3.4. We will highlight three possible scenarios in which both tetrahedra share a common basis edge, a common face with only one basis edge defined, or a common face with all basis edges defined as shown in Fig.3.5. For the first case shown in Fig.3.5(a), the basis edges $\mathbf{f}_6^V(\mathbf{r})$ in (3.34) will be modified according to (3.32) to yield

$$\mathbf{f}_6^V(\mathbf{r}) = \frac{\mathbf{e}_3}{3V_1}\mathrm{u}(\mathbf{r} \in V_1) + \frac{\mathbf{e}_9}{3V_2}\mathrm{u}(\mathbf{r} \in V_2) \tag{3.35}$$

From (3.31) an additional basis edge is required to form the complete basis set of (3.34) in V_1. The required basis edge can be either $\mathbf{f}_7^V(\mathbf{r})$ or $\mathbf{f}_8^V(\mathbf{r})$ since

$$\begin{aligned} \frac{\mathbf{e}_9}{3V_2}\mathrm{u}(\mathbf{r} \in V_2) &= \mathbf{f}_7^V(\mathbf{r}) \pm \mathbf{f}_{10}^V(\mathbf{r}) \\ &= \mathbf{f}_8^V(\mathbf{r}) \pm \mathbf{f}_{11}^V(\mathbf{r}) \end{aligned} \tag{3.36}$$

Similarly, the second configuration shown in Fig.3.5(b) has a complete basis set according to (3.31) and requires no additional basis edges. The edge elements in this case are given by

$$\begin{aligned} \mathbf{f}_1^V(\mathbf{r}) &= \frac{\mathbf{e}_5}{3V_1}\mathrm{u}(\mathbf{r} \in V_1) \\ \mathbf{f}_2^V(\mathbf{r}) &= \frac{\mathbf{e}_4}{3V_1}\mathrm{u}(\mathbf{r} \in V_1) + \frac{\mathbf{e}_8}{3V_2}\mathrm{u}(\mathbf{r} \in V_2) \\ \mathbf{f}_3^V(\mathbf{r}) &= \frac{\mathbf{e}_6}{3V_1}\mathrm{u}(\mathbf{r} \in V_1) + \frac{\mathbf{e}_9}{3V_2}\mathrm{u}(\mathbf{r} \in V_2) \end{aligned} \tag{3.37}$$

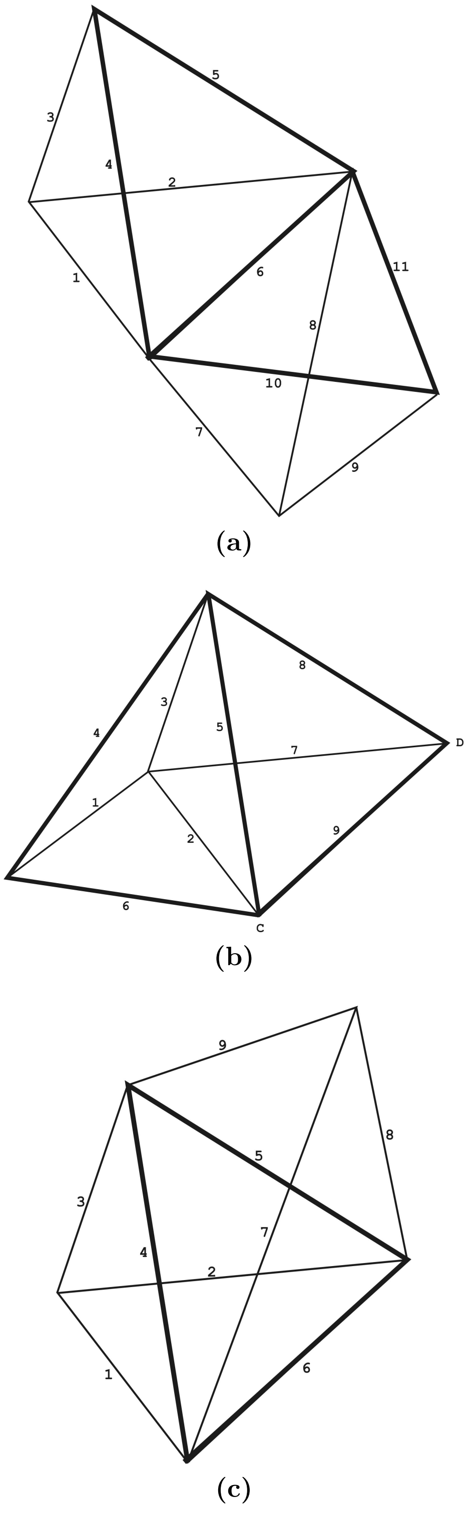

(a)

(b)

(c)

Figure 3.5: Possible orientation of a simple mesh with two tetrahedra: (a) Two tetrahedra sharing an edge, (b) two tetrahedra sharing a face that those not have all edges defined, and (c) two tetrahedra sharing a face with all edges defined. Bold lines indicate the linearly independent edges.

and

$$
\begin{aligned}
\mathbf{f}_4^V(\mathbf{r}) &= \frac{\mathbf{e}_2}{3V_1}\mathrm{u}(\mathbf{r} \in V_1) \\
\mathbf{f}_5^V(\mathbf{r}) &= \frac{\mathbf{e}_1}{3V_1}\mathrm{u}(\mathbf{r} \in V_1) + \frac{\mathbf{e}_7}{3V_2}\mathrm{u}(\mathbf{r} \in V_2) \\
\mathbf{f}_6^V(\mathbf{r}) &= \frac{\mathbf{e}_3}{3V_1}\mathrm{u}(\mathbf{r} \in V_1) \\
\mathbf{f}_7^V(\mathbf{r}) &= \frac{\mathbf{e}_5}{3V_2}\mathrm{u}(\mathbf{r} \in V_2) \\
\mathbf{f}_8^V(\mathbf{r}) &= \frac{\mathbf{e}_2}{3V_2}\mathrm{u}(\mathbf{r} \in V_2) \\
\mathbf{f}_9^V(\mathbf{r}) &= \frac{\mathbf{e}_3}{3V_2}\mathrm{u}(\mathbf{r} \in V_2)
\end{aligned}
\tag{3.38}
$$

where the basis edge elements are $\mathbf{f}_4^V(\mathbf{r})$, $\mathbf{f}_5^V(\mathbf{r})$, $\mathbf{f}_6^V(\mathbf{r})$, $\mathbf{f}_7^V(\mathbf{r})$, $\mathbf{f}_8^V(\mathbf{r})$ and $\mathbf{f}_9^V(\mathbf{r})$, since

$$
\begin{aligned}
\mathbf{f}_1^V(\mathbf{r}) &= \mathbf{f}_4^V(\mathbf{r}) \pm \mathbf{f}_6^V(\mathbf{r}) \\
\mathbf{f}_2^V(\mathbf{r}) &= \Big[(\mathbf{f}_5^V(\mathbf{r}) \pm \mathbf{f}_6^V(\mathbf{r})\Big] \pm \mathbf{f}_9^V(\mathbf{r}) \\
\mathbf{f}_3^V(\mathbf{r}) &= \Big[(\mathbf{f}_4^V(\mathbf{r}) \pm \mathbf{f}_5^V(\mathbf{r})\Big] \pm \mathbf{f}_8^V(\mathbf{r}) \\
\mathbf{f}_7^V(\mathbf{r}) &= \mathbf{f}_8^V(\mathbf{r}) \pm \mathbf{f}_9^V(\mathbf{r})
\end{aligned}
\tag{3.39}
$$

Lastly, we consider the configuration shown in Fig.3.5(c) where two tetrahedra share a common face that has all edges defined as basis edges. In this particular case, the basis edges of the simple mesh are modified as

$$
\begin{aligned}
\mathbf{f}_4^V(\mathbf{r}) &= \frac{\mathbf{e}_2}{3V_1}\mathrm{u}(\mathbf{r} \in V_1) + \frac{\mathbf{e}_8}{3V_2}\mathrm{u}(\mathbf{r} \in V_2) \\
\mathbf{f}_5^V(\mathbf{r}) &= \frac{\mathbf{e}_1}{3V_1}\mathrm{u}(\mathbf{r} \in V_1) + \frac{\mathbf{e}_7}{3V_2}\mathrm{u}(\mathbf{r} \in V_2) \\
\mathbf{f}_6^V(\mathbf{r}) &= \frac{\mathbf{e}_3}{3V_1}\mathrm{u}(\mathbf{r} \in V_1) + \frac{\mathbf{e}_9}{3V_2}\mathrm{u}(\mathbf{r} \in V_2)
\end{aligned}
\tag{3.40}
$$

and thus the system requires the addition of two more basis edges in order to satisfy (3.32). It can easily be shown that these additional basis edges can be chosen from the set $\{\mathbf{f}_7^V(\mathbf{r}),\ \mathbf{f}_8^V(\mathbf{r}),\ \mathbf{f}_9^V(\mathbf{r})\}$ since we have the condition that

$$\mathbf{f}_7^V(\mathbf{r}) + \mathbf{f}_8^V(\mathbf{r}) + \mathbf{f}_9^V(\mathbf{r}) = 0 \tag{3.41}$$

Thus, we can expressed the remaining edge elements as

$$\begin{aligned}
\mathbf{f}_1^V(\mathbf{r}) &= \left[\mathbf{f}_4^V(\mathbf{r}) \pm \mathbf{f}_6^V(\mathbf{r})\right] \pm \mathbf{f}_7^V(\mathbf{r}) \\
\mathbf{f}_2^V(\mathbf{r}) &= \left[\mathbf{f}_5^V(\mathbf{r}) \pm \mathbf{f}_6^V(\mathbf{r})\right] \pm \mathbf{f}_8^V(\mathbf{r}) \\
\mathbf{f}_3^V(\mathbf{r}) &= \left[\mathbf{f}_4^V(\mathbf{r}) \pm \mathbf{f}_5^V(\mathbf{r})\right] \pm \mathbf{f}_9^V(\mathbf{r})
\end{aligned} \tag{3.42}$$

From these test considerations, we develop a selection algorithm to extract the linearly independent edges from the set of all edges. For simplicity, we assume that the mesh is made up of a single volume with one or more holes or voids. The selection algorithm is outlined graphically in Fig.3.6. The first step is to pick an arbitrary node as the first or head node in a linked list. A linked list is a fundamental data structure that is made up of a sequence of data items with each item containing a data field as well as one or two references or links that allow access to the next or previous data item. The main benefits of a linked list include the facility to insert and remove data items at any point in the list, and the ability to traverse the linked items in a different order than that used to store the items in memory or on disk. A simple linked list is shown in Fig.3.7. With the head node defined we proceed to pick a node from the list; the seed node. We find all tetrahedra sharing this node and validate each one against the test configurations shown in Fig.3.5. If any tetrahedron fails the validation process then the seed node is removed and inserted at the end of the list. Upon successful validation, the independent edges are identified as the edges of the tetrahedra that do not include the seed node. All other nodes of the tetrahedra are appended to the end of the list. The procedure is repeated until all nodes in the mesh are exhausted. The total number of independent edges in a given mesh discretization can be found

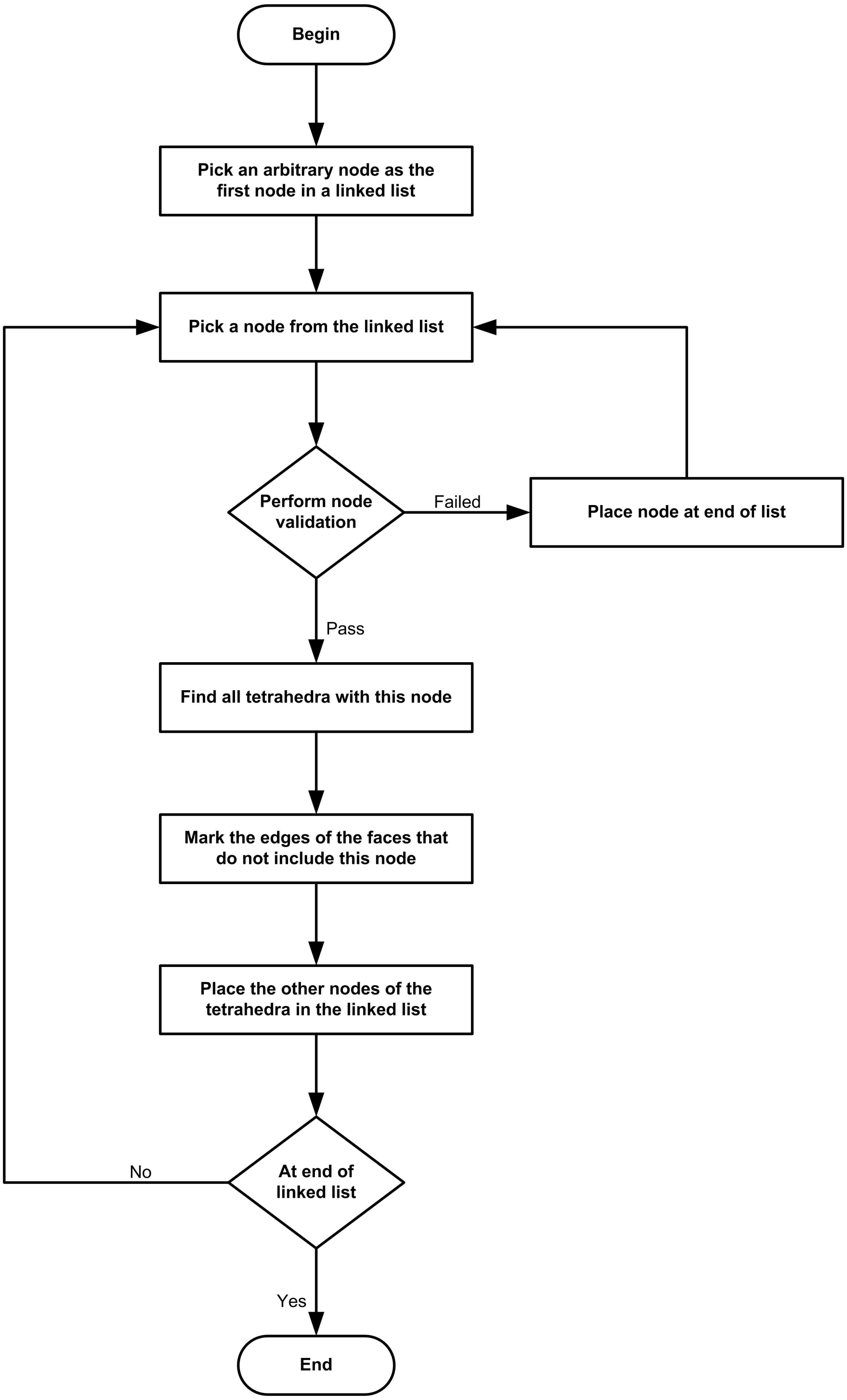

Figure 3.6: Selection algorithm for identifying linearly independent edges.

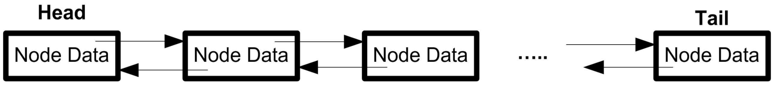

Figure 3.7: A simple linked list structure showing reference pointers to the previous and next data items.

using

$$N_B = N_F - N_T - N_{voids} \tag{3.43}$$

where N_{voids} is the total number of voids in the mesh domain. Eq.(3.43) can be explained by considering a mesh system with no voids. When an internal tetrahedron is removed, a void is created in its place. In this situation, the number of independent edges will not change since the void is completely surrounded by the remaining tetrahedra. Consequently, the number of voids have to be subtracted from (3.31) yielding (3.43) in order to account for the inclusion of voids. Furthermore, the inclusion of holes in the mesh discretization does not affect (3.31) as previously reported by [39]. This can be explained by considering the smallest hole that can be accommodated in the mesh. This hole is created by removing exactly one tetrahedron and one face from the mesh. Much bigger holes can be thought of as a collection of these small holes. In effect, (3.31) need not be modified as the difference between the total number of faces and tetrahedra will be constant for all situations where holes exist in the discretization domain.

3.4 Derivation of the Method of Moment Integral Equations

In this section, we discuss the derivation of the integral equations that are needed for modeling MRI RF coils using the Method of Moments. These equations are derived by enforcing known boundary conditions in terms of the unknown current distributions in a volume, or on a finite boundary subjected to a known source of excitation. In this case the volume of interest is the inhomogeneous biological insert while the finite

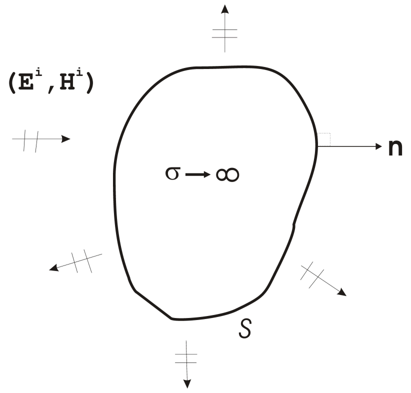

Figure 3.8: A perfect conducting body illuminated by an incident electromagnetic wave.

boundary is the surface of the conductive strips that constitutes the RF coil. As such, three different equations are needed to completely characterize the model based on the interactions between the inhomogeneous volume and the finite conductive boundary. These equations are categorized as the surface-surface, volume-volume and surface-volume MoM equations respectively.

3.4.1 Surface-Surface MoM Equation

Fig.3.8 depicts a simple situation involving the illumination of a highly conductive body by an incident electromagnetic wave $(\mathbf{E}^i, \mathbf{H}^i)$. We will apply (3.23) to this problem and also enforce the boundary condition that the tangential component of the electric field $\mathbf{E}$ must vanish on the surface S of a perfect conducting body. This can be stated more concisely in the form

$$\mathbf{n} \times (\mathbf{E}^i + \mathbf{E}^s) = 0 \tag{3.44}$$

where the vector $\mathbf{n}$ is the outward surface normal of S as shown in Fig.3.8. The scattered electric field $\mathbf{E}^s$ is generated by induced charges and surface currents on the surface S. Consequently, this reduces the solution domain to the surface of the conductive body with all integral equations reduced to surface integral equations. The

Surface-Surface MoM equation is a consequence of enforcing the boundary condition on S, and it takes the form

$$\mathbf{n} \times \left[\mathbf{E}^i + \frac{1}{j\omega\epsilon\mu} \nabla\nabla \cdot \mathbf{A}(\mathbf{r}) - j\omega \mathbf{A}(\mathbf{r}) \right] = 0 \tag{3.45}$$

where according to (3.18), the magnetic vector potential becomes

$$\mathbf{A}(\mathbf{r}) = \mu \int_S \mathbf{J}(\mathbf{r}') G(\mathbf{r}, \mathbf{r}') \; dS \tag{3.46}$$

and S is assumed to be completely enclosed in a linear, isotropic medium. We can now let the surface S be discretized into triangular patch elements with each interior edge n associated with the RWG basis function $\mathbf{f}_n(\mathbf{r})$. The surface current density on S can then be expanded in terms of the basis function $\mathbf{f}_n$ as

$$\mathbf{J}(\mathbf{r}') \approx \sum_{n=1}^{N} I_n \mathbf{f}_n(\mathbf{r}') \tag{3.47}$$

where N is the total number of interior edges in the discretization. It is worthwhile to mention that the boundary edges are not associated with $\mathbf{f}_n(\mathbf{r}')$ since the normal component of current at a true boundary edge must vanish. Also, since we associate a basis function with each interior edge, the current density in each triangular patch element has at most three associated basis functions. Thus, the coefficients I_n in (3.47) denote the normal component of the surface current density flowing through the n^{th} interior edge, since the normal component of $\mathbf{f}_n(\mathbf{r}')$ is unity at each edge. With the surface current density defined, our goal is to transform (3.45) into a linear system of equations. In addition, our MRI RF coil model is not excited by an incident electric field, thus $\mathbf{E}^i$ in (3.45) is zero. Also, the solution domain is discretized into triangular patch elements allowing us to approximate (3.46) as

$$\mathbf{A}(\mathbf{r}) \approx \mu \sum_{u=1}^{M} \int_{T_u} \mathbf{J}(\mathbf{r}')G(\mathbf{r},\mathbf{r}')\ dT_u \tag{3.48}$$

with M denoting the total number of triangular patch elements and T_u representing the u^{th} triangular patch element. By using the definition of $\mathbf{J}(\mathbf{r}')$ in (3.47), we can further express (3.48) as

$$\mathbf{A}(\mathbf{r}) \approx \mu \sum_{u=1}^{M} \sum_{n=1}^{N} I_n \int_{T_u} \mathbf{f}_n(\mathbf{r}')G(\mathbf{r},\mathbf{r}')\ dT_u \tag{3.49}$$

Now let an arbitrary tangential vector $\mathbf{m}$ be defined on the discretized surface S. A necessary and sufficient condition for (3.45) to be valid is that

$$\frac{1}{j\omega\epsilon\mu}\mathbf{m} \cdot \nabla\nabla \cdot \mathbf{A}(\mathbf{r}) - j\omega\mathbf{m} \cdot \mathbf{A}(\mathbf{r}) = 0 \tag{3.50}$$

For simplicity, if we choose the tangent vector $\mathbf{m}$ to be $\mathbf{f}_m(\mathbf{r})$ in (3.50) and integrate the dot product over the domain S, we obtain

$$\sum_{v=1}^{M} \sum_{m=1}^{N} \left[\frac{1}{j\omega\epsilon\mu} \int_{T_v} \mathbf{f}_m(\mathbf{r}) \cdot \nabla\nabla \cdot \mathbf{A}(\mathbf{r})\ dT_v - j\omega \int_{T_v} \mathbf{f}_m(\mathbf{r}) \cdot \mathbf{A}(\mathbf{r})\ dT_v \right] = 0 \tag{3.51}$$

Furthermore, we see that (3.51) constitutes a well defined set of MoM equations with a Galerkin type enforcement condition since $\mathbf{f}_m(\mathbf{r})$ and $\mathbf{f}_n(\mathbf{r}')$ are denoted using the same basis definition. In general, the Galerkin method employing identical weighting and basis functions in the MoM formulation yields more accurate numerical results when compared to other MoM methods under similar computational constraints [16]. This is attributable to the fact that both energy and reciprocity are preserved in the approximate solution by using a scalar product with a real-valued basis function.

In order to simplify (3.51), we note the relationship that

$$\begin{aligned}\int\limits_{T_v} \mathbf{f}_m(\mathbf{r}) \cdot \nabla\nabla \cdot \mathbf{A}(\mathbf{r})\ dT_v &= \int\limits_{T_v} \nabla \cdot \Big[\nabla \cdot \mathbf{A}(\mathbf{r})\mathbf{f}_m(\mathbf{r})\Big]\ dT_v - \int\limits_{T_v} \nabla \cdot \mathbf{A}(\mathbf{r}) \nabla \cdot \mathbf{f}_m(\mathbf{r})\ dT_v \\ &= -\int\limits_{T_v} \nabla \cdot \mathbf{A}(\mathbf{r}) \nabla \cdot \mathbf{f}_m(\mathbf{r})\ dT_v\end{aligned} \tag{3.52}$$

since $\mathbf{f}_m(\mathbf{r})$ is tangent to the surface S and

$$\int\limits_{T_v} \nabla \cdot \Big[\nabla \cdot \mathbf{A}(\mathbf{r})\mathbf{f}_m(\mathbf{r})\Big]\ dT_v = \int\limits_{\partial T_v} \nabla \cdot \mathbf{A}(\mathbf{r})\mathbf{f}_m(\mathbf{r}) \cdot \mathbf{n}\ d\partial T_v = 0 \tag{3.53}$$

Thus, we can now write (3.51) as

$$\sum_{v=1}^{M}\sum_{m=1}^{N}\left[\frac{1}{j\omega\epsilon\mu}\int\limits_{T_v} \nabla \cdot \mathbf{f}_m(\mathbf{r})\nabla \cdot \mathbf{A}(\mathbf{r})\ dT_v + j\omega \int\limits_{T_v} \mathbf{f}_m(\mathbf{r}) \cdot \mathbf{A}(\mathbf{r})\ dT_v\right] = 0 \tag{3.54}$$

Using (3.48), we can simplify $\nabla \cdot \mathbf{A}(\mathbf{r})$ into

$$\begin{aligned}\nabla \cdot \mathbf{A}(\mathbf{r}) &= \mu \sum_{u=1}^{M} \int\limits_{T_u} \nabla \cdot \Big[\mathbf{J}(\mathbf{r}')G(\mathbf{r},\mathbf{r}')\Big]\ dT_u \\ &= \mu \sum_{u=1}^{M} \int\limits_{T_u} \mathbf{J}(\mathbf{r}') \cdot \nabla G(\mathbf{r},\mathbf{r}')\ dT_u \\ &= \mu \sum_{u=1}^{M} \int\limits_{T_u} G(\mathbf{r},\mathbf{r}')\nabla' \cdot \mathbf{J}(\mathbf{r}')\ dT_u - \mu \sum_{u=1}^{M} \int\limits_{T_u} \nabla' \cdot \Big[\mathbf{J}(\mathbf{r}')G(\mathbf{r},\mathbf{r}')\Big]\ dT_u \\ &= \mu \sum_{u=1}^{M} \int\limits_{T_u} G(\mathbf{r},\mathbf{r}')\nabla' \cdot \mathbf{J}(\mathbf{r}')\ dT_u - \mu \sum_{u=1}^{M} \int\limits_{\partial T_u} G(\mathbf{r},\mathbf{r}')\mathbf{J}(\mathbf{r}') \cdot \mathbf{n}\ d\partial T_u \\ &= \mu \sum_{u=1}^{M} \int\limits_{T_u} G(\mathbf{r},\mathbf{r}')\nabla' \cdot \mathbf{J}(\mathbf{r}')\ dT_u\end{aligned} \tag{3.55}$$

since

$$\mu \sum_{u=1}^{M} \int\limits_{\partial T_u} G(\mathbf{r}, \mathbf{r}')\mathbf{J}(\mathbf{r}') \cdot \mathbf{n} \; d\partial T_u = 0 \tag{3.56}$$

and $\mathbf{J}(\mathbf{r}')$ is defined along the surface tangent as indicated in (3.47). Finally, we define the Surface-Surface MoM equation as

$$\begin{aligned} \sum_{\substack{v=1\\u=1}}^{M} \sum_{\substack{n=1\\m=1}}^{N} I_n \Bigg[\frac{1}{j\omega\epsilon} \int\limits_{T_u} \int\limits_{T_v} \nabla \cdot \mathbf{f}_m(\mathbf{r}) \nabla' \cdot \mathbf{f}_n(\mathbf{r}') G(\mathbf{r}, \mathbf{r}') \; dT_u dT_v \\ + j\omega\mu \int\limits_{T_u} \int\limits_{T_v} \mathbf{f}_m(\mathbf{r}) \cdot \mathbf{f}_n(\mathbf{r}') G(\mathbf{r}, \mathbf{r}') \; dT_u dT_v \Bigg] = 0 \end{aligned} \tag{3.57}$$

3.4.2 Volume-Volume MoM Equation

In this section, we present the derivation of the Volume-Volume MoM integral equation for modeling the electromagnetic scattering by an inhomogeneous material body. The Volume-Volume MoM integral equation is derived from the volume Electric Field Integral Equation (EFIE) as written in (3.23), while utilizing the divergence–free property of the solenoidal basis function [30]. The solution of the resulting Volume-Volume MoM integral equation can then be obtained using the method of volume integral equation as described in [29]. This method has the advantage of being easily applicable to problems involving inhomogeneous material bodies [28], as well as providing much better accuracy at the resonances of Eigenmode problems [40]. On the other hand, its computational complexity increases with increasing grid size, but the use of the divergence–free solenoidal basis function will provide a reduction in the number of unknowns with possible improvements in overall system performance.

In deriving the Volume-Volume MoM integral equation, we note that the electric field $\mathbf{E}(\mathbf{r})$ and the magnetic field $\mathbf{B}(\mathbf{r})$ can both be described in terms of the magnetic vector potential $\mathbf{A}(\mathbf{r})$ as in (3.23) and (3.8), where $\mathbf{A}(\mathbf{r})$ is as defined in (3.18). In an inhomogeneous material body characterized by permittivity $\epsilon_0\epsilon_r(\mathbf{r})$ and conductance

$\sigma(\mathbf{r})$ and bounded by volume V, the volume equivalence principle [29] allows us to replace the inhomogeneous body by an equivalent volume current density $\widetilde{\mathbf{J}}(\mathbf{r})$ in V. The equivalent volume current density $\widetilde{\mathbf{J}}(\mathbf{r})$ can be obtained from (3.2) by using

$$\begin{aligned}\nabla \times \mathbf{H}(\mathbf{r}) &= j\omega\mathbf{D}(\mathbf{r}) + \mathbf{J}(\mathbf{r}) \\ &= j\omega\mathbf{D}(\mathbf{r}) - j\omega\epsilon_0\mathbf{E}(\mathbf{r}) + j\omega\epsilon_0\mathbf{E}(\mathbf{r}) + \mathbf{J}(\mathbf{r}) \\ &= j\omega\epsilon_0\mathbf{E}(\mathbf{r}) + \widetilde{\mathbf{J}}(\mathbf{r})\end{aligned} \tag{3.58}$$

where $\widetilde{\mathbf{J}}(\mathbf{r})$ is defined as

$$\widetilde{\mathbf{J}}(\mathbf{r}) = \mathbf{J}(\mathbf{r}) + j\omega(\mathbf{D}(\mathbf{r}) - \epsilon_0\mathbf{E}(\mathbf{r})) \tag{3.59}$$

With $\widetilde{\mathbf{J}}(\mathbf{r})$ defined, we can now replace the volume current density $\mathbf{J}(\mathbf{r})$ in (3.18) by $\widetilde{\mathbf{J}}(\mathbf{r})$. For the case where the inhomogeneous body is illuminated by an incident electromagnetic wave $\mathbf{E}^i(\mathbf{r})$, the volume EFIE [28] is given by

$$\mathbf{E}(\mathbf{r}) = \mathbf{E}^i(\mathbf{r}) + \frac{1}{j\omega\epsilon_0\mu_0}\nabla\nabla\cdot\mathbf{A}(\mathbf{r}) - j\omega\mathbf{A}(\mathbf{r}) \tag{3.60}$$

We previously introduced the vector quantity $\mathbf{C}(\mathbf{r})$ such that $\mathbf{C}(\mathbf{r}) = j\omega\mathbf{D}(\mathbf{r}) + \mathbf{J}(\mathbf{r})$. The quantity $\mathbf{C}(\mathbf{r})$ is defined as the total volume current density and is a consequence of the conservation of charge continuity. From (3.29), we see that $\mathbf{C}(\mathbf{r})$ is divergence-free, i.e $\nabla\cdot\mathbf{C}(\mathbf{r}) = 0$. Thus, $\mathbf{C}(\mathbf{r})$ can conveniently be described by the divergence-free solenoidal basis function as defined in (3.30). Next, we express the net electric field $\mathbf{E}(\mathbf{r})$ and $\widetilde{\mathbf{J}}(\mathbf{r})$ in terms of $\mathbf{C}(\mathbf{r})$ yielding

$$\mathbf{E}(\mathbf{r}) = \Big[\frac{1}{j\omega\epsilon_r(\mathbf{r})\epsilon_0 + \sigma(\mathbf{r})}\Big]\mathbf{C}(\mathbf{r}) = k_1(\mathbf{r})\mathbf{C}(\mathbf{r}) \tag{3.61}$$

$$\widetilde{\mathbf{J}}(\mathbf{r}) = \Big[1 - \frac{j\omega\epsilon_0}{j\omega\epsilon_r(\mathbf{r})\epsilon_0 + \sigma(\mathbf{r})}\Big]\mathbf{C}(\mathbf{r}) = k_2(\mathbf{r})\mathbf{C}(\mathbf{r}) \tag{3.62}$$

The new scalar quantities $k_1(\mathbf{r})$ and $k_2(\mathbf{r})$ are dependent only on the material properties of the body. Thus, we can now substitute (3.61) and (3.62) in (3.60) giving

$$\begin{aligned}\mathbf{E}^i(\mathbf{r}) = k_1(\mathbf{r})\mathbf{C}(\mathbf{r}) + j\omega\mu_0 \int\limits_V k_2(\mathbf{r}')G(\mathbf{r},\mathbf{r}')\mathbf{C}(\mathbf{r}')\ dV \\ - \frac{1}{j\omega\epsilon_0}\nabla \int\limits_V \nabla \cdot k_2(\mathbf{r}')G(\mathbf{r},\mathbf{r}')\mathbf{C}(\mathbf{r}')\ dV\end{aligned} \tag{3.63}$$

We can further simplify (3.63) into

$$\begin{aligned}\mathbf{E}^i(\mathbf{r}) = k_1(\mathbf{r})\mathbf{C}(\mathbf{r}) + j\omega\mu_0 \int\limits_V k_2(\mathbf{r}')G(\mathbf{r},\mathbf{r}')\mathbf{C}(\mathbf{r}')\ dV \\ + \frac{1}{j\omega\epsilon_0}\nabla \int\limits_S k_2(\mathbf{r}')G(\mathbf{r},\mathbf{r}')\mathbf{C}(\mathbf{r}') \cdot \mathbf{u}\ dS\end{aligned} \tag{3.64}$$

where we have utilized the fact that

$$\begin{aligned}\int\limits_V \nabla \cdot k_2(\mathbf{r}')G(\mathbf{r},\mathbf{r}')\mathbf{C}(\mathbf{r}')\ dV &= \int\limits_V k_2(\mathbf{r}')\mathbf{C}(\mathbf{r}') \cdot \nabla G(\mathbf{r},\mathbf{r}')\ dV \\ &= -\int\limits_V k_2(\mathbf{r}')\mathbf{C}(\mathbf{r}') \cdot \nabla' G(\mathbf{r},\mathbf{r}')\ dV \\ &= -\int\limits_V \nabla' \cdot k_2(\mathbf{r}')G(\mathbf{r},\mathbf{r}')\mathbf{C}(\mathbf{r}')\ dV \\ &= -\int\limits_S k_2(\mathbf{r}')G(\mathbf{r},\mathbf{r}')\mathbf{C}(\mathbf{r}') \cdot \mathbf{u}\ dS\end{aligned} \tag{3.65}$$

The vector $\mathbf{u}$ is the unit normal on the surface S that encloses the volume V. Also, (3.65) is a consequence of the divergence theorem where the volume integral is transformed into a much simpler surface integral. Next, the inhomogeneous material volume V is discretized into N tetrahedra elements resulting in the transformation of

(3.64) into

$$\mathbf{E}^i(\mathbf{r}) \approx \sum_{m=1}^{M} C_m^V k_1(\mathbf{r})\mathbf{f}_m^V(\mathbf{r}) + j\omega\mu_0 \sum_{u=1}^{N}\sum_{m=1}^{M} C_m^V \int\limits_{V_u} k_2(\mathbf{r}')G(\mathbf{r},\mathbf{r}')\mathbf{f}_m^V(\mathbf{r}')\ dV_u + \frac{1}{j\omega\epsilon_0}\nabla \sum_{u=1}^{N}\sum_{m=1}^{M} C_m^V \int\limits_{S_u} k_2(\mathbf{r}')G(\mathbf{r},\mathbf{r}')\mathbf{f}_m^V(\mathbf{r}')\cdot\mathbf{u}_u\ dS_u \tag{3.66}$$

We now implement a Galerkin type enforcement condition by multiplying (3.66) with the weighting function $k_2(\mathbf{r})\mathbf{f}_n^V(\mathbf{r})$ and integrating over the inhomogeneous volume V. Here again, the integral of $k_2(\mathbf{r})\mathbf{f}_n^V(\mathbf{r})$ with the gradient term in (3.66) is simplified using the divergence theorem and the solenoidal property of $\mathbf{f}_n^V(\mathbf{r})$. Overall, this gives the $M \times M$ moment equation in the form

$$\sum_{v=1}^{N}\sum_{n=1}^{M} \int\limits_{V_v} k_2(\mathbf{r})\mathbf{f}_n^V(\mathbf{r})\cdot\mathbf{E}^i(\mathbf{r})\ dV_v = \sum_{v=1}^{N}\sum_{m,n=1}^{M} C_m^V \int\limits_{V_v} k_1(\mathbf{r})k_2(\mathbf{r}')\mathbf{f}_m^V(\mathbf{r}')\cdot\mathbf{f}_n^V(\mathbf{r})\ dV_v + j\omega\mu_0 \sum_{u,v=1}^{N}\sum_{m,n=1}^{M} C_m^V \int\limits_{V_u}\int\limits_{V_v} k_2(\mathbf{r}')k_2(\mathbf{r})\mathbf{f}_m^V(\mathbf{r}')\cdot\mathbf{f}_n^V(\mathbf{r})\ G(\mathbf{r},\mathbf{r}')\ dV_u dV_v + \frac{1}{j\omega\epsilon_0} \sum_{u,v=1}^{N}\sum_{m,n=1}^{M} C_m^V \int\limits_{S_u}\int\limits_{S_v} k_2(\mathbf{r}')k_2(\mathbf{r})\mathbf{f}_m^V(\mathbf{r}')\cdot\mathbf{u}_u\ \mathbf{f}_n^V(\mathbf{r})\cdot\mathbf{u}_v\ G(\mathbf{r},\mathbf{r}')\ dS_u dS_v \tag{3.67}$$

3.4.3 Surface-Volume MoM Equation

The formulation of the surface-volume MoM equation is based on the VIE approach presented in [41] with the combined use of the RWG basis function and the solenoidal basis function. The result is fundamentally a combination of (3.57) and (3.67), plus an additional component that describes the interaction between the conductive surface and the inhomogeneous volume. The derivation process involves formulating a scattering problem as described by

$$\mathbf{E}(\mathbf{r}) = \mathbf{E}^i(\mathbf{r}) + \mathbf{E}^s(\mathbf{r}) \tag{3.68}$$

In this case, the total electric field $\mathbf{E}(\mathbf{r})$ is the vector sum of the incident electric field $\mathbf{E}^i(\mathbf{r})$ and the scattered electric field $\mathbf{E}^s(\mathbf{r})$, where $\mathbf{E}^s(\mathbf{r})$ is given by (3.23). We will further assume that there is no incident field in the vicinity. Let the conductive surface be bounded by surface S, whereas the inhomogeneous material volume V be bounded by surface S_V. Once again, we will assign electrical permittivity $\epsilon_0\epsilon_r(\mathbf{r})$ and electrical conductivity $\sigma(\mathbf{r})$ to the inhomogeneous body in V. The scattered field $\mathbf{E}^s(\mathbf{r})$ is composed of two components owing to the composite nature of the structure. The first component $\mathbf{E}^s_S(\mathbf{r})$ is due to the volume polarization current $\widetilde{\mathbf{J}}(\mathbf{r}')$ in V, while the other component $\mathbf{E}^s_V(\mathbf{r})$ arises from the surface current $\mathbf{J}(\mathbf{r}')$ on S. Thus, we can conveniently express $\mathbf{E}^s(\mathbf{r})$ as

$$\mathbf{E}^s(\mathbf{r}) = \mathbf{E}^s_S(\mathbf{r}) + \mathbf{E}^s_V(\mathbf{r}) \tag{3.69}$$

with

$$\mathbf{E}^s_S(\mathbf{r}) = -j\omega\mu_0 \int\limits_S \mathbf{J}(\mathbf{r}')G(\mathbf{r},\mathbf{r}')\ dS + \frac{1}{j\omega\epsilon_0}\nabla \int\limits_S G(\mathbf{r},\mathbf{r}')\nabla'\cdot\mathbf{J}(\mathbf{r}')\ dS \tag{3.70}$$

$$\mathbf{E}^s_V(\mathbf{r}) = -j\omega\mu_0 \int\limits_V \widetilde{\mathbf{J}}(\mathbf{r}')G(\mathbf{r},\mathbf{r}')\ dV - \frac{1}{j\omega\epsilon_0}\nabla \int\limits_{S_V} G(\mathbf{r},\mathbf{r}')\widetilde{\mathbf{J}}(\mathbf{r}')\cdot\mathbf{u}\ dS_V \tag{3.71}$$

The inhomogeneous volume V is discretized into N_V tetrahedra elements, and the conductive surface S is discretized into N_S triangular elements. The volume polarization current $\widetilde{\mathbf{J}}(\mathbf{r}')$ in V and the surface current $\mathbf{J}(\mathbf{r}')$ on S are as defined in (3.62), (3.30) and (3.26). Since two different basis functions were used to approximate $\widetilde{\mathbf{J}}(\mathbf{r}')$ and $\mathbf{J}(\mathbf{r}')$, a Galerkin type enforcement will involve testing with both $\mathbf{f}_n(\mathbf{r})$

and $k_2(\mathbf{r})\mathbf{f}_n^V(\mathbf{r})$ on (3.68). Thus, there will be two surface-volume MoM equations that can be expressed in the form

$$\begin{aligned}\sum_{v=1}^{N_S}\sum_{n=1}^{M_S}\int\limits_{T_v}\mathbf{f}_n(\mathbf{r})\cdot\mathbf{E}(\mathbf{r})\ dT_v = \\ \sum_{v=1}^{N_S}\sum_{n=1}^{M_S}\Big(\int\limits_{T_v}\mathbf{f}_n(\mathbf{r})\cdot\mathbf{E}_S^s(\mathbf{r})\ dT_v + \int\limits_{T_v}\mathbf{f}_n(\mathbf{r})\cdot\mathbf{E}_V^s(\mathbf{r})\ dT_v\Big)\end{aligned} \tag{3.72}$$

$$\begin{aligned}\sum_{v=1}^{N_V}\sum_{n=1}^{M_V}\int\limits_{V_v}k_2(\mathbf{r})\mathbf{f}_n^V(\mathbf{r})\cdot\mathbf{E}(\mathbf{r})\ dV_v = \\ \sum_{v=1}^{N_V}\sum_{n=1}^{M_V}\Big(\int\limits_{V_v}k_2(\mathbf{r})\mathbf{f}_n^V(\mathbf{r})\cdot\mathbf{E}_S^s(\mathbf{r})\ dV_v + \int\limits_{V_v}k_2(\mathbf{r})\mathbf{f}_n^V(\mathbf{r})\cdot\mathbf{E}_V^s(\mathbf{r})\ dV_v\Big)\end{aligned} \tag{3.73}$$

The first term on the left-hand side of (3.72) should ideally be zero since $\mathbf{f}_n(\mathbf{r})$ is orthogonal to $\mathbf{E}(\mathbf{r})$ on the conductive surface S. Also, the first term on the right-hand side of (3.72) simplifies into (3.57). Similarly, the first term on the left-hand side of (3.73) minus the second term on the right-hand side (3.73) simplifies to (3.67) when the incident field $\mathbf{E}^i(\mathbf{r})$ is zero. The second term on the right-hand side of (3.72) can be expanded into

$$\begin{aligned}-\sum_{v=1}^{N_S}\sum_{n=1}^{M_S}\int\limits_{T_v}\mathbf{f}_n(\mathbf{r})\cdot\mathbf{E}_V^s(\mathbf{r})\ dT_v = \\ j\omega\mu_0\sum_{u=1}^{N_V}\sum_{v=1}^{N_S}\sum_{m=1}^{M_V}\sum_{n=1}^{M_S}C_m^V\int\limits_{T_v}\int\limits_{V_u}k_2(\mathbf{r}')\mathbf{f}_n(\mathbf{r})\cdot\mathbf{f}_m^V(\mathbf{r}')\ G(\mathbf{r},\mathbf{r}')\ dV_u dT_v \\ -\frac{1}{j\omega\epsilon_0}\sum_{u=1}^{N_V}\sum_{v=1}^{N_S}\sum_{m=1}^{M_V}\sum_{n=1}^{M_S}C_m^V\int\limits_{T_v}\int\limits_{S_u}k_2(\mathbf{r}')\nabla\cdot\mathbf{f}_n(\mathbf{r})\ \mathbf{f}_m^V(\mathbf{r}')\cdot\mathbf{u}_u\ G(\mathbf{r},\mathbf{r}')\ dS_u dT_v\end{aligned} \tag{3.74}$$

where the divergence theorem and standard vector identities have been used to transform the integral of $\mathbf{f}_n(\mathbf{r})$ with the gradient term in (3.70). Similarly, evaluation of the first term on the right-hand side of (3.73) gives

$$
\begin{aligned}
&-\sum_{v=1}^{N_V}\sum_{n=1}^{M_V}\int\limits_{V_v} k_2(\mathbf{r})\mathbf{f}_n^V(\mathbf{r})\cdot\mathbf{E}_S^s(\mathbf{r})\;dV_v = \\
&j\omega\mu_0\sum_{u=1}^{N_V}\sum_{v=1}^{N_S}\sum_{m=1}^{M_V}\sum_{n=1}^{M_S} I_m\int\limits_{T_u}\int\limits_{V_v} k_2(\mathbf{r})\mathbf{f}_n^V(\mathbf{r})\cdot\mathbf{f}_m(\mathbf{r}')\;G(\mathbf{r},\mathbf{r}')\;dV_v dT_u \qquad (3.75)\\
&-\frac{1}{j\omega\epsilon_0}\sum_{u=1}^{N_V}\sum_{v=1}^{N_S}\sum_{m=1}^{M_V}\sum_{n=1}^{M_S} I_m\int\limits_{T_u}\int\limits_{S_v} k_2(\mathbf{r})\nabla'\cdot\mathbf{f}_m(\mathbf{r}')\;\mathbf{f}_n^V(\mathbf{r})\cdot\mathbf{u}_v\;G(\mathbf{r},\mathbf{r}')\;dS_v dT_u
\end{aligned}
$$

As with (3.74), the divergence theorem and standard vector identities have been used to simplify the integral of $k_2(\mathbf{r})\mathbf{f}_n^V(\mathbf{r})$ with the gradient term in (3.71).

3.4.4 Voltage Sources, Lumped Impedances and Conduction Losses

In an MRI RF coil system, voltages sources are used as the primary sources of excitation. As such, a voltage source instead of an incident wave needs to be incorporated into the MoM formulation. This can be accomplished by the introduction of an appropriate feed model into the system [42, 43]. One such model that is ideally suited for use with the RWG basis function is the so-called delta-gap source model [44, 45]. The delta-gap source model is an impressed voltage source connected across a gap of negligible thickness along an element of the structure as shown in Fig.3.9. The

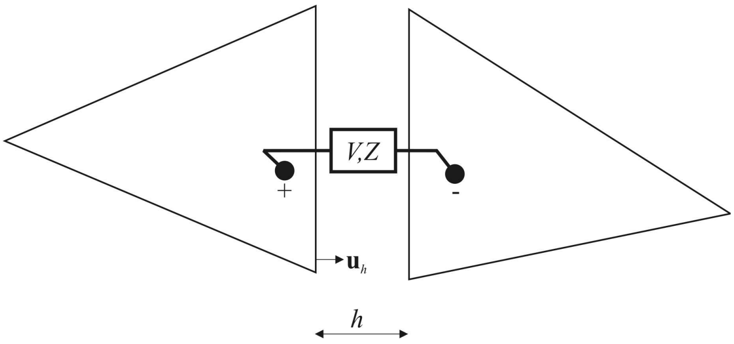

Figure 3.9: Delta-gap feed model showing a voltage source V connected across the gap h. The connected voltage can also be due to an attached impedance Z as shown.

impressed electric field **E** within the region of the gap can be expressed in terms of the impressed voltage V and the gap thickness h as

$$\mathbf{E} = -\nabla\Phi = -\frac{V}{h}\mathbf{u}_h \tag{3.76}$$

where Φ denotes the electric potential and $\mathbf{u}_h$ is the normal of the feed edge along the gap h. From (3.76), we observe that in the limit as h tends to zero, the electric field within the gap becomes infinite. By using an approximation to the delta-function construct [46], we can simplify (3.76) into the form

$$\begin{aligned} \mathbf{E} &= -V \underset{h\rightarrow 0}{Lt} \frac{1}{h}\ \mathbf{u}_h \\ &= -V\delta(h)\ \mathbf{u}_h \end{aligned} \tag{3.77}$$

Also, the delta function approximation used in (3.77) implies that the integral of the electric field in the region of the gap is ideally the negative of the applied voltage [25]. This can be stated more concisely in the form

$$\begin{aligned} \int \mathbf{E}\cdot\mathbf{u}_h\ dh &= -\int V\delta(h)\ \mathbf{u}_h\cdot\mathbf{u}_h\ dh \\ &= -\int V\delta(h)\ dh \\ &= -V \end{aligned} \tag{3.78}$$

Application of the delta-gap source model involves associating the model with the defining edge of an RWG element. This implies that the electric field $\mathbf{E}(\mathbf{r})$ on the surface of the element is normal to the surface except within the gap region where it is essentially tangential. As a consequence, the right-hand side of (3.57) and the left-hand side of (3.72) will be nonzero, and can be evaluated using (3.77) as

$$
\begin{aligned}
\int_{T_v} \mathbf{f}_n(\mathbf{r}) \cdot \mathbf{E}(\mathbf{r})\ dT_v &= -V_m \int_{T_v} \mathbf{f}_n(\mathbf{r}) \cdot \mathbf{u}_h\ \delta(h)\ dT_v \\
&= -V_m \int_{T_v} \delta(h)\ dh \\
&= -V_m
\end{aligned}
\tag{3.79}
$$

where V_m is the gap voltage applied across the m^{th} element. It should be noted that (3.79) will be nonzero only when $m = n$. With the introduction of lumped impedance sources, also shown in Fig.3.9, the lumped impedance Z is simply

$$
Z = \begin{cases} R \\ j\omega L \\ \dfrac{1}{j\omega C} \end{cases}
\tag{3.80}
$$

the gap voltage V_m in this case is essentially the voltage drop across the associated impedance of the m^{th} element [25]. Thus, we can conveniently express V_m in the form

$$
V_m = -I_m Z
\tag{3.81}
$$

where I_m is the unknown expansion coefficient representing the normal component of current density associated with the m^{th} element as defined in (3.26).

Finally, we consider the introduction of conduction losses in the surface formulation of (3.57) and (3.72). In this case, the coil surface must be considered a nonperfect conductor in order to account for resistive losses [25]. Obviously, this should result in nonzero values for the right-hand side of (3.57) and the left-hand side of (3.72) since there is a nonzero tangential component of the electric field on the surface of a nonperfect conductor. The tangential component of the electric field $\mathbf{E}_{\tan}(\mathbf{r})$ is related to the surface current density $\mathbf{J}(\mathbf{r})$ by

$$\mathbf{E}_{\tan}(\mathbf{r}) = \rho\ \mathbf{J}(\mathbf{r}) \tag{3.82}$$

where ρ is the surface resistivity of the nonperfect conducting surface. With the relationship defined in (3.82), we can evaluate the right-hand side of (3.57) and the left-hand side of (3.72) using

$$\begin{aligned}\sum_{v=1}^{N_S}\sum_{n=1}^{M_S}\int_{T_v}\mathbf{f}_n(\mathbf{r})\cdot\mathbf{E}(\mathbf{r})\ dT_v &= \sum_{v=1}^{N_S}\sum_{n=1}^{M_S}\int_{T_v}\mathbf{f}_n(\mathbf{r})\cdot\mathbf{E}_{\tan}(\mathbf{r})\ dT_v \\ &= \rho\sum_{v=1}^{N_S}\sum_{\substack{m=1\\n=1}}^{M_S} I_m\int_{T_v}\mathbf{f}_n(\mathbf{r})\cdot\mathbf{f}_m(\mathbf{r})\ dT_v\end{aligned} \tag{3.83}$$

Note that the integral in (3.83) is ideally zero when element m and n are not part of the same triangular element.

3.4.5 MoM RF Coil Model

In this section, we discuss the derivation of a complete MoM model of an MRI RF coil. Our goal is to provide a set of matrix equations that can be used to implement a numerical procedure for obtaining an accurate model of an MRI RF coil system. The complete matrix model takes into account conduction losses on the surface of the coil, voltage excitation at the transmitting ports, and the introduction of lumped impedances for tuning and matching the coil system at the resonance frequency.

We begin our development of a suitable coil model by considering the Surface-Volume MoM equations of (3.72) and (3.73). We intend to develop a matrix equation of the form

$$\boldsymbol{\mathcal{V}} = \boldsymbol{\mathcal{Z}}\boldsymbol{\mathcal{I}} \tag{3.84}$$

where $\boldsymbol{\mathcal{V}}$ is the field excitation vector, $\boldsymbol{\mathcal{Z}}$ is the impedance matrix, and $\boldsymbol{\mathcal{I}}$ is the vector of unknown current density distributions. The vectors $\boldsymbol{\mathcal{V}}$ and $\boldsymbol{\mathcal{I}}$ are of dimension $M_S + M_V$, while the matrix $\boldsymbol{\mathcal{Z}}$ is of dimension $(M_S + M_V) \times (M_S + M_V)$. As mentioned previously, M_S represents the total number of RWG elements in the surface discretization while M_V denotes the total number of solenoidal edge elements in the volume discretization. Next, we compartmentalize the matrix equation of (3.84) based on (3.72) and (3.73) in the form

$$\begin{pmatrix} V_S \\ V_V \end{pmatrix} = \begin{pmatrix} Z_{SS} & Z_{SV} \\ Z_{VS} & Z_{VV} \end{pmatrix} \begin{pmatrix} I \\ C \end{pmatrix} \tag{3.85}$$

The field excitation vector V_S denotes a series of delta-gap voltage sources applied on the surface of the structure. This is the chosen form of excitation most suitable for use with RWG elements, as discussed earlier. Thus, we can express V_S using (3.79) as

$$V_S = -\int\limits_{T_v} \mathbf{f}_n(\mathbf{r}) \cdot \mathbf{E}(\mathbf{r})\ dT_v = V_m \tag{3.86}$$

with $m = 1,\ 2,\ \ldots,\ M_S$. Similarly, the excitation vector V_V represents an electric field excitation on the inhomogeneous volume by an incident wave. In the absence of delta-gap voltage sources, i.e. when $V_S = 0$, V_V can be expressed as

$$V_V = \int\limits_{V_v} k_2(\mathbf{r})\mathbf{f}_n^V(\mathbf{r}) \cdot \mathbf{E}^i(\mathbf{r})\ dV_v \tag{3.87}$$

with $n = 1,\ 2,\ \ldots,\ M_S$, otherwise $V_V = 0$ for all n since our MoM model only allows one source of electromagnetic excitation. Next, we consider the Z_{SS} component of the impedance matrix $\boldsymbol{\mathcal{Z}}$ in (3.84). Clearly, Z_{SS} is a combination of (3.57), (3.83) and (3.81), and subsequently can be express as

$$\begin{aligned} Z_{SS} &= \frac{1}{j\omega\epsilon} \int\limits_{T_u}\int\limits_{T_v} \nabla\cdot\mathbf{f}_n(\mathbf{r})\nabla'\cdot\mathbf{f}_m(\mathbf{r}')G(\mathbf{r},\mathbf{r}')\ dT_u dT_v \\ &+ j\omega\mu \int\limits_{T_u}\int\limits_{T_v} \mathbf{f}_n(\mathbf{r})\cdot\mathbf{f}_m(\mathbf{r}')G(\mathbf{r},\mathbf{r}')\ dT_u dT_v \\ &+ \rho \int\limits_{T_v} \mathbf{f}_m(\mathbf{r})\cdot\mathbf{f}_m(\mathbf{r}')\ dT_v + Z_{mm} \\ &\qquad\qquad\qquad m,n \in 1,2,\ldots,M_S \end{aligned} \tag{3.88}$$

Similarly, the component Z_{VV} of $\boldsymbol{\mathcal{Z}}$ is essentially (3.67) without the incident field excitaion. This can be expressed in the form

$$\begin{aligned} Z_{VV} &= \int\limits_{V_v} k_1(\mathbf{r})k_2(\mathbf{r}')\mathbf{f}_m^V(\mathbf{r}')\cdot\mathbf{f}_n^V(\mathbf{r})\ dV_v \\ &+ j\omega\mu_0 \int\limits_{V_u}\int\limits_{V_v} k_2(\mathbf{r}')k_2(\mathbf{r})\mathbf{f}_m^V(\mathbf{r}')\cdot\mathbf{f}_n^V(\mathbf{r})\ G(\mathbf{r},\mathbf{r}')\ dV_u dV_v \\ &+ \frac{1}{j\omega\epsilon_0} \int\limits_{S_u}\int\limits_{S_v} k_2(\mathbf{r}')k_2(\mathbf{r})\mathbf{f}_m^V(\mathbf{r}')\cdot\mathbf{u}_u\ \mathbf{f}_n^V(\mathbf{r})\cdot\mathbf{u}_v\ G(\mathbf{r},\mathbf{r}')\ dS_u dS_v \\ &\qquad\qquad\qquad m,n \in 1,2,\ldots,M_V \end{aligned} \tag{3.89}$$

Finally, we consider the Z_{SV} and Z_{VS} components of the impedance matrix $\boldsymbol{\mathcal{Z}}$. These matrices describe the mutual interaction between the surface RWG elements and the volume solenoidal elements. This interaction is given by (3.74) and (3.75) as discussed previously. Careful observations of (3.74) and (3.75) reveal that they are equivalent, implying Z_{SV} and Z_{VS} are equivalent matrices. The implication of this is that the impedance matrix $\boldsymbol{\mathcal{Z}}$ is symmetric since Z_{SS} and Z_{VV} are also symmetric matrices.

We conclude by expressing the equivalent matrices Z_{SV} and Z_{VS} in the form

$$\begin{aligned}
Z_{SV} = j\omega\mu_0 \int\limits_{T_v}\int\limits_{V_u} & k_2(\mathbf{r}')\mathbf{f}_n(\mathbf{r}) \cdot \mathbf{f}_m^V(\mathbf{r}')\ G(\mathbf{r},\mathbf{r}')\ dV_u dT_v \\
- \frac{1}{j\omega\epsilon_0} \int\limits_{T_v}\int\limits_{S_u} & k_2(\mathbf{r}')\nabla \cdot \mathbf{f}_n(\mathbf{r})\ \mathbf{f}_m^V(\mathbf{r}') \cdot \mathbf{u}_u\ G(\mathbf{r},\mathbf{r}')\ dS_u dT_v \\
& m \in 1, 2, \ldots, M_V \\
& n \in 1, 2, \ldots, M_S
\end{aligned} \tag{3.90}$$

and

$$\begin{aligned}
Z_{VS} = j\omega\mu_0 \int\limits_{T_u}\int\limits_{V_v} & k_2(\mathbf{r})\mathbf{f}_n^V(\mathbf{r}) \cdot \mathbf{f}_m(\mathbf{r}')\ G(\mathbf{r},\mathbf{r}')\ dV_v dT_u \\
- \frac{1}{j\omega\epsilon_0} \int\limits_{T_u}\int\limits_{S_v} & k_2(\mathbf{r})\nabla' \cdot \mathbf{f}_m(\mathbf{r}')\ \mathbf{f}_n^V(\mathbf{r}) \cdot \mathbf{u}_v\ G(\mathbf{r},\mathbf{r}')\ dS_v dT_u \\
& m \in 1, 2, \ldots, M_S \\
& n \in 1, 2, \ldots, M_V
\end{aligned} \tag{3.91}$$

After all the elements of the excitation vector $\boldsymbol{\mathcal{V}}$ and the impedance matrix $\boldsymbol{\mathcal{Z}}$ have been determined, the resulting system of linear equations can be solved for the unknown I_m and C_m coefficients. Once all these coefficients are determined, the surface current density and equivalent volume current density can then be obtained. The scattered electric field due to the surface current density can be obtained by substituting (3.26) in (3.70), yielding

$$\begin{aligned}
\mathbf{E}_S^s(\mathbf{r}) = & \frac{1}{j\omega\epsilon} \sum_{u=1}^{N_S}\sum_{m=1}^{M_S} I_m \int\limits_{T_u} \nabla' \cdot \mathbf{f}_m(\mathbf{r}')\nabla G(\mathbf{r},\mathbf{r}')\ dT_u \\
& - j\omega\mu \sum_{u=1}^{N_S}\sum_{m=1}^{M_S} I_m \int\limits_{T_u} \mathbf{f}_m(\mathbf{r}')G(\mathbf{r},\mathbf{r}')\ dT_u
\end{aligned} \tag{3.92}$$

Also, the resulting scattered magnetic field $\mathbf{B}_S^s(\mathbf{r})$ is easily obtained by using (3.49) in (3.8) giving

$$\mathbf{B}_S^s(\mathbf{r}) = \mu \sum_{u=1}^{N_S} \sum_{m=1}^{M_S} I_m \int\limits_{T_u} \mathbf{f}_m(\mathbf{r}') \times \nabla' G(\mathbf{r}, \mathbf{r}') \; dT_u \tag{3.93}$$

Similarly, we can obtain the scattered electric field due to the equivalent volume current density from (3.71) as

$$\begin{aligned} \mathbf{E}_V^s(\mathbf{r}) = &-\frac{1}{j\omega\epsilon} \sum_{u=1}^{N_V} \sum_{m=1}^{M_V} C_m k_2(\mathbf{r}') \int\limits_{S_u} \mathbf{f}_m^V(\mathbf{r}') \cdot \mathbf{u}_u \; \nabla G(\mathbf{r}, \mathbf{r}') \; dS_u \\ &- j\omega\mu \sum_{u=1}^{N_V} \sum_{m=1}^{M_V} C_m k_2(\mathbf{r}') \int\limits_{V_u} \mathbf{f}_m^V(\mathbf{r}') G(\mathbf{r}, \mathbf{r}') \; dV_u \end{aligned} \tag{3.94}$$

The associated magnetic field can be expressed as

$$\begin{aligned} \mathbf{B}_V^s(\mathbf{r}) &= \mu \sum_{u=1}^{N_V} \sum_{m=1}^{M_V} C_m k_2(\mathbf{r}') \int\limits_{V_u} \mathbf{f}_m^V(\mathbf{r}') \times \nabla' G(\mathbf{r}, \mathbf{r}') \; dV_u \\ &= \mu \sum_{u=1}^{N_V} \sum_{m=1}^{M_V} C_m k_2(\mathbf{r}') \mathbf{f}_m^V(\mathbf{r}') \times \mathbf{u}_u \int\limits_{S_u} G(\mathbf{r}, \mathbf{r}') \; dS_u \end{aligned} \tag{3.95}$$

Because $\mathbf{f}_m^V(\mathbf{r}')$ is a constant vector field in each tetrahedron, standard vector identities dictate that

$$\int\limits_{V_u} \nabla' G(\mathbf{r}, \mathbf{r}') \; dV_u = \mathbf{u}_u \int\limits_{S_u} G(\mathbf{r}, \mathbf{r}') \; dS_u \tag{3.96}$$

The total electric field in the inhomogeneous volume can be found from (3.61) giving

$$\mathbf{E}(\mathbf{r}) = k_1(\mathbf{r}) \sum_{m=1}^{M_V} C_m \mathbf{f}_m^V(\mathbf{r}) \tag{3.97}$$

The total magnetic field in the inhomogeneous volume is given by the sum of (3.93) and (3.95), i.e.

$$\mathbf{B}(\mathbf{r}) = \mathbf{B}_S^s(\mathbf{r}) + \mathbf{B}_V^s(\mathbf{r}) \tag{3.98}$$

3.5 Method of Moments Integral Evaluation

The numerical evaluation of the MoM integrals forms an essential part in obtaining stable and accurate solutions of the underlying electromagnetic scattering problem. These integrals posses a singular behavior inherent in their kernels, but the very nature of the singular behavior makes evaluation of their integral kernels very involving due to the presence of the free space Green's function and its gradient. The inclusion of the free space Green's function and its gradient introduce singularities of order $1/R$ and $1/R^2$ as $R \to 0$, where $R = |\mathbf{r} - \mathbf{r}'|$ denotes the distance between the source and observation points. As such, traditional integration schemes based on Gaussian quadrature are ineffective and lead to inaccurate results. In order to alleviate this issue, several techniques have been developed specifically to improve accuracy, stability and efficiency of evaluation. These include the Duffy's transformation [47], polar coordinate transformation [48], integration by series expansion [49], and several singularity extraction methods [50]–[56].

In the Duffy's transformation method, the source region is subdivided into 3 smaller regions of similar geometry that share a common vertex located at the singularity [47]. The integral over each subregion is subsequently transformed into an integral over a higher order geometry. This effectively cancels out the inherent singularity in the low order domain. However, the accuracy of the transformation is dependent on the regularity of the source region. Also, the transformation exhibits increases in computational complexity with the addition of new integration points in the source domain. Lastly, the transformation cannot easily be applied to singularities of order $1/R^2$ [50].

In the series expansion technique, transcendental functions in the integral kernel are expanded as a series of polynomials. Each element of the series is integrated analytically thus eliminating the singular point [49]. This method is extremely accurate in the near field where the error rapidly converges to zero as $R \to 0$. But it suffers from the drawback that it cannot effectively handle a $1/R^2$ singularity [49]. This is also the case with the polar coordinate transformation.

The singularity extraction method seeks to regularize the integral kernel by extracting the singularity and integrating it analytically for the inner source integral for specific observation points. The regularized kernel is then integrated using more traditional numerical integration schemes. However, numerical integration of the regularized kernel may still lead to an inaccurate solution because the kernel may not necessarily be continuously differentiable in the source domain [50]. Continuous differentiability of the kernel in the source domain is a requirement for standard integration scheme such as the Gaussian quadrature [51]. Furthermore, kernels having singularity of order $1/R^2$ are difficult to integrate when the source and observation points lie on intersecting planes [51]. As such, several researchers have thoroughly investigated possible solutions to these issues [50] –[52] and [56]. They proposed a remedy where more terms are extracted from the integral kernel and integrated analytically over the source domain. After extraction, the remaining function is at least once continuously differentiable in the source domain when $R = 0$. Also, this solution easily handles kernels having a $1/R^2$ singularity in their source domains.

In this work, the above technique was employed to evaluate the singular integrals required for our MoM RF coil formulation. Our implementation extracts only 2 terms from the Green's function and its gradient. After extraction, the remaining function is sufficiently smooth and 1^{st} order continuously differentiable and thus allows for the application of the Gaussian quadrature [57].

3.5.1 Identification of Base Integrals

The evaluation of each element of (3.88), (3.89), (3.90) or (3.91), and (3.92), (3.93), (3.94) and (3.95) involves integrations over triangular and tetrahedral domains. The triangular domain describe the surfaces of the individual tetrahedra elements as well as the triangular regions of the surface discretization, while the tetrahedral domain describes the tetrahedra regions in the volume discretization. All integrations over these domains were accomplished using the Gaussian numerical quadrature method except in cases where a singularity exist in the integral kernels as a result of the presence of the Green's function or its gradient. In order to evaluate these singular integrals, we need to extract their singular terms as well as one more term that guarantees continuous differentiability, and then integrate these terms using analytical techniques. The remaining non-singular terms are sufficiently smooth to allow for the application of the Gaussian numerical quadrature. We begin the integral evaluation process by identifying all the singular integral kernels in (3.88), (3.89), (3.90) or (3.91), (3.92), (3.93), (3.94) and (3.95). These are listed as follows:

$$\mathcal{B}_1 = \int\limits_{T_u}\int\limits_{T_v} G(\mathbf{r},\mathbf{r}')\ dT_u dT_v \tag{3.99}$$

$$\mathcal{B}_2 = \int\limits_{T_u}\int\limits_{T_v} (\mathbf{r}-\mathbf{r}_i)\cdot(\mathbf{r}'-\mathbf{r}_j)\ G(\mathbf{r},\mathbf{r}')\ dT_u dT_v \tag{3.100}$$

$$\mathcal{B}_3 = \int\limits_{V_u}\int\limits_{V_v} G(\mathbf{r},\mathbf{r}')\ dV_u dV_v \tag{3.101}$$

$$\mathcal{B}_4 = \int\limits_{S_u}\int\limits_{S_v} G(\mathbf{r},\mathbf{r}')\ dS_u dS_v \tag{3.102}$$

$$\mathcal{B}_5 = \int\limits_{T_v}\int\limits_{V_u} (\mathbf{r}-\mathbf{r}_i)\ G(\mathbf{r},\mathbf{r}')\ dV_u dT_v \tag{3.103}$$

$$\mathcal{B}_6 = \int\limits_{T_u} \nabla G(\mathbf{r},\mathbf{r}')\ dT_u \tag{3.104}$$

$$\mathcal{B}_7 = \int\limits_{T_u} (\mathbf{r}'-\mathbf{r}_i)\ G(\mathbf{r},\mathbf{r}')\ dT_u \tag{3.105}$$

$$\mathcal{B}_8 = \int\limits_{T_u} (\mathbf{r}'-\mathbf{r}_i)\times\nabla' G(\mathbf{r},\mathbf{r}')\ dT_u \tag{3.106}$$

$$\mathcal{B}_9 = \int\limits_{S_u} \nabla G(\mathbf{r}, \mathbf{r}') \; dS_u \tag{3.107}$$

$$\mathcal{B}_{10} = \int\limits_{V_u} G(\mathbf{r}, \mathbf{r}') \; dV_u \tag{3.108}$$

$$\mathcal{B}_{11} = \int\limits_{S_u} G(\mathbf{r}, \mathbf{r}') \; dS_u \tag{3.109}$$

For the case of the double integrals in (3.99)-(3.103), the outer integrals can be evaluated using numerical Gaussian quadrature [57]. On the other hand, their inner integrals as well as the single integrals of (3.104)-(3.109) contain a singularity that must be extracted and integrated analytically. The singularity can be extracted by expressing the Green's function $G(\mathbf{r}, \mathbf{r}')$ in terms of a singular component $G_A(\mathbf{r}, \mathbf{r}')$ and a nonsingular component $G_N(\mathbf{r}, \mathbf{r}')$. This is given as

$$\begin{aligned} G(\mathbf{r}, \mathbf{r}') &= \left(G(\mathbf{r}, \mathbf{r}') - \frac{1}{4\pi R} + \frac{k^2 R}{8\pi} \right) + \frac{1}{4\pi R} - \frac{k^2 R}{8\pi} \\ &= G_N(\mathbf{r}, \mathbf{r}') + G_A(\mathbf{r}, \mathbf{r}') \end{aligned} \tag{3.110}$$

where $R = |\mathbf{r} - \mathbf{r}'|$ and $G(\mathbf{r}, \mathbf{r}')$ is as defined in (3.20). The gradient of the Green's function can be written using (3.110) as

$$\begin{aligned} \nabla G(\mathbf{r}, \mathbf{r}') &= \nabla G_N(\mathbf{r}, \mathbf{r}') + \nabla G_A(\mathbf{r}, \mathbf{r}') \\ &= \nabla \left(G(\mathbf{r}, \mathbf{r}') - \frac{1}{4\pi R} + \frac{k^2 R}{8\pi} \right) + \frac{1}{4\pi} \nabla \frac{1}{R} - \frac{k^2}{8\pi} \nabla R \end{aligned} \tag{3.111}$$

The nonsingular term $G_N(\mathbf{r}, \mathbf{r}')$ and its gradient $\nabla G_N(\mathbf{r}, \mathbf{r}')$ have been shown to be sufficiently smooth with continuous derivates at $R = 0$ [50]. Thus, evaluation of source and testing integrals with these kernels can be done more readily using Gaussian quadrature with accurate results.

Next, we proceed to identify the base integrals. With careful expansion and simplification of (3.99)-(3.103), the following base integrals were identified. These are listed as

$$\mathcal{I}_1 = \int\limits_S R^n \, dS' \tag{3.112}$$

$$\mathcal{I}_2 = \int\limits_S \mathbf{r}' R^n \, dS' \tag{3.113}$$

$$\mathcal{I}_3 = \int\limits_S \nabla R^n \, dS' \tag{3.114}$$

$$\mathcal{I}_4 = \int\limits_V R^n \, dV' \tag{3.115}$$

$$\mathcal{I}_5 = \int\limits_V \nabla R^n \, dV' \qquad n \in -1, 1 \tag{3.116}$$

where the integration with limits S and V denote integration over triangular and tetrahedra domains, respectively. The evaluation of the singular base integrals of (3.112)-(3.116) is accomplished by using Gauss integral theorem to transform the integral over the appropriate domain S or V into an integral over the boundaries ∂S or ∂V of the domain. The application of the Gauss integral theorem requires that the integrand be continuously differentiable in the integration domain [53]. However, this is not the case due to the presence of the singularity in the domain where $R = |\mathbf{r} - \mathbf{r}'| = 0$. Our approach to this problem is to isolate a small region of the integration domain containing the singularity for separate treatment as described in [53]. Integrals over this region or its boundary can be evaluated by using a local polar coordinate scheme centered at the singularity.

3.5.1.1 Base Integrals on a Triangle

In the evaluation of (3.112) over the triangular domain S for $n = -1$, we partition S into two regions defined as $S - S_\varepsilon$ and S_ε, respectively. This partitioning is as shown in Fig.3.10 where the domain S is defined by triangle ABC, and the domain S_ε is a circle of radius ε centered at point P' on S. The point P is the observation point as

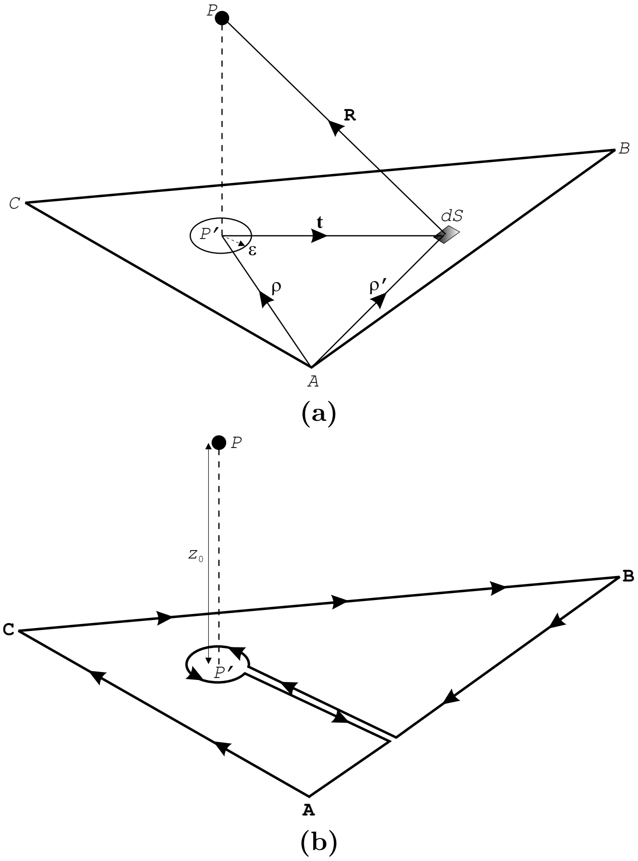

Figure 3.10: Transforming an integral over a surface S into an integral over the boundary ∂S of the surface S; (a) surface integral with singular point extracted, (b) line integral without singularity.

defined by position vector $\mathbf{r}$, vector $\boldsymbol{\rho}$ is the projection of vector $\mathbf{r}$ onto S as referenced from point A, vector $\boldsymbol{\rho}'$ is a similar projection of vector $\mathbf{r}'$ on S, vector $\mathbf{t}$ denotes the vector from point P' on S to the area element dS, and z_0 is the perpendicular distance between point P and the plane of S. Note that the planar configuration must be such that z_0 is in the direction of the normal of plane S. Now we can express (3.112) for $n = -1$ as

$$\begin{aligned}\int_S \frac{1}{R}\, dS' &= \underset{\varepsilon\to 0}{Lt} \int_{S-S_\varepsilon} \frac{1}{R}\, dS' + \underset{\varepsilon\to 0}{Lt} \int_{S_\varepsilon} \frac{1}{R}\, dS' \\ &= \underset{\varepsilon\to 0}{Lt} \int_{S-S_\varepsilon} \frac{1}{R}\, dS' \qquad (3.117)\end{aligned}$$

since the integral in the region S_ε evaluates as

$$\underset{\varepsilon\to 0}{Lt}\int_{S_\varepsilon}\frac{1}{R}\,dS' = \underset{\varepsilon\to 0}{Lt}\int_0^{2\pi}\int_0^{\varepsilon}\frac{t}{\sqrt{t^2+z_0^2}}\,dtd\theta = 0 \tag{3.118}$$

After the singularity has been extracted, we can then express (3.117) in a form that is suitable for the application of the Gauss integral theorem. This will allow us to transform the surface integral in (3.117) into a line integral that bounds the surface. By using the identity [53]

$$\frac{1}{R} = -\frac{z_0^2}{R^3} - \nabla'_S\cdot\frac{\mathbf{R}}{R} \tag{3.119}$$

$$\frac{1}{R^3} = -\nabla'_S\cdot\frac{\mathbf{t}}{t^2R} \tag{3.120}$$

we can further express (3.117) in the form

$$\begin{aligned}\int_S\frac{1}{R}\,dS' &= \underset{\varepsilon\to 0}{Lt}\int_{S-S_\varepsilon}\nabla'_S\cdot\left(\frac{z_0^2\mathbf{t}}{t^2R}-\frac{\mathbf{R}}{R}\right)dS'\\ &= \underset{\varepsilon\to 0}{Lt}\sum_{i=1}^{3}\int_{\partial S_i-\partial S_{i\varepsilon}}\left(\frac{z_0^2\mathbf{t}\cdot\mathbf{u}_i}{t^2R}-\frac{\mathbf{R}\cdot\mathbf{u}_i}{R}\right)dl'_i\end{aligned} \tag{3.121}$$

where $\mathbf{u}_i$ is the unit outward normal of edge ∂S_i with $i = 1, 2, 3$, and the summation is made across the edges ∂S_i and the infinitesimal arcs $\partial S_{i\varepsilon}$ that bound the domain $S-S_\varepsilon$ as defined in Fig.3.10. Next we seek to simplify (3.121) further by using Fig.3.11. The parameters associated with the evaluation of the line integral about the edge AB is as shown in Fig.3.11. These parameters can easily be extended to accommodate the evaluation of the line integral about the remaining edges. From Fig.3.10, we designate the perpendicular distance between the point P' and the edge AB or its extension OB by d_0. Also, the distance OA and OB that define the endpoints of edge AB are designated by l_1 and l_2 while R_1 and R_2 designate the distance of the endpoints of edge AB from the observation point P. We also define the angle φ_1 and φ_2 as

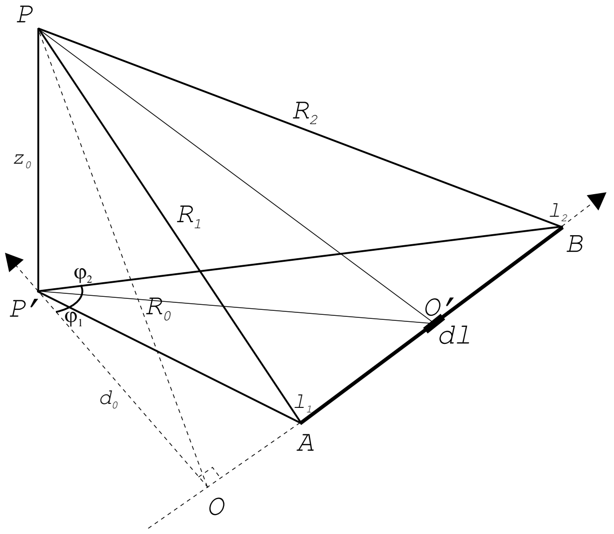

Figure 3.11: Geometrical quantities used in evaluating the line integral along an edge.

the angle subtended by the line OA and OB at the point P'. These angles define the infinitesimal arc $\partial S_{i\varepsilon}$ that bound the exclusion region. Also, the perpendicular distance between point P and the edge AB or its extension OB is designated by R_0. In addition, the source element dl is located at point O' and its distance from point P' is designated by l. Using Fig.3.11, we define the following additional parameters associated with edge AB

$$O'P = R = \sqrt{R_0^2 + l^2} \tag{3.122}$$

$$O'P' = t = \sqrt{d_0 + l^2} \tag{3.123}$$

which then allows us to simplify (3.121) in the form

$$\begin{aligned}\int_S \frac{1}{R}\, dS' = \sum_{i=1}^{3} \Bigg\{ & \int_{l_{1i}}^{l_{2i}} \frac{z_0^2 d_{0i}}{(d_{0i}^2 + l^2)\sqrt{R_0^2 + l^2}}\, dl' \\ & + \int_{l_{1i}}^{l_{2i}} \frac{d_{0i}}{\sqrt{R_0^2 + l^2}}\, dl' - \underset{\varepsilon \to 0}{Lt} \int_{\varphi_{i1}}^{\varphi_{i2}} \frac{z_0^2 - \varepsilon^2}{\sqrt{\varepsilon^2 + z_0^2}}\, d\varphi' \Bigg\}\end{aligned}$$

$$\begin{aligned}\int\limits_S \frac{1}{R}\, dS' &= \sum_{i=1}^{3}\left\{ z_0\left[\tan^{-1}\frac{l_{2i}z_0}{d_{0i}R_{2i}} - \tan^{-1}\frac{l_{1i}z_0}{d_{0i}R_{1i}}\right]\right.\\ &\qquad\left. + d_{0i}\ln\frac{l_{2i}+R_{2i}}{l_{1i}+R_{1i}} - z_0\left[\tan^{-1}\frac{l_{2i}}{d_{0i}} - \tan^{-1}\frac{l_{1i}}{d_{0i}}\right]\right\}\\ &= \sum_{i=1}^{3}\left\{ d_{0i}\ln\frac{l_{2i}+R_{2i}}{l_{1i}+R_{1i}} - z_0\left[\tan^{-1}\frac{l_{2i}d_{0i}}{R_{0i}^2+z_0R_{2i}} - \tan^{-1}\frac{l_{1i}d_{0i}}{R_{0i}^2+z_0R_{1i}}\right]\right\}\end{aligned} \tag{3.124}$$

where we have employed the identity

$$\tan^{-1}\frac{l_{ni}}{d_{0i}} - \tan^{-1}\frac{l_{ni}z_0}{d_{0i}R_{ni}} = \tan^{-1}\frac{l_{ni}d_{0i}}{R_{0i}^2+z_0R_{ni}} \tag{3.125}$$

with the assumption that the arctangent function was evaluated on its principal axis, and $n = 1, 2$ define the index associated with the edge endpoints.

Similarly, we consider the evaluation of (3.112) over the triangular region S for $n = 1$. In this case, we do not need to partition the S domain since the kernel is non-singular for all R. Instead, we employ the identity [52]

$$\nabla'_S \cdot (R^n\mathbf{R}) = nz_0^2R^{n-2} - (n+2)R^n \tag{3.126}$$

in (3.112) for $n = 1$ and thus evaluate the integral as

$$\begin{aligned}\int\limits_S R\, dS' &= \frac{z_0^2}{3}\int\limits_S \frac{1}{R}\, dS' - \frac{1}{3}\int\limits_S \nabla'_S\cdot(R\mathbf{R})\, dS'\\ &= \frac{z_0^2}{3}\int\limits_S \frac{1}{R}\, dS' - \frac{1}{3}\sum_{i=1}^{3}\int\limits_{\partial S_i} R\mathbf{R}\cdot\mathbf{u}_i\, dl'\\ &= \frac{z_0^2}{3}\int\limits_S \frac{1}{R}\, dS' + \frac{1}{3}\sum_{i=1}^{3}\int\limits_{\partial S_i} d_{0i}\sqrt{R_0^2+l^2}\, dl'\end{aligned}$$

$$
\begin{aligned}
\int\limits_S R\; dS' &= \frac{z_0^2}{3}\int\limits_S \frac{1}{R}\; dS' + \frac{d_{0i}}{6}\sum_{i=1}^{3}\left\{(l_{2i}R_{2i} - l_{1i}R_{1i}) + R_{0i}^2 \ln\frac{l_{2i}+R_{2i}}{l_{1i}+R_{1i}}\right\} \\
&= \frac{z_0^2}{3}\sum_{i=1}^{3}\left\{d_{0i}\ln\frac{l_{2i}+R_{2i}}{l_{1i}+R_{1i}} - z_0\left[\tan^{-1}\frac{l_{2i}d_{0i}}{R_{0i}^2+z_0R_{2i}} - \tan^{-1}\frac{l_{1i}d_{0i}}{R_{0i}^2+z_0R_{1i}}\right]\right\} \\
&+ \frac{d_{0i}}{6}\sum_{i=1}^{3}\left\{(l_{2i}R_{2i} - l_{1i}R_{1i}) + R_{0i}^2\ln\frac{l_{2i}+R_{2i}}{l_{1i}+R_{1i}}\right\} \qquad (3.127)
\end{aligned}
$$

For the evaluation of (3.113) for the case of $n = -1$, we proceed as with (3.112) and partition S into two regions defined by $S - S_\varepsilon$ and S_ε as shown in Fig.3.10. As mentioned previously, the domain S is defined by triangle ABC while the S_ε domain is a circle of radius ε centered at point P' on S. Also, we define the relationship

$$
\nabla_s' R^{n+2} = (n+2)R^n(\mathbf{r}' - \mathbf{r}_\rho) \qquad (3.128)
$$

where $\mathbf{r}_\rho$ is the projection of the observation point located by $\mathbf{r}$ on the plane of S. This relationship is essential in transforming the surface integral over S into a line integral along ∂S using Gauss integral theorem. Now we can express (3.113) for $n = -1$ in the form

$$
\int\limits_S \frac{\mathbf{r}'}{R}\; dS' = \int\limits_S \frac{\mathbf{r}' - \mathbf{r}_\rho}{R}\; dS' + \mathbf{r}_\rho \int\limits_S \frac{\mathbf{1}}{R}\; dS' \qquad (3.129)
$$

Here, the second term on the right can easily be evaluated as $\mathbf{r}_\rho$ multiplied by (3.124). The first term on the right can easily be evaluated using the relationship in (3.128) for $n = -1$ as

$$
\begin{aligned}
\int\limits_S \frac{\mathbf{r}' - \mathbf{r}_\rho}{R}\; dS' &= \underset{\varepsilon\to 0}{Lt}\int\limits_{S-S_\varepsilon} \frac{\mathbf{r}' - \mathbf{r}_\rho}{R}\; dS' + \underset{\varepsilon\to 0}{Lt}\int\limits_{S_\varepsilon} \frac{\mathbf{r}' - \mathbf{r}_\rho}{R}\; dS' \\
&= \underset{\varepsilon\to 0}{Lt}\int\limits_{S-S_\varepsilon} \nabla_S' R\; dS' \\
&= \underset{\varepsilon\to 0}{Lt}\sum_{i=1}^{3}\int\limits_{\partial S_i - \partial S_{i\varepsilon}} R\mathbf{u}_i\; dl'
\end{aligned}
$$

$$\begin{aligned}\int\limits_S \frac{\mathbf{r}'-\mathbf{r}_\rho}{R}\ dS' &= \sum_{i=1}^{3}\mathbf{u}_i \int\limits_{\partial S_i} R\ dl' \\ &= \frac{1}{2}\sum_{i=1}^{3}\mathbf{u}_i\left\{\int_{l_{1i}}^{l_{2i}} \frac{d}{dl'}\big(Rl\big)\ dl' + R_{0i}^2\int_{l_{1i}}^{l_{2i}}\frac{1}{R}\ dl'\right\} \\ &= \frac{1}{2}\sum_{i=1}^{3}\mathbf{u}_i\left\{l_{2i}R_{2i}-l_{1i}R_{1i}+R_{0i}^2\ln\frac{l_{2i}+R_{2i}}{l_{1i}+R_{1i}}\right\} \qquad (3.130)\end{aligned}$$

When $n=1$ in (3.113), we have

$$\int\limits_S \mathbf{r}'R\ dS' = \int\limits_S (\mathbf{r}'-\mathbf{r}_\rho)R\ dS' + \mathbf{r}_\rho\int\limits_S R\ dS' \qquad (3.131)$$

Also, the second term on the right is just $\mathbf{r}_\rho$ multiplied by (3.127). On the other hand, the first term is calculated using (3.128) for $n=1$ as

$$\begin{aligned}\int\limits_S (\mathbf{r}'-\mathbf{r}_\rho)R\ dS' &= \frac{1}{3}\int\limits_S \nabla_S' R^3\ dS' \\ &= \frac{1}{3}\sum_{i=1}^{3}\mathbf{u}_i\int\limits_{\partial S_i} R^3\ dl' \\ &= \frac{1}{12}\sum_{i=1}^{3}\mathbf{u}_i\left\{\int_{l_{1i}}^{l_{2i}}\frac{d}{dl'}\big(R^3 l\big)\ dl' + 3R_{0i}^2\int_{l_{1i}}^{l_{2i}} R\ dl'\right\} \\ &= \frac{1}{12}\sum_{i=1}^{3}\mathbf{u}_i\left\{l_{2i}R_{2i}^3 - l_{1i}R_{1i}^3\right. \\ &\qquad\left. + \frac{3R_{0i}^2}{2}\big(l_{2i}R_{2i}-l_{1i}R_{1i}+R_{0i}^2\ln\frac{l_{2i}+R_{2i}}{l_{1i}+R_{1i}}\big)\right\} \qquad (3.132)\end{aligned}$$

Let us now consider the evaluation of (3.114) when $n=-1$ and $n=1$. We begin by stating the following results:

$$\begin{aligned}\nabla\frac{1}{R} &= \nabla_S\frac{1}{R} + \mathbf{z}\frac{\partial}{\partial z}\frac{1}{R} \\ &= -\nabla_S'\frac{1}{R} - \mathbf{z}\frac{z_0}{R^3} \qquad (3.133)\end{aligned}$$

and

$$\begin{aligned}\nabla R &= \nabla_S R + \mathbf{z}\frac{\partial}{\partial z}R \\ &= -\nabla'_S R + \mathbf{z}\frac{z_0}{R}\end{aligned} \tag{3.134}$$

where $\mathbf{z}$ is the unit normal on the plane of triangle S. These results will enable us transform (3.114) into a form that is suitable for the application of the Gauss integral theorem. Considering (3.134), we can write (3.114) for $n = 1$ in the form

$$\int_S \nabla R \; dS' = -\int_S \nabla'_S R \; dS' + \mathbf{z}\int_S \frac{z_0}{R}\; dS' \tag{3.135}$$

Both terms on the right of (3.135) have previously been evaluated in (3.130) and (3.124). Thus, (3.135) simplifies as

$$\begin{aligned}\int_S \nabla R \; dS' = \mathbf{z}\sum_{i=1}^{3}\left\{ d_{0i}z_0 \ln\frac{l_{2i}+R_{2i}}{l_{1i}+R_{1i}} - z_0^2\left[\tan^{-1}\frac{l_{2i}d_{0i}}{R_{0i}^2+z_0R_{2i}} - \tan^{-1}\frac{l_{1i}d_{0i}}{R_{0i}^2+z_0R_{1i}}\right]\right\} \\ -\frac{1}{2}\sum_{i=1}^{3}\mathbf{u}_i\left\{ l_{2i}R_{2i} - l_{1i}R_{1i} + R_{0i}^2\ln\frac{l_{2i}+R_{2i}}{l_{1i}+R_{1i}}\right\}\end{aligned} \tag{3.136}$$

Similarly, when $n = -1$ we can use (3.133) to express (3.114) in the form

$$\int_S \nabla\frac{1}{R}\; dS' = -\int_S \nabla'_S\frac{1}{R}\; dS' - \mathbf{z}\int_S \frac{z_0}{R^3}\; dS' \tag{3.137}$$

We next apply the Gauss integral theorem to the first term on the right of (3.137) in order to transform the surface integral on S into a line integral around ∂S. This eventually leads to

$$\begin{aligned}\int\limits_{S} \nabla'_S \frac{1}{R}\, dS' &= \sum_{i=1}^{3} \mathbf{u}_i \int\limits_{\partial S_i} \frac{1}{R}\, dl' \\ &= \sum_{i=1}^{3} \mathbf{u}_i \ln \frac{l_{2i} + R_{2i}}{l_{1i} + R_{1i}} \end{aligned} \tag{3.138}$$

The second term on the right of (3.137) can be transformed into a suitable form using (3.120). As described previously, the presence of the singularity at $R = 0$ should be excluded from the domain S and integrated separately. The exclusion of the singular point at $R = 0$ will result in the partitioning of S into S_ε and $S - S_\varepsilon$. Thus, the second term on the right of (3.137) can be simplified as

$$\begin{aligned}\mathbf{z} \int\limits_{S} \frac{z_0}{R^3}\, dS' &= \mathbf{z} \underset{\varepsilon \to 0}{Lt} \left\{ \int\limits_{S_\varepsilon} \frac{z_0}{R^3}\, dS' - \int\limits_{S - S_\varepsilon} \nabla'_S \cdot \frac{z_0 \mathbf{t}}{t^2 R}\, dS' \right\} \\ &= \mathbf{z} \sum_{i=1}^{3} \left\{ \underset{\varepsilon \to 0}{Lt} \int\limits_{S_\varepsilon} \frac{z_0}{R^3}\, dS' - \int\limits_{\partial S - \partial S_\varepsilon} \frac{z_0 \mathbf{t} \cdot \mathbf{u}_i}{t^2 R}\, dS' \right\} \\ &= \mathbf{z} \sum_{i=1}^{3} \left\{ \underset{\varepsilon \to 0}{Lt} \int_{\varphi_{i1}}^{\varphi_{i2}} \frac{z_0}{\sqrt{\varepsilon^2 + z_0^2}}\, d\varphi' - \int_{l_{1i}}^{l_{2i}} \frac{z_0 d_{0i}}{(d_{0i}^2 + l^2)\sqrt{R_0^2 + l^2}}\, dl' \right\} \\ &= \mathbf{z} \sum_{i=1}^{3} \left\{ \tan^{-1} \frac{l_{2i} d_{0i}}{R_{0i}^2 + z_0 R_{2i}} - \tan^{-1} \frac{l_{1i} d_{0i}}{R_{0i}^2 + z_0 R_{1i}} \right\} \end{aligned} \tag{3.139}$$

3.5.1.2 Base Integrals on a Tetrahedron

In this section, we will consider the evaluation of (3.115) and (3.116) over the tetrahedral domain V. We will employ the use of the relationship

$$\nabla' \cdot R^n \mathbf{R} = -(n + 3) R^n \tag{3.140}$$

in order to easily apply the Gauss divergence theorem to (3.115). In a similar fashion when $n = -1$, as in the case of a triangular domain, we need to exclude a small neighborhood V_ε in the vicinity of the singularity and consider this integral for separate treatment. In essence, integrals over this region or its boundary will be evaluated using a local polar coordinate scheme centered at the singularity in the limit as the excluded region tends to zero. Now consider the integral in (3.115) when $n = -1$. With the help of (3.140), (3.115) can be evaluated as

$$\begin{aligned}\int\limits_V \frac{1}{R}\, dV' &= -\frac{1}{2} \underset{\varepsilon\to 0}{Lt} \int\limits_{V-V_\varepsilon} \nabla' \cdot \frac{\mathbf{R}}{R}\, dV' + \underset{\varepsilon\to 0}{Lt} \int\limits_{V_\varepsilon} \frac{1}{R}\, dV' \\ &= -\frac{1}{2} \underset{\varepsilon\to 0}{Lt} \int\limits_{\partial V-\partial V_\varepsilon} \frac{\mathbf{R}\cdot\mathbf{n}}{R}\, dS' \\ &= -\frac{1}{2}\sum_{j=1}^{4} \int\limits_{\partial V_j} \frac{\mathbf{R}\cdot\mathbf{n}_j}{R}\, dS' \\ &= \frac{1}{2}\sum_{j=1}^{4} z_{0j} \int\limits_{\partial V_j} \frac{1}{R}\, dS' \end{aligned} \tag{3.141}$$

using results from (3.124), (3.141) finally evaluates into

$$\begin{aligned}\int\limits_V \frac{1}{R}\, dV' = \frac{1}{2}\sum_{j,i=1}^{4,3} \Bigg\{ & z_{0j} d_{0ij} \ln \frac{l_{2ij} + R_{2ij}}{l_{1ij} + R_{1ij}} - z_{0j}^2 \Bigg[\tan^{-1} \frac{l_{2ij} d_{0ij}}{R_{0ij}^2 + z_{0j} R_{2ij}} \\ & - \tan^{-1} \frac{l_{1ij} d_{0ij}}{R_{0ij}^2 + z_{0j} R_{1ij}} \Bigg] \Bigg\} \end{aligned} \tag{3.142}$$

When $n = 1$ in (3.115), we have

$$\begin{aligned}\int\limits_V R\, dV' &= -\frac{1}{4} \int\limits_V \nabla' \cdot R\mathbf{R}\, dV' = -\frac{1}{4} \int\limits_{\partial V} R\mathbf{R}\cdot\mathbf{n}\, dS' \\ &= -\frac{1}{4}\sum_{j=1}^{4} \int\limits_{\partial V_j} R\mathbf{R}\cdot\mathbf{n}_j\, dS' = \frac{1}{4}\sum_{j=1}^{4} z_{0j} \int\limits_{\partial V_j} R\, dS' \end{aligned} \tag{3.143}$$

Using (3.127) in (3.143) gives

$$\int\limits_V R\, dV' = \frac{z_{0j}^3}{12} \sum_{j,i=1}^{4,3} \left\{ d_{0ij} \ln \frac{l_{2ij} + R_{2ij}}{l_{1ij} + R_{1ij}} \right.$$
$$\left. - z_{0j} \left[\tan^{-1} \frac{l_{2ij} d_{0ij}}{R_{0ij}^2 + z_{0j} R_{2ij}} - \tan^{-1} \frac{l_{1ij} d_{0ij}}{R_{0ij}^2 + z_{0j} R_{1ij}} \right] \right\}$$
$$+ \frac{z_{0j} d_{0ij}}{24} \sum_{j,i=1}^{4,3} \left\{ (l_{2ij} R_{2ij} - l_{1ij} R_{1ij}) + R_{0ij}^2 \ln \frac{l_{2ij} + R_{2ij}}{l_{1ij} + R_{1ij}} \right\} \tag{3.144}$$

Consider next the evaluation of (3.116) for $n = -1$. As discussed previously, we will partition the domain V around the singular point for separate treatment. In effect, we can evaluate (3.116) for $n = -1$ as

$$\int\limits_V \nabla \frac{1}{R}\, dV' = -\underset{\varepsilon \to 0}{Lt} \int\limits_{V - V_\varepsilon} \nabla' \frac{1}{R}\, dV' + \underset{\varepsilon \to 0}{Lt} \int\limits_{V_\varepsilon} \frac{\mathbf{R}}{R^3}\, dV'$$
$$= -\underset{\varepsilon \to 0}{Lt} \int\limits_{\partial V - \partial V_\varepsilon} \frac{\mathbf{n}}{R}\, dS'$$
$$= -\sum_{j=1}^{4} \mathbf{n}_j \int\limits_{\partial V_j} \frac{1}{R}\, dS'$$
$$= -\sum_{j,i=1}^{4,3} \mathbf{n}_j \left\{ d_{0ij} \ln \frac{l_{2ij} + R_{2ij}}{l_{1ij} + R_{1ij}} - z_{0j} \left[\tan^{-1} \frac{l_{2ij} d_{0ij}}{R_{0ij}^2 + z_{0j} R_{2ij}} \right. \right.$$
$$\left. \left. - \tan^{-1} \frac{l_{1ij} d_{0ij}}{R_{0ij}^2 + z_{0j} R_{1ij}} \right] \right\} \tag{3.145}$$

Also when $n = 1$, (3.116) simplifies into

$$\begin{aligned}
\int\limits_V \nabla R \, dV' &= -\int\limits_V \nabla' R \, dV' \\
&= -\int\limits_{\partial V} R\mathbf{n} \, dS' \\
&= -\sum_{j=1}^{4} \mathbf{n}_j \int\limits_{\partial V_j} R \, dS' \\
&= -\mathbf{n_j} \frac{z_{0j}^2}{12} \sum_{j,i=1}^{4,3} \Bigg\{ d_{0ij} \ln \frac{l_{2ij} + R_{2ij}}{l_{1ij} + R_{1ij}} \\
&\qquad\qquad - z_{0j} \left[\tan^{-1} \frac{l_{2ij} d_{0ij}}{R_{0ij}^2 + z_{0j} R_{2ij}} - \tan^{-1} \frac{l_{1ij} d_{0ij}}{R_{0ij}^2 + z_{0j} R_{1ij}} \right] \Bigg\} \\
&\quad - \mathbf{n_j} \frac{d_{0ij}}{6} \sum_{j,i=1}^{4,3} \Bigg\{ (l_{2ij} R_{2ij} - l_{1ij} R_{1ij}) + R_{0ij}^2 \ln \frac{l_{2ij} + R_{2ij}}{l_{1ij} + R_{1ij}} \Bigg\}
\end{aligned} \tag{3.146}$$

Efficient numerical calculation of these base integrals form the bulk of the evaluation of the impedance matrix. In deriving the impedance matrix, the associated integrals have been written in a form that emphasizes evaluation on a geometric basis rather than an element by element basis. This is because some elements require the same integrals when they share the same geometric domain. As such, it is far more efficient to calculate these integrals by geometric domain combinations. Furthermore, we have adopted the same numerical treatment proposed by [50] where two terms from the Green's function are extracted and integrated analytically by formulae developed above. These formulae are essentially identical to those presented in [50] and [52], except for (3.145) and (3.146) which were developed exclusively in this work. In conclusion, our numeric implementation has been shown to demonstrate faster convergence, superior accuracy and robustness, as well as improved computation time due to additional regularization by the extraction of higher-order terms [50] and [51].

3.6 Resolution of Discretization

An important issue concerning the application of any numerical procedure in a discretization domain is in the selection of an appropriate upper bound on the resolution of the discretization. Establishing such a bound on the resolution of the discretized elements minimizes discretization errors, improves stability, and enhances the accuracy of the numerical results [58]. A simple rule that can be applied to set up an upper bound on the discretized resolution is the Nyquist criterion. The Nyquist criterion sets up a lower bound on the sampling frequency f_s in the form

$$f_s = 2f \tag{3.147}$$

where f is the frequency of interest. Using (3.147), we can now set up an upper bound on the resolution as

$$l_{res} \leq \frac{\lambda}{2\sqrt{\epsilon_r}} \tag{3.148}$$

where l_{res} defines the required upper bound, and the product of frequency f and wavelength λ is a constant. From (3.148), we observe that an increase in frequency reduces the upper bound, thereby necessitating an increase in the number of elements in the discretization. Similarly, a decrease in frequency increases the upper bound consequently reducing the number of elements in the discretization. A more strict upper bound as discussed in [28, 58], where

$$l_{res} \leq \frac{\lambda}{4\sqrt{\epsilon_r}} \tag{3.149}$$

was adopted for our numerical implementation. The effects of biological tissues on this upper bound at a defined frequency is dependent on the electrical permittivity of the tissues as given in 3.149. Because of the availability of large computer memory resources, we targeted discretization resolutions that are less than 4mm.

Chapter 4

Model Implementation and Validation

In this chapter, we will discuss the implementation and validation of our Method of Moments Model for MRI RF coils. The model is the a numerical implementation of the MoM formulations derived in Chapter 3. Our goal is to use the full wave solutions obtained by the Method of Moments in the determination of the electrical and magnetic properties of RF coils prior to prototype construction. Knowledge of the electromagnetic properties of the RF coils can subsequently be used to influence their design for improved and optimum performance.

4.1 Software Implementation

The development of efficient software implementations for the numerical solutions of MoM based integral equations is of paramount importance in the design and development of appropriate electromagnetic models. Several critical factors come together to influence the software development process, but the key performance metric is the software execution time [59, 60]. For a given hardware configuration, the software execution time is heavily dependent on program structure, algorithmic implementation, and the software development language of choice [59]. The C++ programming language was chosen as the software development language of choice. This is because the C++ programming language facilitates software portability across several different operating systems as well as various hardware-dependent machine architectures [61]. The software development will target two different hardware platforms: the standard IBM® PC running the Microsoft Windows® operating system [62], and the massively parallel SGi Altix® supercomputer running the SGi ProPack® operating system [63]. The SGi Altix® architecture features 16 64-bit Intel Itanium® 2 processors with 6MB of L3 cache, running at 1.5GHz with a combined shared memory subsystem of 40GB. The SGi ProPack® operating system is based on the Red Hat Enterprise Server® Linux distribution with an SGI software layer that features a high-performance scheduler with support for very large architectures with up to 128 CPUs.

With the choice of programming language and hardware platforms, the next step is the implementation of an efficient program structure. For this, we chose a system made up of three functional units developed as independent software blocks. These are identified as the Pre-Processor, the Processor and the Post-Processor units, respectively. The Pre-Processor unit is a software block that accepts as inputs the mesh file that approximates the conducting surface of the MRI coil, as well as the mesh files of any inhomogeneous body in the vicinity of the coil. These mesh files can be obtained using any meshing software that is capable of generating triangular and tetrahedral meshes of surface and volume discretizations. In addition, user-defined inputs such as resonance frequency, surface conductance and choice of input ports as well as ports containing lumped element components, are fed as inputs to the Pre-Processor units. The Pre-Processor will act on these inputs and generate the necessary voltage, resistance, capacitance and element definition files. A simplified diagram depicting the input–output relationship of the Pre-Processor unit is shown in Fig.4.1. The Pre-Processor unit was developed specifically as a Graphical User Interface (GUI) application for the Microsoft Windows® operating system using the

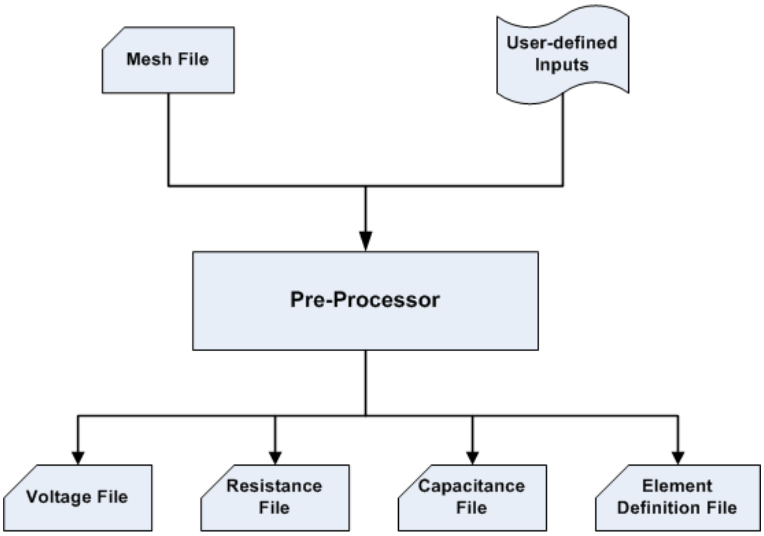

Figure 4.1: Input–Output relationship of the Pre-Processor unit.

Microsoft Visual Studio.Net® C++ development environment and the OpenGL® Application Programming Interface (API) graphics library [64]. The Microsoft Visual Studio.Net® C++ development environment provides the Microsoft Foundation Class and associated Template library (MFC&T) that provide the tools needed to create full-featured Windows-based applications. OpenGL® is the leading industry standard API for interactive 3D graphics rendering and 2D imaging. It provides device-independent support for common low-level 3D graphics drawing operations such as polygon specification, basic lighting control, transformation specification, and frame buffer operations like blending and depth-buffering. The OpenGL® API graphics library also comes bundled in the Microsoft Visual Studio.Net® C++ development environment. The main GUI of the Pre-Processor unit is made up of a top level menu system, a toolbar, a docked dialog bar and a status bar as shown in Fig.4.2. The top level menu system allows the users to specify and configure the system to be solved. The dialog bar on the left of the graphical user interface contains display and control options. The toolbar, located just under the top level menu system, provides a subset of the functionality of the top level menu system. Its main purpose is to serve as a shortcut for frequently used menu items.

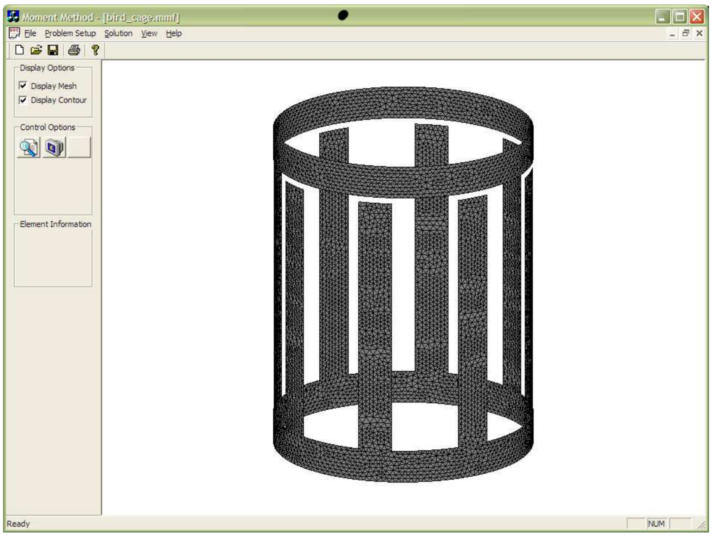

☑ Display Mesh
☑ Display Contour

Figure 4.2: The main windows-based GUI of the Pre-Processor unit. The picture shows the mesh discretization of a birdcage coil during preprocessing.

The Processor unit forms the core foundation of the software implementation of the MoM numerical model. It acts on the outputs of the Pre-Processor unit and produces a numerical solution of the underlying MoM integral equations. The input–output relationship of the Processor unit is shown in Fig.4.3. The Processor unit was developed as a console-based application in order to facilitate portability between Microsoft Windows® and the SGi ProPack® operating systems. We introduced an algorithmic implementation in the Processor unit that is based on the concept of operating system threads [65]. In essence, operating system threads can be defined as semi-independent program segments that define interfaces and functionality to support multiple flows of control within a defined operating system process [65]. Also, operating system threads provide the basic building blocks behind task switching and event scheduling in the main system kernel of multitasking operating systems such as Microsoft Windows® and SGi ProPack®. The implemented algorithm allows us to efficiently distribute the task of filling the impedance matrix across multiple CPU cores that make up the intended hardware architecture. The number of operating system threads in the Processor unit is equal to the number of CPU cores in the underlying

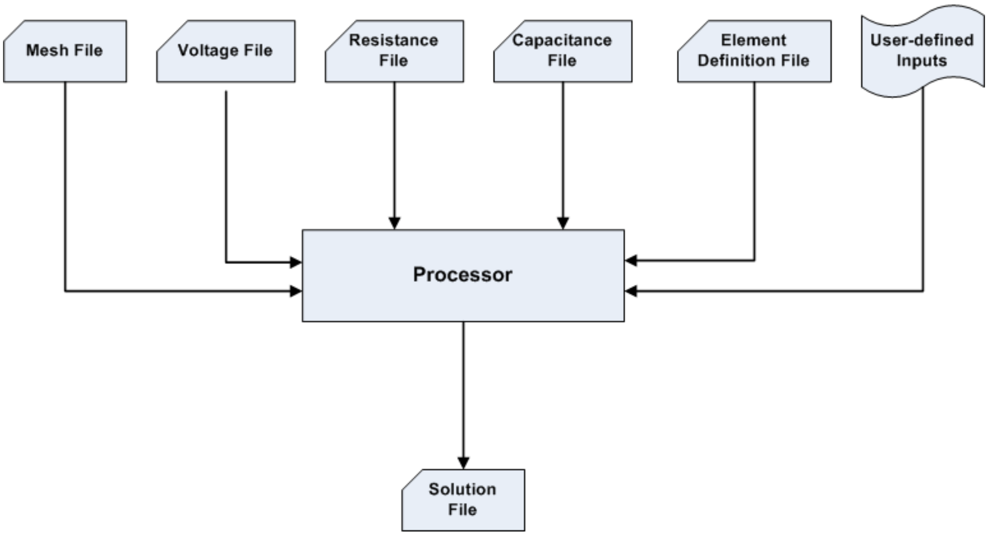

Figure 4.3: Input–Output relationship of the Processor unit.

hardware platform. This effectively reduces computation time by a factor of the number of operating system threads. After the task of filling the impedance matrix, the solution of the resulting MoM matrix equation is obtained by using the Linear Algebraic Package (LAPACK) available as part of the Intel® Math Kernel Library (MKL) [66]. It is worth noting that the Intel® MKL library is also structured around the concept of operating system threads. The output of the Processor unit is the numerical solution of the underlying MoM matrix equation. This is essentially the unknown surface current density coefficients as defined in (3.26), as well as the unknown total volume current density coefficients defined in (3.30). These results are subsequently saved in the appropriate format in the solution file on an element-by-element basis. The Post-Processor unit uses the solution file together with the mesh files, the element definition file and the user-defined input file to determine the electromagnetic field parameters of interest. Again, the Post-Processor unit was developed as a console-based application in order to facilitate portability across Microsoft Windows® and SGi ProPack®. A simplified schematic block of the Post-Processor unit is shown in Fig.4.4. In addition, the Post-Processor unit was also developed around the concept of operating system threads. This effectively reduces post-processing time by the

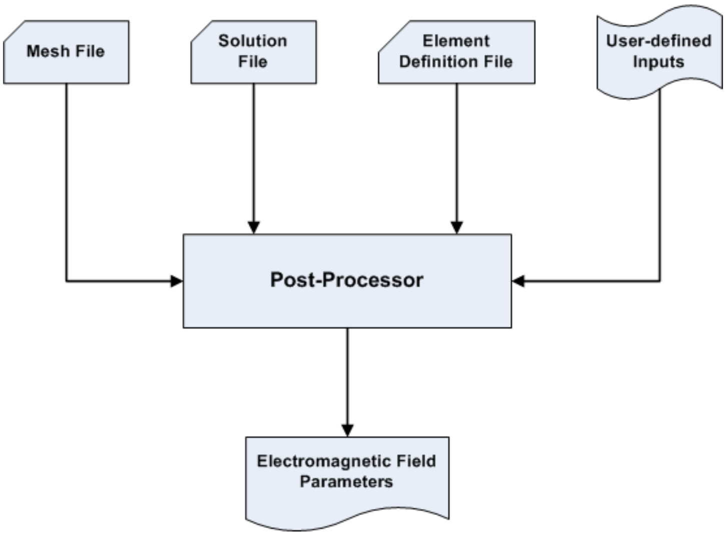

Figure 4.4: The Post-Processor unit showing its inputs and outputs.

number of available CPU cores in the underlying hardware platform. The required electromagnetic field parameters are computed and saved in the appropriate format for visualization in both 2D and 3D using the Tecplot® Numerical Simulation and Visualization software [67]. A typical 3D visualization using Tecplot® is shown in Fig.4.5. It shows the surface current density on a conducting ring.

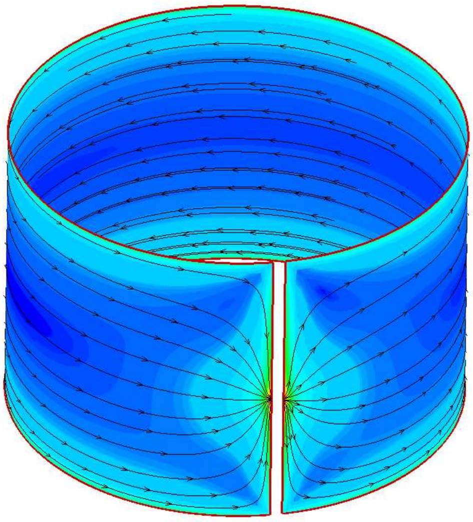

Figure 4.5: 3D visualization of the surface current density on a conducting ring using Tecplot®.The color map signifies the magnitude of the surface current density, and the stream lines indicate the direction of its flow.

4.2 RF Coil Equivalent Circuit Model

In order to determine an equivalent circuit model of an RF coil from the solution of its MoM matrix equation, we utilized the system arrangement shown in Fig.4.6. The linear equivalent circuit model will provide a complete network description of the RF coil as seen from its ports. Such a description can be obtained by computing the scattering matrix **S** of the RF coil system. For the N-port RF coil system of Fig.4.6, the scattering matrix **S** is defined as

$$\begin{bmatrix} V_1^- \\ V_2^- \\ \vdots \\ V_N^- \end{bmatrix} = \begin{bmatrix} S_{11} & S_{12} & \cdots & S_{1N} \\ S_{21} & S_{22} & \cdots & S_{2N} \\ \vdots & & & \vdots \\ S_{N1} & \cdots & \cdots & S_{NN} \end{bmatrix} \begin{bmatrix} V_1^+ \\ V_2^+ \\ \vdots \\ V_N^+ \end{bmatrix}$$

$$\mathbf{V}^- = \mathbf{S} \cdot \mathbf{V}^+ \tag{4.1}$$

with the vector $\mathbf{V}^-$ defined as the amplitude of the voltage wave reflected from each of the N ports, and $\mathbf{V}^+$ is the amplitude of the voltage wave incident on each port. The

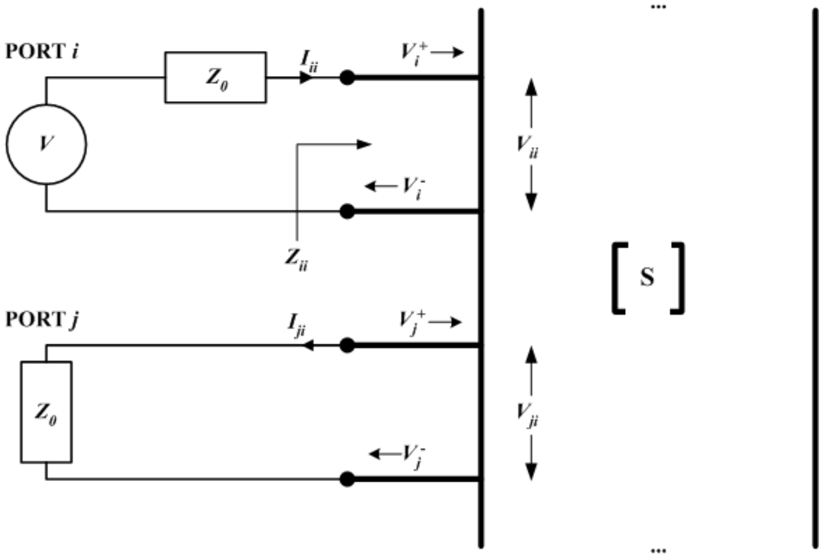

Figure 4.6: Determination of an equivalent circuit of an RF coil from its MoM solution.

scattering matrix **S** reflects a representation that is more in accord with direct measurements because the incident and reflected voltage waves can be obtained through physical measurements with a vector network analyzer. Each elements of **S** can be determined with

$$S_{ji} = \left. \frac{V_j^-}{V_i^+} \right|_{V_k^+=0,\ \text{for}\ i \neq k} \tag{4.2}$$

where S_{ji} is defined as the transmission coefficient from port i to port j with all other ports are terminated by the matched impedance Z_0. When $i = j$, the definitive term changes into a reflection coefficient and it now characterizes S_{ii}. Looking at the N port coil system of Fig.4.6, a voltage source V with source impedance Z_0 is applied across port i while all other ports, including port j are terminated by matched loads. This configuration is defined as part of the User-defined inputs in the Pre-Processor unit of the MoM implementation. For this circuit arrangement, the currents I_{ii} and I_{ji} are determined by solving the underlying MoM matrix equations for the case of the loaded RF coil. Once a solution for the port current I_{ii} is obtained, the input impedance Z_{ii} at port i can be determined as

$$Z_{ii} = \frac{V_{ii}}{I_{ii}} = \frac{V - I_{ii}Z_0}{I_{ii}} \tag{4.3}$$

The element S_{ii} of **S** can now be determined as the reflection coefficient at port i when all other ports are terminated by matched loads. This can be written as

$$S_{ii} = \frac{V_i^-}{V_i^+} = \frac{Z_{ii} - Z_0}{Z_{ii} + Z_0} \tag{4.4}$$

Similarly, the transmission coefficient S_{ji} from port i to port j when all other ports are terminated by matched loads can subsequently be found using (4.2). From Fig.4.6, we note that

$$
\begin{aligned}
V_{ii} &= V_i^+ + V_i^- \\
&= (1 + S_{ii})V_i^+
\end{aligned}
\tag{4.5}
$$

Now since port j is terminated by the matched load Z_0, we have that $V_j^+ = 0$. This implies that

$$V_{ji} = V_j^- = I_{ji}Z_0 \tag{4.6}$$

Finally, we can express the transmission coefficient S_{ji} observed at port j in the form

$$S_{ji} = \frac{I_{ji}Z_0}{V - I_{ii}Z_0}(1 + S_{ii}) \tag{4.7}$$

With the aid of (4.4) and (4.7), we have been able to realize an equivalent circuit model in terms of the scattering matrix **S** of an RF coil. We would like to add that **S** completely characterizes the electrical circuit properties of the RF coil. This will allow us to determine pertinent circuit parameters such as decoupling capacitors, as well as tuning and matching capacitors required to resonate the RF coil at its Larmor resonance frequency.

4.3 Tuning and Matching Requirement

The process of tuning and matching RF coils to their associated coupling circuits can be achieved by using lumped element capacitors in a two-element or L-section network configuration. All RF coils possess an inherent inductance due to the spatial distribution of their conductors around the region of interest, and also because of the size of their current-carrying conductors. As such, RF coils will be highly efficient when they are operated at their resonance frequencies. The tuning process establishes a resonance condition in the RF coil at the desired Larmor frequency. The resonance phenomenon guarantees some form of rudimentary signal amplification as well as frequency selectivity. The result is that the typically weak NMR signal will equate to large signal changes in the RF coil. This large signal change, although still not strong enough, can further be amplified and processed in order to reveal important information about the properties of the sample.

Matching is an important requirement for the design of RF circuits. It guarantees the transfer of maximum power from the signal source to the load. According to the maximum power transfer or conjugate matching theorem, maximum power is transferred from the signal source if, and only if, the input impedance presented at the signal source is equal to the complex conjugate of the source impedance. A proof of the conjugate matching theorem is given in [68] and [69]. It should be noted that conjugate matching does not necessarily yield a system with the best efficiency. As an example, consider the case where the source impedance is real and the input impedance presented to the source is also real. In this case, the load and the generator are matched and there are no reflections on the transmission line. But only half the power generated is delivered to the load yielding an efficiency of 50%. In essence, the efficiency of the system can only be improved by making the source impedance as small as possible.

4.3.1 L-Section Tuning and Matching

The L-section network is the simplest type of narrow band matching network used in the tuning and matching of RF coils. It uses two lumped reactive elements that are arranged in an L-section configuration to match arbitrary load impedances to a transmission line. There exist two possible configurations for L-section networks. These are the shunt and series configurations as illustrated in Fig.4.7(a) and (b). In these configurations, the load impedance Z_L is essentially the input impedance at any

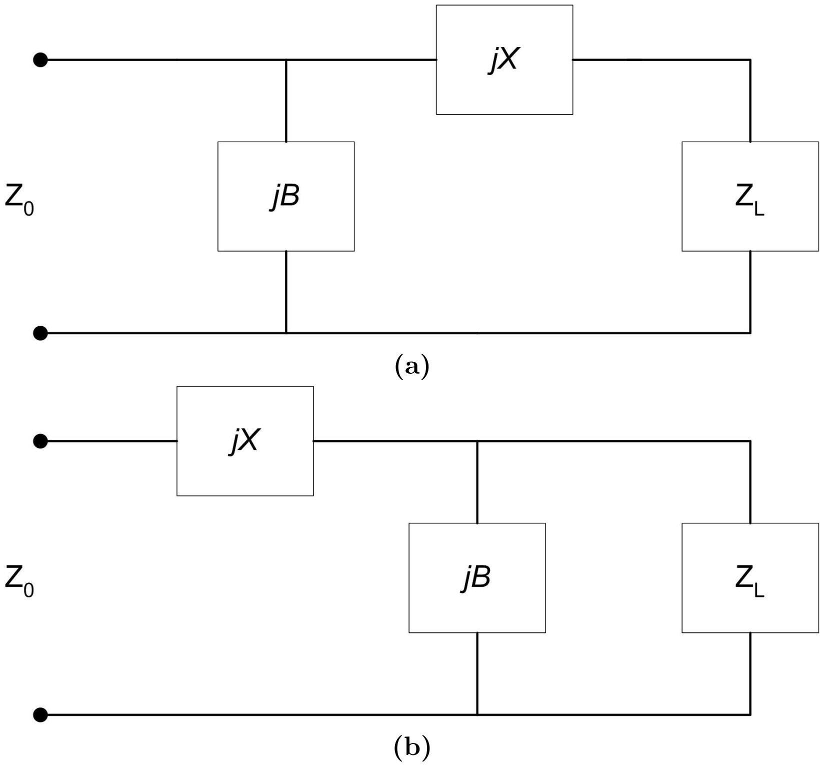

Figure 4.7: L-section network configuration: (a) Shunt configuration, and (b) Series configuration.

of the receiving or transmitting ports of the RF coil. This impedance can be obtained from the scattering matrix **S** using any of the transformations presented in [68]. As usual, the characteristic impedance of the connecting transmission line is denoted by Z_0. The lumped reactive elements jB and jX in each configuration could be either inductive or capacitive, depending on the load impedance Z_L. Thus, there exist eight distinct possibilities for L-section matching using a combination of capacitors and inductors. Let us now consider the case of tuning and matching the impedance of Z_L to the transmission line with characteristic impedance Z_0. In this case, the coil impedance Z_L can be written as

$$Z_L = R_L + jX_L \tag{4.8}$$

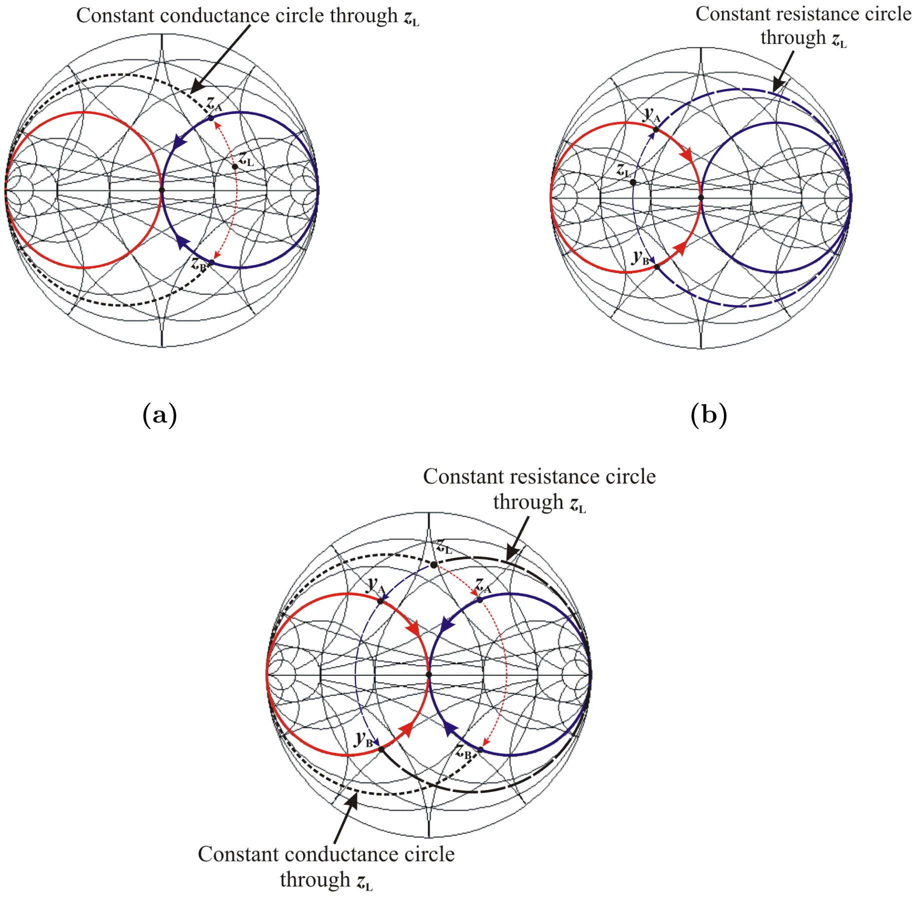

(a) **(b)**

(c)

Figure 4.8: Possible locations of z_L on a Smith chart: (a) z_L resides in the unit $r = 1$ circle, (b) z_L resides in the unit $g = 1$ circle, and (c) z_L resides outside both circles. The unit $r = 1$ circle is shown in blue while the unit $g = 1$ circle is shown in red.

or in normalized form with respect to Z_0 as

$$z_L = \frac{Z_L}{Z_0} = \frac{R_L}{Z_0} + j\frac{X_L}{Z_0} = r_L + jx_L \tag{4.9}$$

where R_L denotes the resistive component, and X_L the reactive component of the coil impedance. Based on the nature of the normalized impedance z_L, it can reside in three exclusive regions on the Smith chart as illustrated in Fig.4.8. We now consider each of the three cases depicted in Fig.4.8 separately. When z_L lies within the $r = 1$ circle as in Fig.4.8(a), there exists a unique constant conductance circle that passes through z_L since $r_L > 1$. The constant conductance circle will intersect the $r = 1$ circle at two distinct points z_A and z_B as shown in Fig.4.8(a). These points are complex conjugates of each other, and can be expressed in the form $z_{A,B} = 1 \pm j\Delta$, where the + sign refers to the point z_A, and the - sign refers to its conjugate z_B with Δ representing its normalized reactance component. The normalized admittance y_L is given by

$$y_L = \frac{1}{z_L} = \frac{1}{r_L + jx_L} = \frac{r_L}{r_L^2 + x_L^2} - j\frac{x_L}{r_L^2 + x_L^2} = \alpha - j\beta \tag{4.10}$$

Similarly, the normalized admittances of z_A and z_B is given by

$$y_{A,B} = \frac{1}{z_{A,B}} = \frac{1}{1 \pm j\Delta} = \frac{1}{1 + \Delta^2} \pm j\frac{\Delta}{1 + \Delta^2} \tag{4.11}$$

Since $y_{A,B}$ and y_L reside on the same constant conductance circle, they must have equal real components, or equal conductance components. Thus, we have

$$\alpha = \frac{1}{1 + \Delta^2} \tag{4.12}$$

Solving for Δ gives

$$\Delta = \sqrt{\frac{1}{\alpha} - 1} \tag{4.13}$$

Hence, we conclude that the L-section configuration of Fig.4.7(b) is needed to transform z_L into a unit normal impedance, and thus tune and match Z_L to the transmission line when z_L lies exclusively in the $r = 1$ circle. The reactance jB that is required to transform z_L to either z_A or z_B, along the constant conductance circle as shown in Fig.4.8(a), can be determined from (4.10) and (4.11) as

$$jB = \frac{-jZ_0}{\frac{\pm\Delta}{1 + \Delta^2} + \beta} \tag{4.14}$$

The remaining reactance jX that is required to transform $z_{A,B}$ to a unit normal impedance is simply given as

$$jX = \pm jZ_0\Delta \tag{4.15}$$

Next, we consider the situation when z_L lies exclusively in the $g = 1$ circle as illustrated in Fig.4.8(b). We observe that in this senario, z_L and points y_A and y_B must reside on the same constant resistance circle as shown. In this case, y_A and y_B can be expressed in the form

$$y_{A,B} = 1 \pm jK \tag{4.16}$$

since $y_{A,B}$ reside on the $g = 1$ conductance circle as shown in Fig.4.8(b). The corresponding impedances z_A and z_B can be found easily from (4.16) as

$$z_{A,B} = \frac{1}{y_{A,B}} = \frac{1}{1 \pm jK} = \frac{1}{1+K^2} \pm j\frac{K}{1+K^2} \tag{4.17}$$

Now since z_L and $z_{A,B}$ reside on the same constant resistance circle, they must have equal resistive components. Thus, we have that

$$r_L = \frac{1}{1+K^2} \tag{4.18}$$

from which we determine K as

$$K = \sqrt{\frac{1}{r_L} - 1} \tag{4.19}$$

Clearly, the L-section configuration of Fig.4.7(a) is required in order to transform z_L into a unit normal impedance, thus tuning and matching Z_L to the transmission line when z_L lies exclusively in the $g = 1$ circle. The series reactive component jX that is required to transform z_L to either point y_A or y_B can be determined using (4.9) and

(4.17) as

$$jX = jZ_0\left(\frac{\pm K}{1+K^2} - x_L\right) \tag{4.20}$$

Similarly, the reactive component jB in Fig.4.7(a) is easily determined as

$$jB = \pm j\frac{Z_0}{K} \tag{4.21}$$

Lastly, we consider the final case when the impedance z_L does not reside in either unit circles. This situation is depicted in Fig.4.8(c). In this case, both a constant conductance circle and a constant resistance circle can be drawn through z_L as shown. The implication of this statement is that both L-section configurations of Fig.4.7 can be used to tune and match z_L to the transmission line when z_L does not lie in either circle. The values of the required reactive components jX or jB can easily be determined using (4.14) and (4.15), or (4.20) and (4.21).

In conclusion, we would like to add that capacitive only solutions are sort after for the implementation of the L-section network because capacitors have lower losses and smaller physical dimensions when compared with inductors.

4.3.2 S-Matrix Approach to Tuning and Matching

In addition to L-section tuning and matching, another approach based on **S**-matrix reduction finds prominent use in situations where reactive components are to be distributed along the profile of the RF coil. The distribution of reactive components, especially capacitive components along the coil profile, is very important in the elimination of noise resulting from switching gradient fields. Also, it is sometimes beneficial to distribute reactive components in order to maintain reactive symmetry, and hence improve geometric decoupling of neighboring coils in an RF coil array. In the general L-section tuning and matching described in the previous section, the MoM is used to determined the input impedance Z_L of the RF coil. Thereafter, a choice of network topology as well as suitable values of the reactive components jB and jX are determined using the equations derived. When reactive components are to be distributed along the coil profile, several iterations using the MoM are required in order to determine Z_L, since the values of the distributed reactances are unknown. This will invariably lead to a significant increase in computation time.

The **S**-matrix reduction technique provides a solution to this problem by creating extra input ports at all positions where reactive components are located. In effect, the N-port coil system becomes an $N + M$-port system where M is the total number of reactive components distributed along the coil profile. The MoM is applied to the $N + M$ port system in order to determine its scattering matrix $\mathbf{S}$. The resulting $(N + M) \times (N + M)$ **S**-matrix is then reduced into its original form by terminating the M extra ports with reactive components that guarantee the correct **S**-matrix response. To better explain the reduction process, consider a system with N ports. The elements S_{ij} of the **S**-matrix associated with these ports can be obtained using (4.4) and (4.2). Now if an arbitrary port k is terminated by reactive component X_L, there will be wave reflection at port k since X_L is not equal to the characteristic impedance Z_0. The reflection coefficient Γ_k at port k can be determined from

$$\Gamma_k = \frac{V_k^+}{V_k^-} = \frac{X_L - Z_0}{X_L + Z_0} \tag{4.22}$$

As a result of the termination of port k, each element $\mathtt{s}_{ij}$ of the reduced $N - 1$ port system will be modified according to

$$\mathtt{s}_{ij} = S_{ij} + S_{ik} S_{kj} \frac{\Gamma_k}{1 - S_{kk}\Gamma_k} \tag{4.23}$$

When $i = j$, the value of X_L that makes $\mathtt{s}_{ij}$ a minimum is the value required to tune and match the coil system. If $i \neq j$, then the value of X_L that minimizes $\mathtt{s}_{ij}$ reactively decouples the coil system. The minimizing value of X_L can be determined by plotting a graph of $\mathbf{s}_{ij}$ against X_L. When several ports are to be terminated, (4.23) can be applied one port at a time until the original **S**-matrix is completely reduced and minimized into $\mathbf{s}_{ij}$. Clearly, this technique provides considerable savings in computation time since no MoM simulation run is required after the **S**-matrix has been determined. In summary, **S**-matrix reduction is a very versatile technique and can also be used to determine the reactive components required to implement capacitive or inductive decoupling of nearest-neighbor RF coils in an RF coil array.

4.4 Simulation Models and Validation

In this section, we discuss the validation of our MoM implementation based on four different simulation models. These simulation models have been developed explicitly to validate the three different integral equations that form the foundation of our MoM implementation. These base equations are the Surface-Surface, Volume-Volume and Surface-Volume integral equations as discussed in Section 3.4. For the first simulation model, we consider the determination of the inductance of a circular ring of negligible or very thin cross-section. The second simulation model is based on the classic electromagnetic problem of scattering of an incident electromagnetic wave by a dielectric sphere. The third simulation model also considers scattering of an electromagnetic wave by a dielectric sphere, but in this case the source of the electromagnetic wave is a thin circular ring of negligible cross-section. Lastly, we consider the determination of the frequency response of a loaded low-pass quadrature Bird Cage RF coil. Of the four models considered, the first two models have associated analytical solutions that have been used as comparisons. However, the last two simulation models do not have associated analytical solutions. Consequently, their validation was based on strict observation in accordance with established electromagnetic principles, as well as comparisons with actual physical measurements of a constructed prototype based on the models. We begin by presenting the four simulation models and discussing their implementation. Thereafter, we present results of the MoM simulations and discuss their significance in our validation process.

4.4.1 Inductance Calculation Model

We now consider the implementation and validation of a simulation model based on the determination of inductance. Our goal is to determine the inductance of thin circular rings of negligible or very thin cross-sections, and compare them with those obtained from established formulas that were developed in [70]. The diagram of a thin circular ring of negligible cross-section is shown in Fig.4.9. As seen, the radius of the circular ring is denoted by r, while the width of the ring is denoted by w. Several circular ring models were created that differ from one another by variations in r and w. We begin our modeling implementation by creating triangular surface meshes of the thin circular rings using EasyMesh [71]. EasyMesh generates two dimensional, unstructured, Delaunay, and constrained Delaunay triangulations in general domains. As such, another application was developed explicitly to transform the generated 2D meshes into 3D surface mesh representations of the circular rings. This application used a simple rectangular-to-cylindrical coordinate transformation to convert

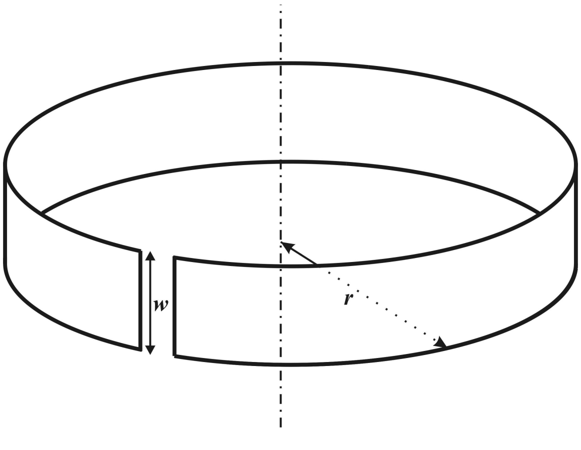

Figure 4.9: A circular ring of negligible or very thin cross-section.

Table 4.1: Radius and width configurations of the thin circular rings with all dimensions in meters

Radius (m)	**Width** (m)	**Total Triangles**	**Total RWG Elements**
0.06	0.015	13076	19225
0.06	0.020	11150	16410
0.06	0.025	13922	20564
0.06	0.030	11586	17110
0.06	0.035	15612	23126
0.05	0.020	9312	13701
0.055	0.020	10252	15088
0.065	0.020	12136	17863
0.07	0.020	13078	19251

the nodes of the 2D meshes into equivalent nodes that are wrapped on a cylinder in 3D space. A total of nine thin circular ring meshes were considered. Fig.4.10 shows their 3D surface meshes after coordinate transformation. The configurations used for the radii and widths, as well as the total number of triangles and RWG elements in the surface discretization is as tabulated in Table.4.1. The source of excitation was chosen to be a delta-gap voltage source of 1V with a corresponding frequency of 100kHz. The solution for the surface currents on the thin circular rings are then obtained using our MoM implementation. Since the problem setup does not involve any inhomogeneous bodies, the surface current solutions were all obtained by solving the Surface-Surface MoM equation for the unknown current distributions. Once the surface current solutions have been obtained using the MoM, the inductance of each ring can then be determined from the ring impedance at the excitation port. This impedance can easily be obtained from the relationship between the port voltage and port current. For verification purposes, the inductance of each ring was then determined using the inductance calculation formulas presented in [70] and later compared with those obtained using the MoM formulations. The results of the comparison are as tabulated in Table.4.2. There is certainly good agreement between the inductance values obtained using the MoM formulation and the inductance calculation. This undoubtedly validates our implementation of the MoM using Surface-Surface MoM

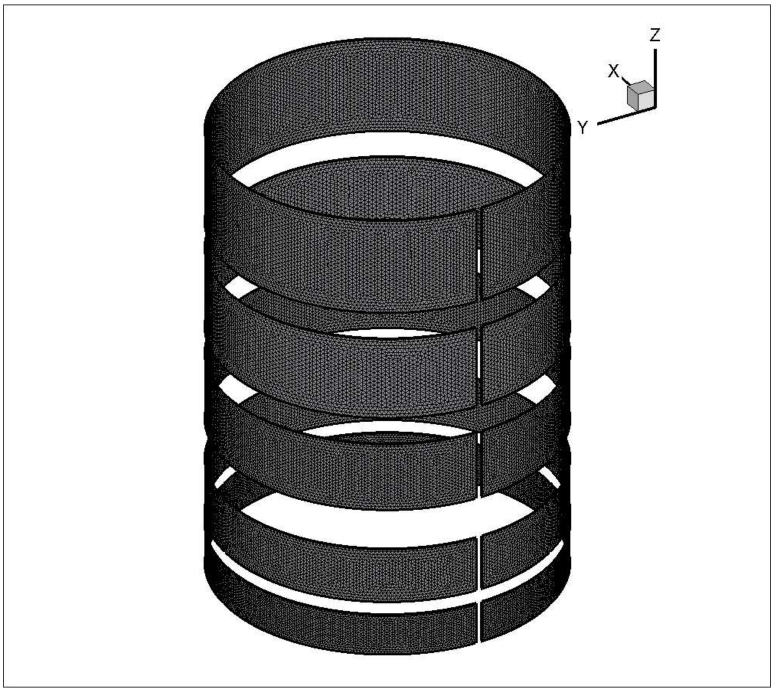

(a) Meshes of constant radii

(b) Meshes of constant widths

Figure 4.10: 3D surface meshes of thin circular rings: (a) ring meshes with equal radii but variable width, and (b) ring meshes with variable radii and equal widths.

Table 4.2: Inductance values for thin circular rings. Inductance obtained using the MoM is compared against those obtained using established formulas

		Inductances	
Radius (m)	**Width** (m)	**MoM** (μH)	**Formula** (μH)
0.06	0.015	0.2167	0.2186
0.06	0.020	0.1953	0.1971
0.06	0.025	0.1794	0.1809
0.06	0.030	0.1667	0.1678
0.06	0.035	0.1558	0.1572
0.05	0.020	0.1518	0.1533
0.055	0.020	0.1733	0.1748
0.065	0.020	0.2182	0.2192
0.07	0.020	0.2410	0.2431

integral equations. Finally, we would like to add that the inductance calculation formulas presented in [70] only provides an approximation of the actual inductance, and this approximation is independent of frequency.

4.4.2 Incident Wave Scattering Model

In this section, we discuss the implementation of an incident wave scattering model to validate our Volume-Volume MoM integral equation. The incident wave scattering model completely embodies the classical problem of scattering of an incident wave by a dielectric sphere. Analytical solutions to this classic problem are readily available in the form of the so-called Mie Series [72]. For the implementation of the scattering model, we consider a sphere of radius r=0.02m. Volumetric discretization of the sphere resulted in a volume mesh with 23048 tetrahedra and 28477 edges. The number of independent basis edges was then determined using the procedure outlined in Section 3.3.3. This resulted in 24093 identified independent basis edges. A mesh of the discretized spherical region is as shown in Fig.4.11. The volume mesh was generated using the simple mesh generator of [73]. The sphere was assigned a dielectric constant of $\varepsilon_r = 2.0$, while its conductance was varied in accordance with $\sigma = 0.0, 0.2, 0.5, 0.75, 1.0$S/m. The incident electromagnetic wave was chosen to be

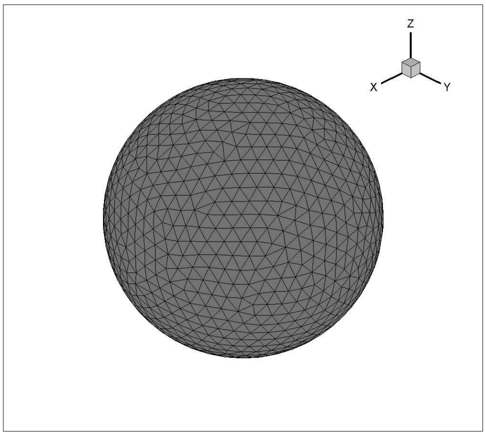

Figure 4.11: Volumetric discretization of a sphere of radius r=0.02m.

a plane wave traveling along the positive z-axis with an amplitude of 1.0V/m and a frequency of 200MHz. It is assumed that the electric field component of the wave oscillates along the positive x-axis. Results from our MoM implementation with the configuration given above, were compared against those obtained using the Mie series implementation with the same input configuration. The results of the comparison are as depicted in Fig.4.12 to Fig.4.16. We observe that our numerical MoM solutions are well behaved, and hence provide us with values of electric and magnetic fields that agree very well with exact values. Also, for situations where there is an associated conductance, $\sigma > 0$, we see that the MoM solutions clearly describe wave attenuation in the volume as expected. In conclusion, these results demonstrate excellent performance of our MoM implementation and help validate its accuracy and correctness.

4.4.3 Circular Ring Scattering Model

In this arrangement, we also consider the scattering of an incident wave by a dielectric sphere. However, in this case, the source of the incident wave is radiation from a circular ring of negligible cross-section. This model was developed to help validate our complete MoM implementation of the Surface-Volume MoM integral equation

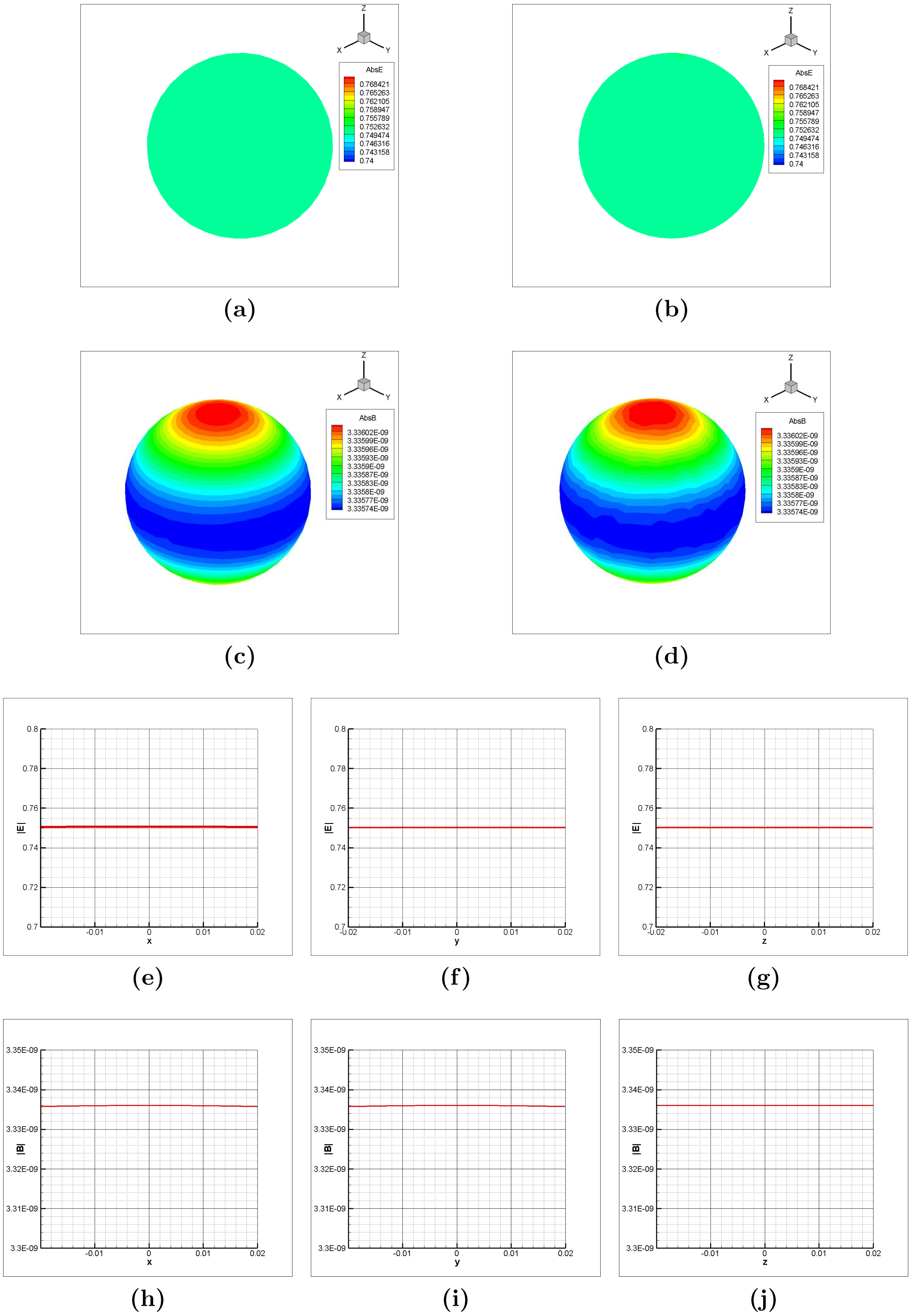

Figure 4.12: Mie series solution versus MoM solution for $\varepsilon_r = 2.0$ and $\sigma = 0.0$ S/m. (a) and (c) indicate the Mie series solution for the magnitude of the electric and magnetic fields on the surface of the sphere, while (b) and (d) show the corresponding MoM solutions. (e), (f) and (g) show the magnitude of the electric field along the x, y and z axes, while (h), (i) and (j) show the corresponding magnetic field. The Mie series solution is shown as solid lines, while the MoM solution is shown as dashed lines. All spatial dimensions are in [m], with the electric and magnetic fields in V/m and T.

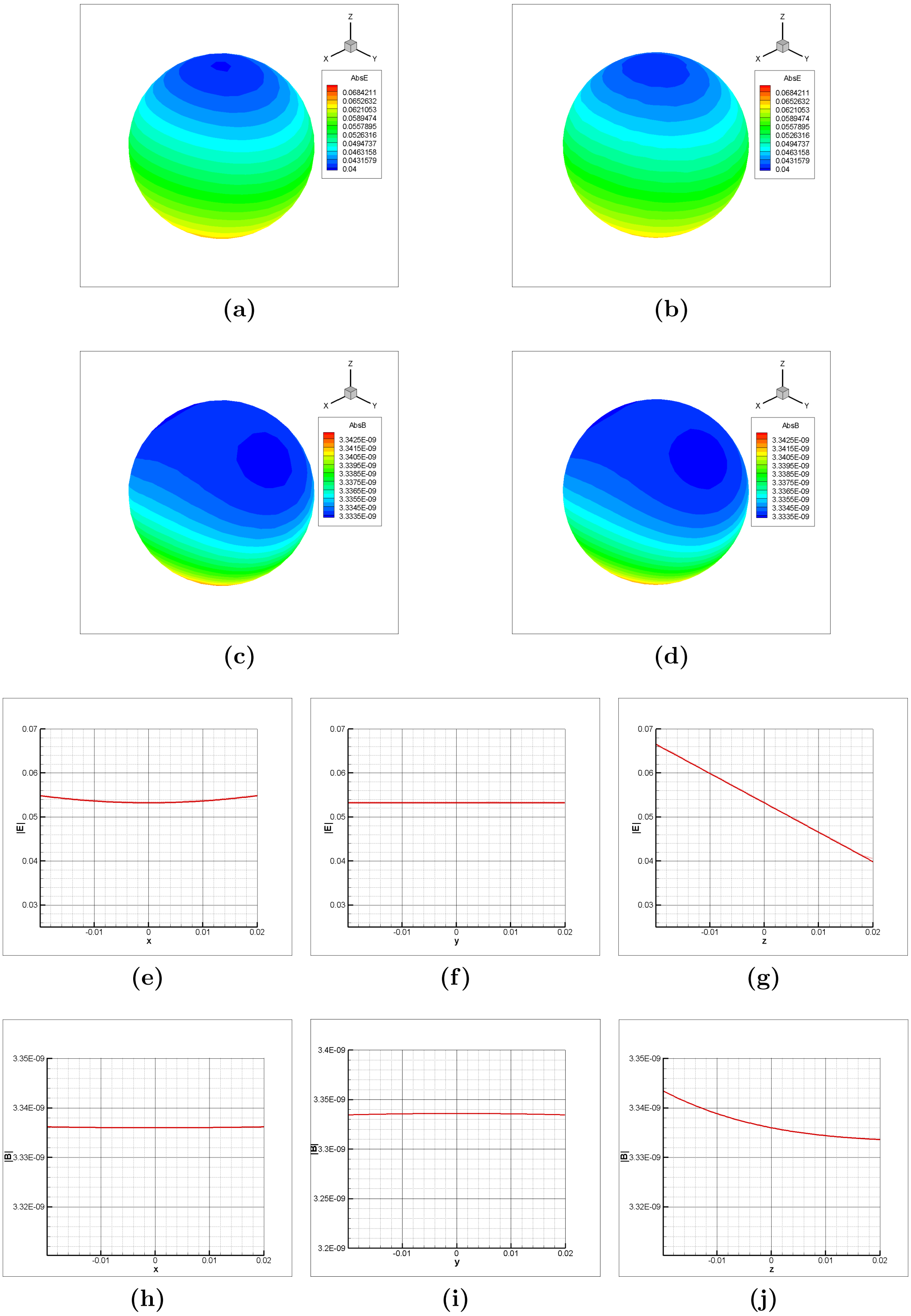

(a) **(b)** **(c)** **(d)** **(e)** **(f)** **(g)** **(h)** **(i)** **(j)**

Figure 4.13: Mie series solution versus MoM solution for $\varepsilon_r = 2.0$ and $\sigma = 0.2$ S/m. (a) and (c) indicate the Mie series solution for the magnitude of the electric and magnetic fields on the surface of the sphere, while (b) and (d) show the corresponding MoM solutions. (e), (f) and (g) show the magnitude of the electric field along the x, y and z axes, while (h), (i) and (j) show the corresponding magnetic field. The Mie series solution is shown as solid lines, while the MoM solution is shown as dashed lines. All spatial dimensions are in [m], with the electric and magnetic fields in V/m and T.

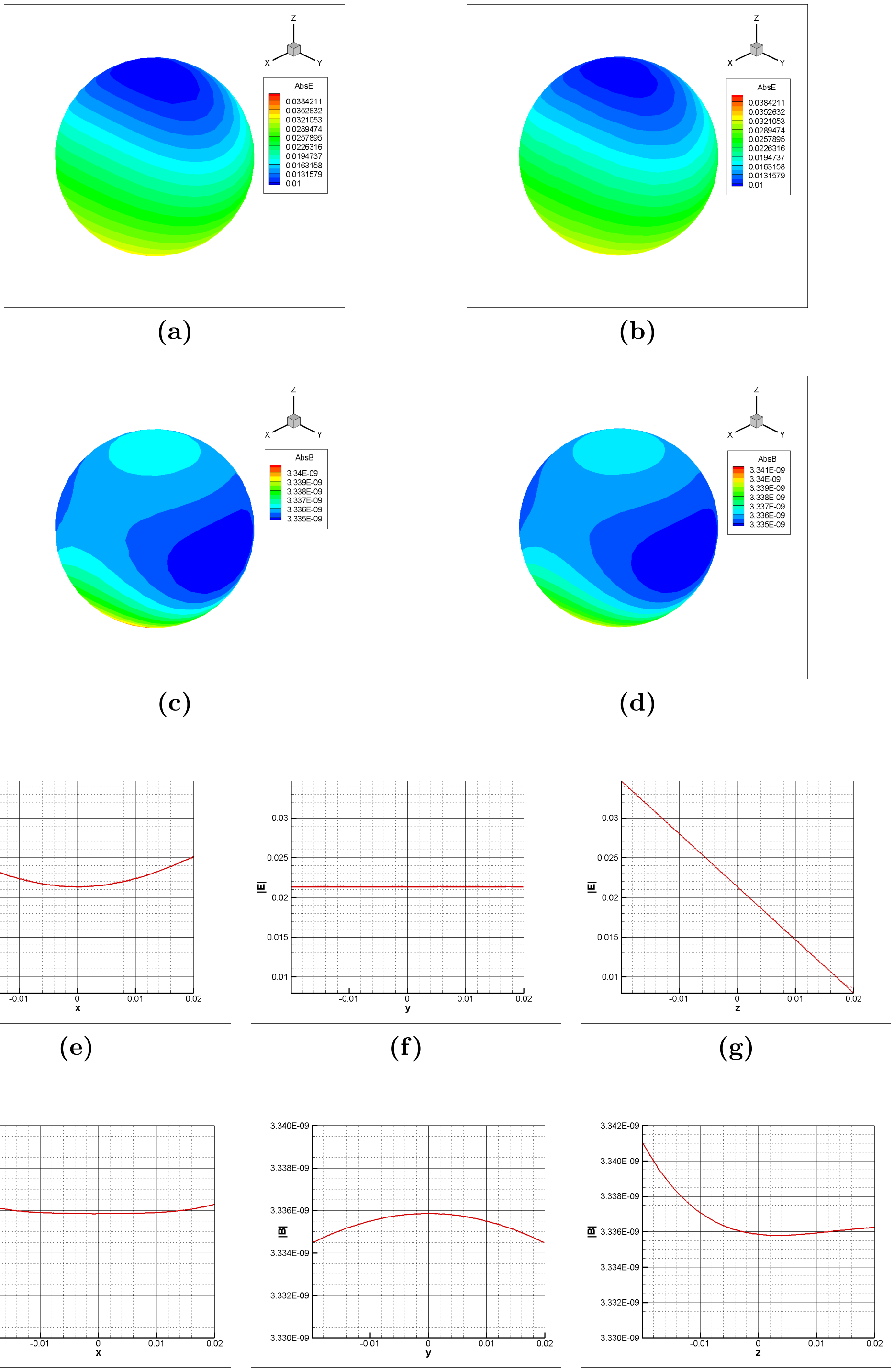

(a) (b) (c) (d) (e) (f) (g) (h) (i) (j)

Figure 4.14: Mie series solution versus MoM solution for $\varepsilon_r = 2.0$ and $\sigma = 0.5$ S/m. (a) and (c) indicate the Mie series solution for the magnitude of the electric and magnetic fields on the surface of the sphere, while (b) and (d) show the corresponding MoM solutions. (e), (f) and (g) show the magnitude of the electric field along the x, y and z axes, while (h), (i) and (j) show the corresponding magnetic field. The Mie series solution is shown as solid lines, while the MoM solution is shown as dashed lines. All spatial dimensions are in [m], with the electric and magnetic fields in V/m and T.

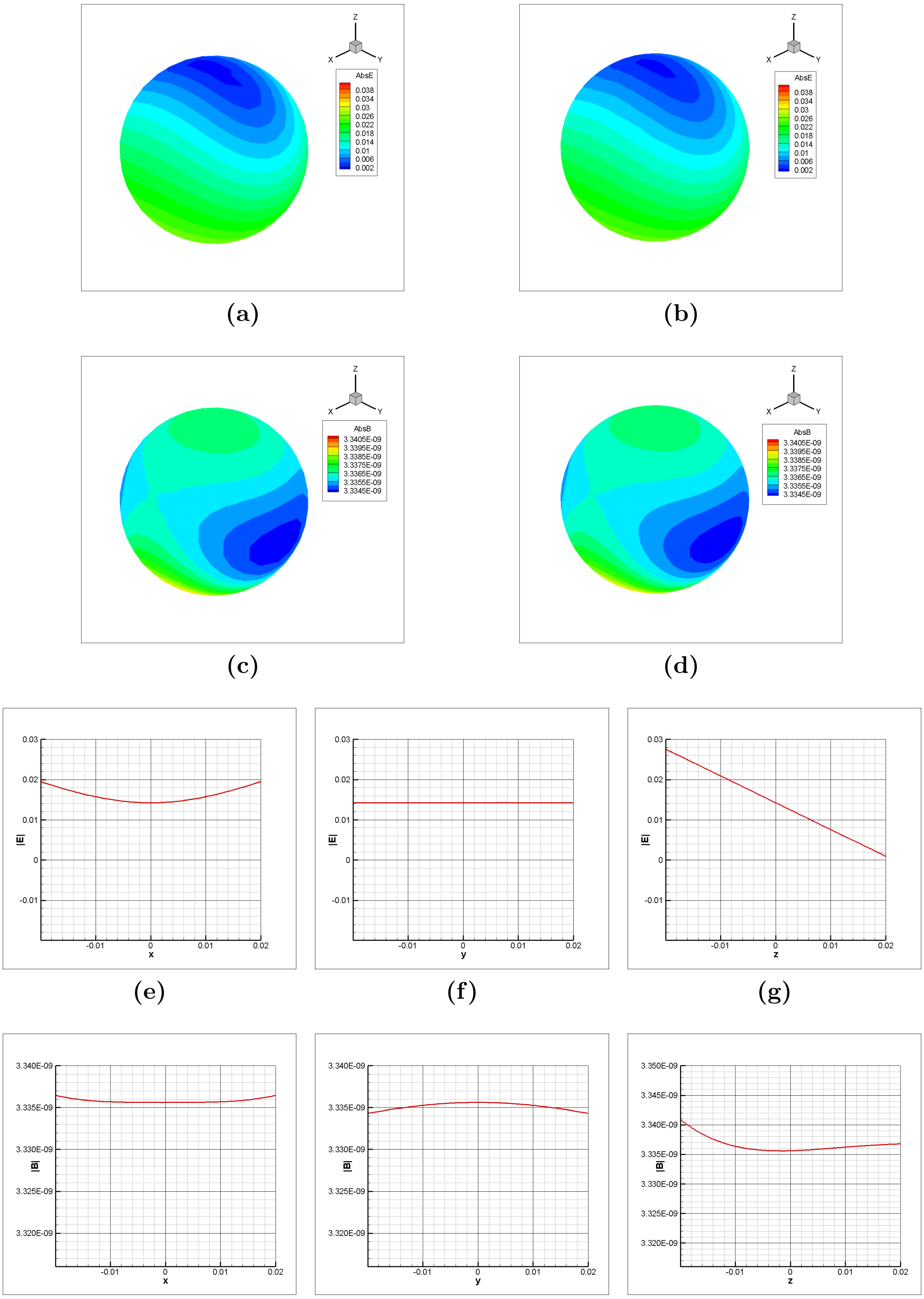

(a) **(b)**

(c) **(d)**

(e) **(f)** **(g)**

(h) **(i)** **(j)**

Figure 4.15: Mie series solution versus MoM solution for $\varepsilon_r = 2.0$ and $\sigma = 0.75$ S/m. (a) and (c) indicate the Mie series solution for the magnitude of the electric and magnetic fields on the surface of the sphere, while (b) and (d) show the corresponding MoM solutions. (e), (f) and (g) show the magnitude of the electric field along the x, y and z axes, while (h), (i) and (j) show the corresponding magnetic field. The Mie series solution is shown as solid lines, while the MoM solution is shown as dashed lines. All spatial dimensions are in [m], with the electric and magnetic fields in V/m and T.

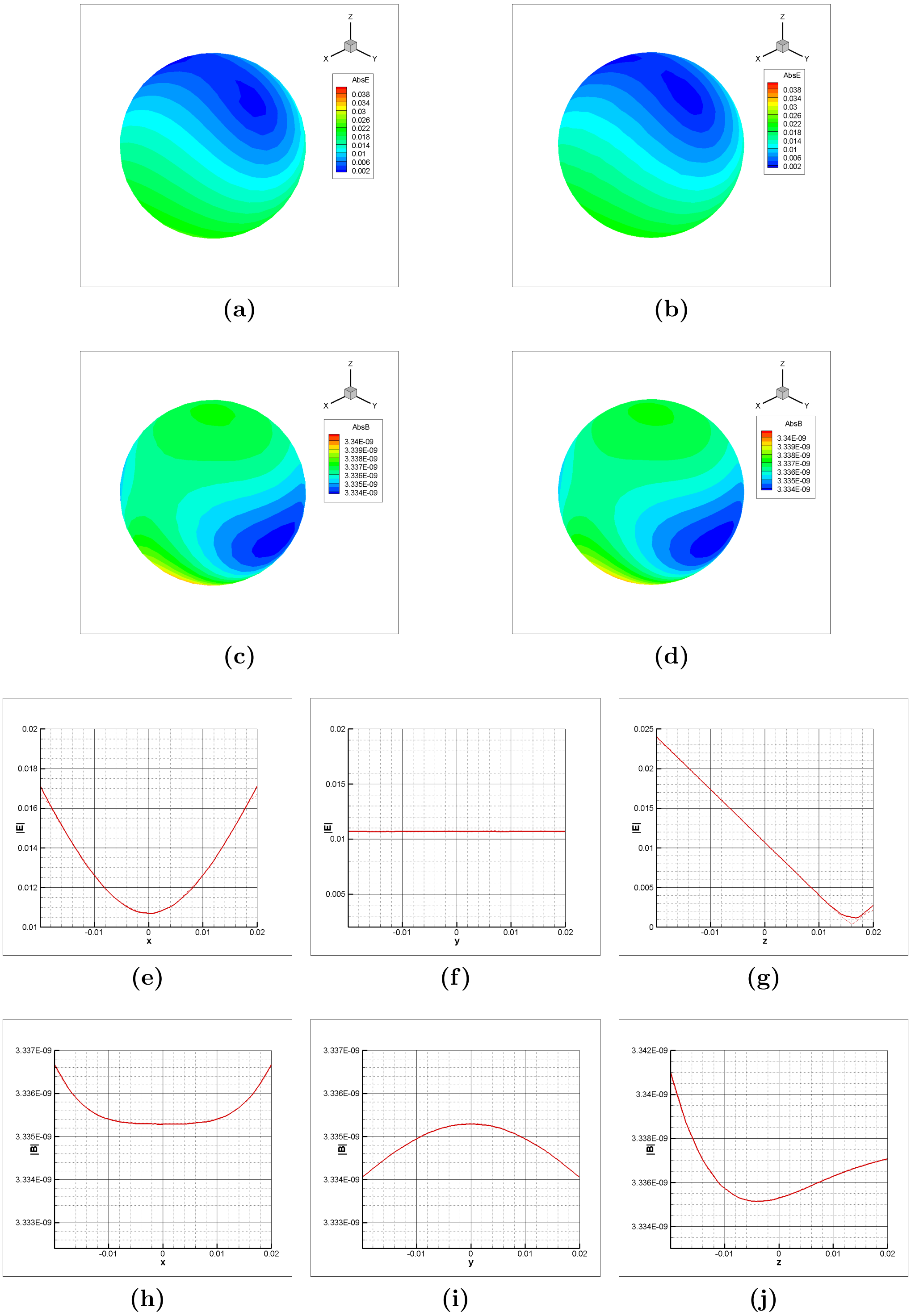

(a) (b) (c) (d) (e) (f) (g) (h) (i) (j)

Figure 4.16: Mie series solution versus MoM solution for $\varepsilon_r = 2.0$ and $\sigma = 1.0$ S/m. (a) and (c) indicate the Mie series solution for the magnitude of the electric and magnetic fields on the surface of the sphere, while (b) and (d) show the corresponding MoM solutions. (e), (f) and (g) show the magnitude of the electric field along the x, y and z axes, while (h), (i) and (j) show the corresponding magnetic field. The Mie series solution is shown as solid lines, while the MoM solution is shown as dashed lines. All spatial dimensions are in [m], with the electric and magnetic fields in V/m and T.

since it contains both surface and volume discretizations. There are no analytical solutions available for this setup, so we will base our validation on deductions about the wave behavior in the dielectric sphere. The model setup is shown in Fig.4.17. The sphere is of radius $r = 0.02$m with a dielectric constant $\varepsilon_r = 2.0$ as in the incident wave scattering model. The conductance of the sphere σ take on values in the list $\sigma = 0.1, 1.0, 10.0, 50.0$S/m. The ring has a radius $r = 0.06$m with a width $w = 0.015$m. After discretization, the volume mesh yielded 6339 tetrahedra with 6777 independent basis edges while the surface mesh gave 1504 triangles and 2066 RWG elements. An excitation voltage of 1V at a frequency of 200.0MHz was applied to the input port of the circular ring. Next, we apply our MoM implementation to obtain solutions for the electric and magnetic fields in the sphere for various values of σ. The results obtained for the electric and magnetic fields are shown in Fig.4.18 through Fig.4.21. From these results, we observe that as σ increases in value, the magnitude of the electric and magnetic fields in the sphere decreases correspondingly. This is the expected behavior since the wave should attenuate due to conduction losses in the sphere. Also, we see that the magnitude of the electric field on the

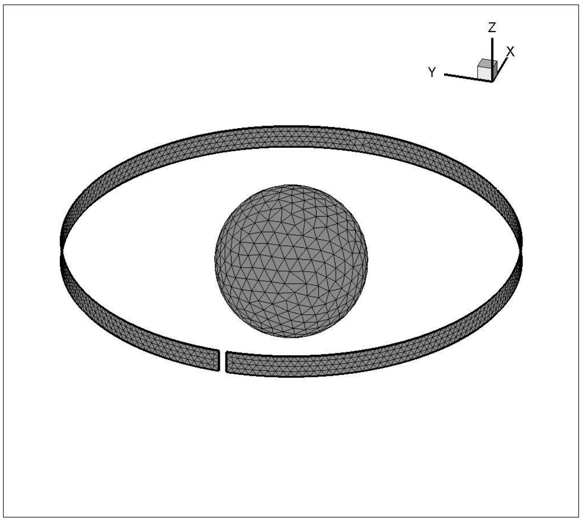

Figure 4.17: Arrangement for modeling scattering by a dielectric sphere. In this case the incident wave emanates from the circular ring.

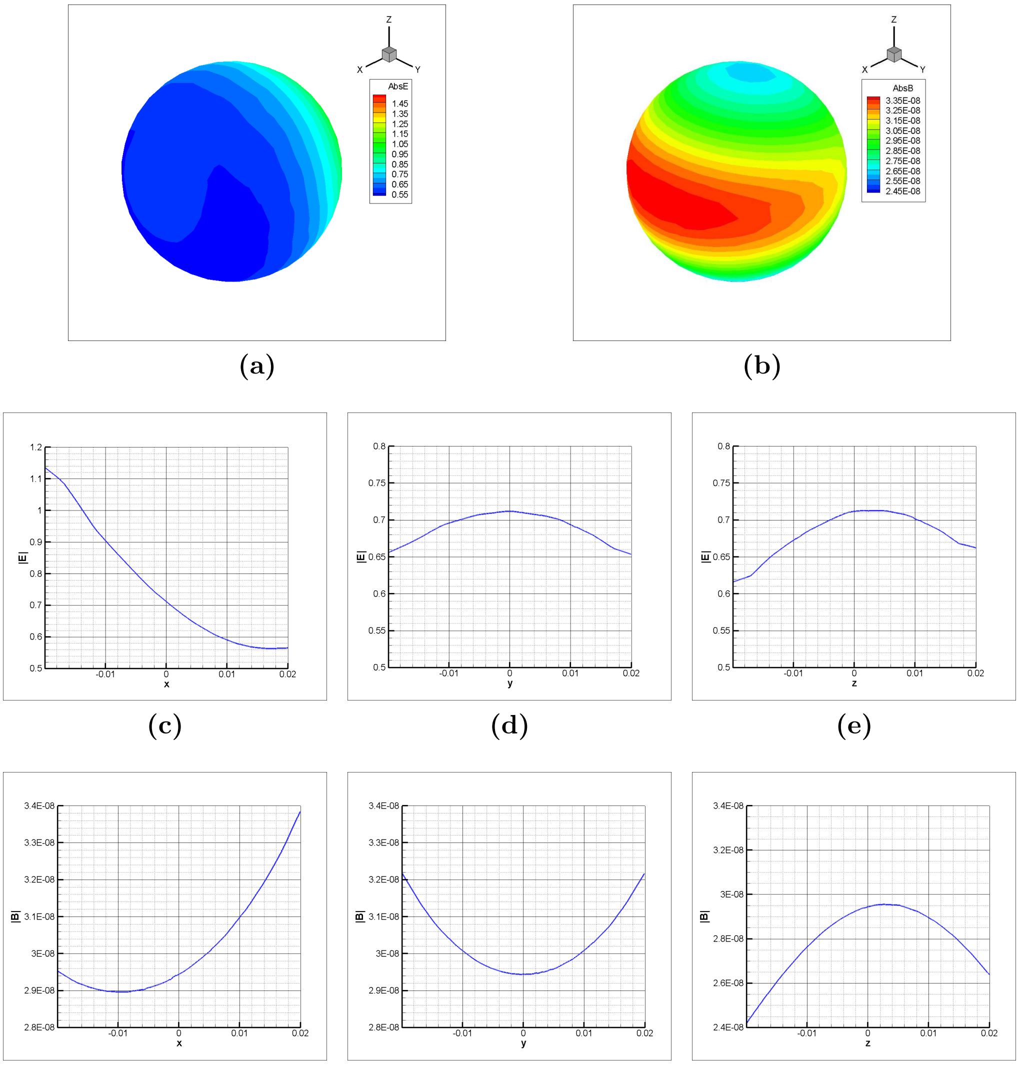

(a) (b)

(c) (d) (e)

(f) (g) (h)

Figure 4.18: Scattering of electromagnetic waves emanating from a circular ring by a dielectric sphere with $\varepsilon_r = 2.0$ and $\sigma = 0.1\text{S/m}$. (a) Magnitude of electric field on the surface of the sphere, (b) magnitude of magnetic field on the surface of the sphere. The magnitude of the electric field is shown along the (c) x, (d) y and (e) z axes. Similarly, the magnitude of the magnetic field is also shown along the (f) x, (g) y and (h) z axes. All spatial dimensions are in [m], with the electric and magnetic fields in V/m and T.

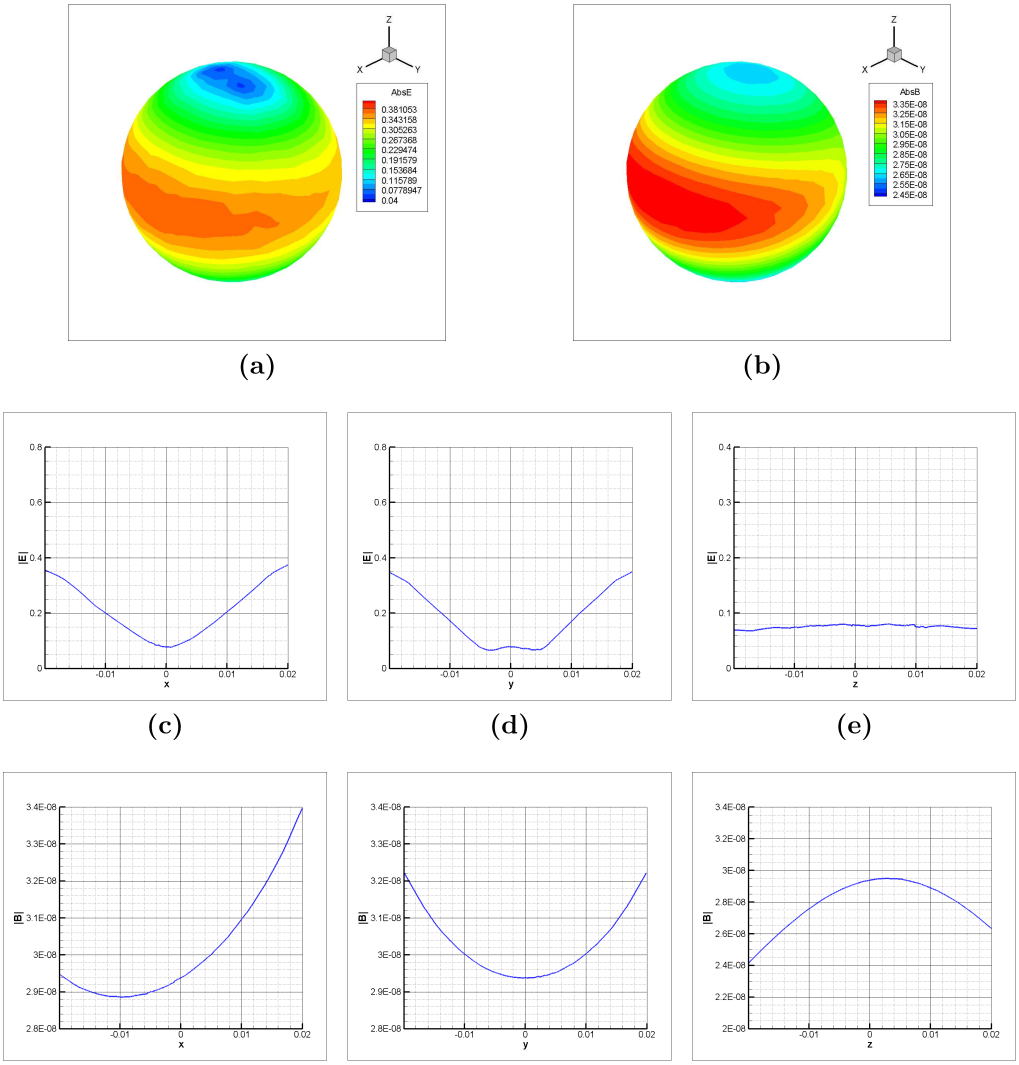
(a) (b)

(c) (d) (e)

(f) (g) (h)

Figure 4.19: Scattering of electromagnetic waves emanating from a circular ring by a dielectric sphere with $\varepsilon_r = 2.0$ and $\sigma = 1.0$S/m. (a) Magnitude of electric field on the surface of the sphere, (b) magnitude of magnetic field on the surface of the sphere. The magnitude of the electric field is shown along the (c) x, (d) y and (e) z axes. Similarly, the magnitude of the magnetic field is also shown along the (f) x, (g) y and (h) z axes. All spatial dimensions are in [m], with the electric and magnetic fields in V/m and T.

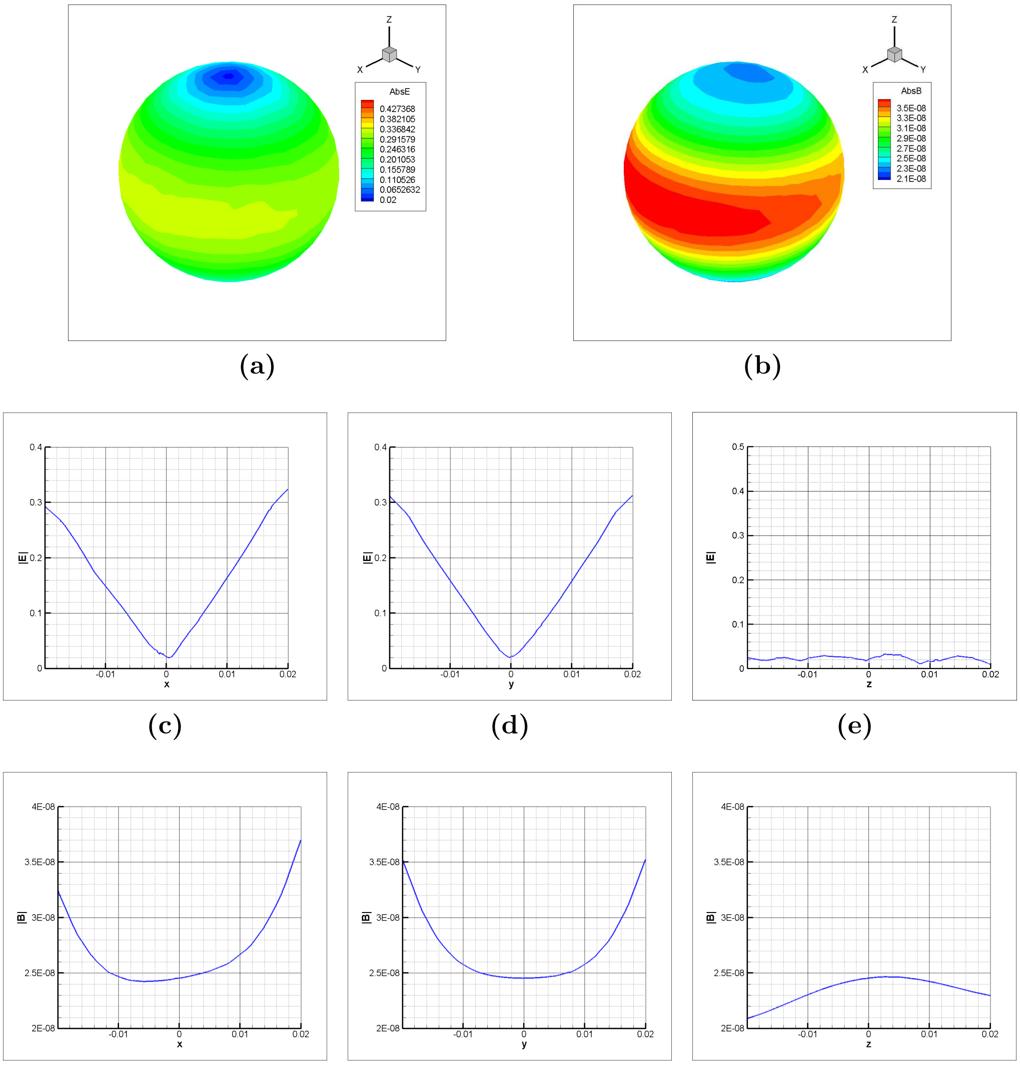

(a) (b)

(c) (d) (e)

(f) (g) (h)

Figure 4.20: Scattering of electromagnetic waves emanating from a circular ring by a dielectric sphere with $\varepsilon_r = 2.0$ and $\sigma = 10.0$S/m. (a) Magnitude of electric field on the surface of the sphere, (b) magnitude of magnetic field on the surface of the sphere. The magnitude of the electric field is shown along the (c) x, (d) y and (e) z axes. Similarly, the magnitude of the magnetic field is also shown along the (f) x, (g) y and (h) z axes. All spatial dimensions are in [m], with the electric and magnetic fields in V/m and T.

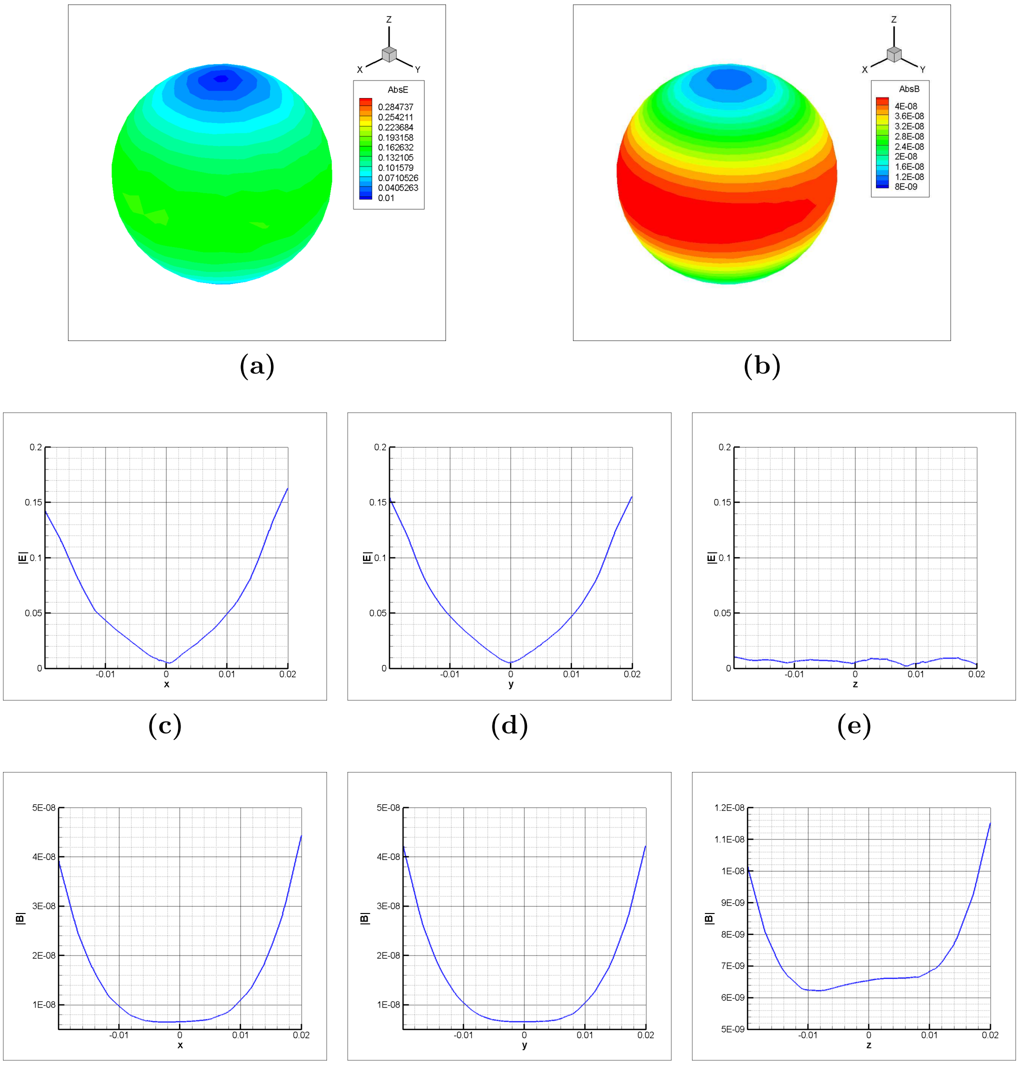

(a) (b)

(c) (d) (e)

(f) (g) (h)

Figure 4.21: Scattering of electromagnetic waves emanating from a circular ring by a dielectric sphere with $\varepsilon_r = 2.0$ and $\sigma = 50.0$S/m. (a) Magnitude of electric field on the surface of the sphere, (b) magnitude of magnetic field on the surface of the sphere. The magnitude of the electric field is shown along the (c) x, (d) y and (e) z axes. Similarly, the magnitude of the magnetic field is also shown along the (f) x, (g) y and (h) z axes. All spatial dimensions are in [m], with the electric and magnetic fields in V/m and T.

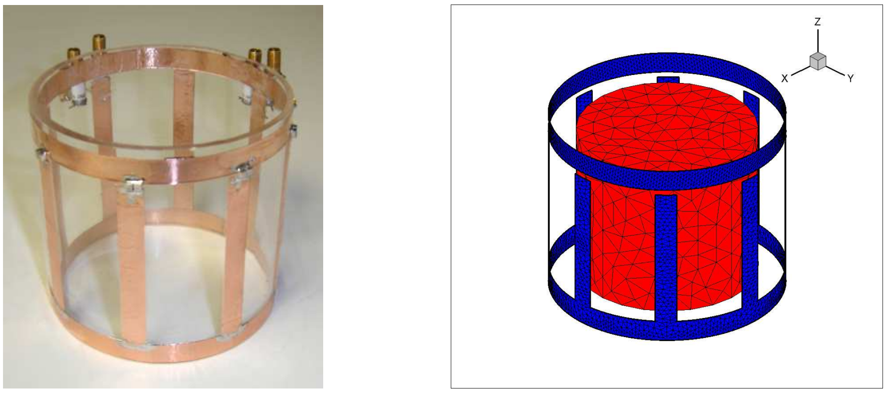

(a) **(b)**

Figure 4.22: Low-pass quadrature birdcage coil: (a) physical prototype, and (b) surface mesh model with volume load mesh.

surface of the sphere decreases as σ increases. Clearly this is because the tangential component of the electric field at the surface tends to zero as the conductance at the boundary increases. In summary, the nature of the electromagnetic wave in the volume of the sphere is very similar to that exhibited by the incident wave scattering model described earlier. This similarity in behavior provides some validity in the implementation of the Surface-Volume MoM integral equation. In the next section, we will improve upon this validity by considering comparisons with actual physical measurements.

4.4.4 RF BirdCage Coil Model

The bird cage RF coil is the most common volume RF coil used in MRI imaging [7]. It finds particular use as an RF transmit coil where it establishes the required uniform magnetic field to excite the sample in the region of interest. In this section, we intend to simulate the frequency response of a loaded low-pass quadrature birdcage RF coil and compare it against actual physical measurements using a network analyzer. For the low-pass quadrature birdcage coil of Fig.4.22(a) [74], a mesh model was generated as shown in Fig.4.22(b) with a diameter of 104mm and a height of 86mm. The mesh model has 8 rungs each of width 9.5mm. The biological load is a simple cylinder of diameter 84mm with electrical properties corresponding to human muscle at 63.6MHz. The birdcage model was discretized into a surface mesh of 6038 triangular elements, while the cylindrical load was discretized into a volume mesh with 3452 tetrahedra. The birdcage model was treated as an 8-port system where each port corresponds to a capacitor location. Two of the 8-ports act as input ports that drive the coil in a quadrature configuration. Our MoM implementation is then used to solve the system at 63.6MHz and determine its scattering matrix $\mathbf{S}$. From the $\mathbf{S}$-matrix, we determined the values of the capacitors needed to achieve resonance at 63.6MHz. The simulated magnetic field of the loaded birdcage coil is shown in Fig.4.23. From Fig.4.23(a) and (b), we observe the highly uniform magnetic field normally associated with the birdcage coil. We also observe the quadrature nature of the magnetic field on the $x-y$ plane. This a consequence of driving the input ports in quadrature. The magnitude of the combined magnetic field along the $x-z$ plane is also shown in Fig.4.23(c). In order to validate our MoM formulation, we built a prototype quadrature birdcage coil with dimensions identical to those of our coil model (see Fig.4.22(a)). We then compared our MoM simulation results of $\mathbf{S}$-matrix parameters (S_{11},S_{21}) with those obtained from actual physical measurements using a network analyzer under loaded conditions. The result of the comparison is depicted in Fig.4.24. Immediately upon

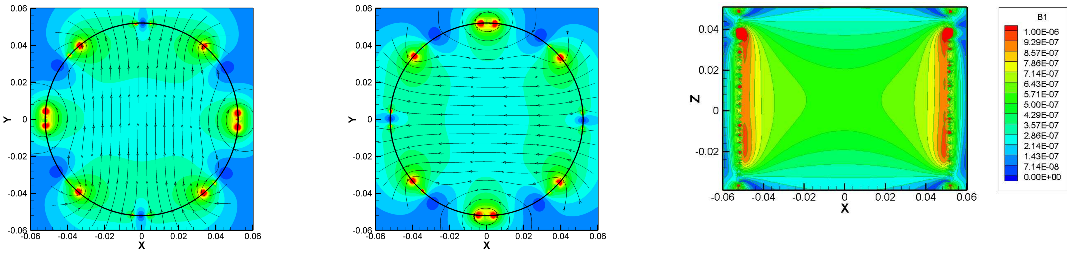

(a) **(b)** **(c)**

Figure 4.23: Magnetic field simulation of a loaded birdcage coil: (a) and (b) are the quadrature fields on the $x-y$ plane, and (c) is the magnitude of the combined fields along the $x-z$ plane.

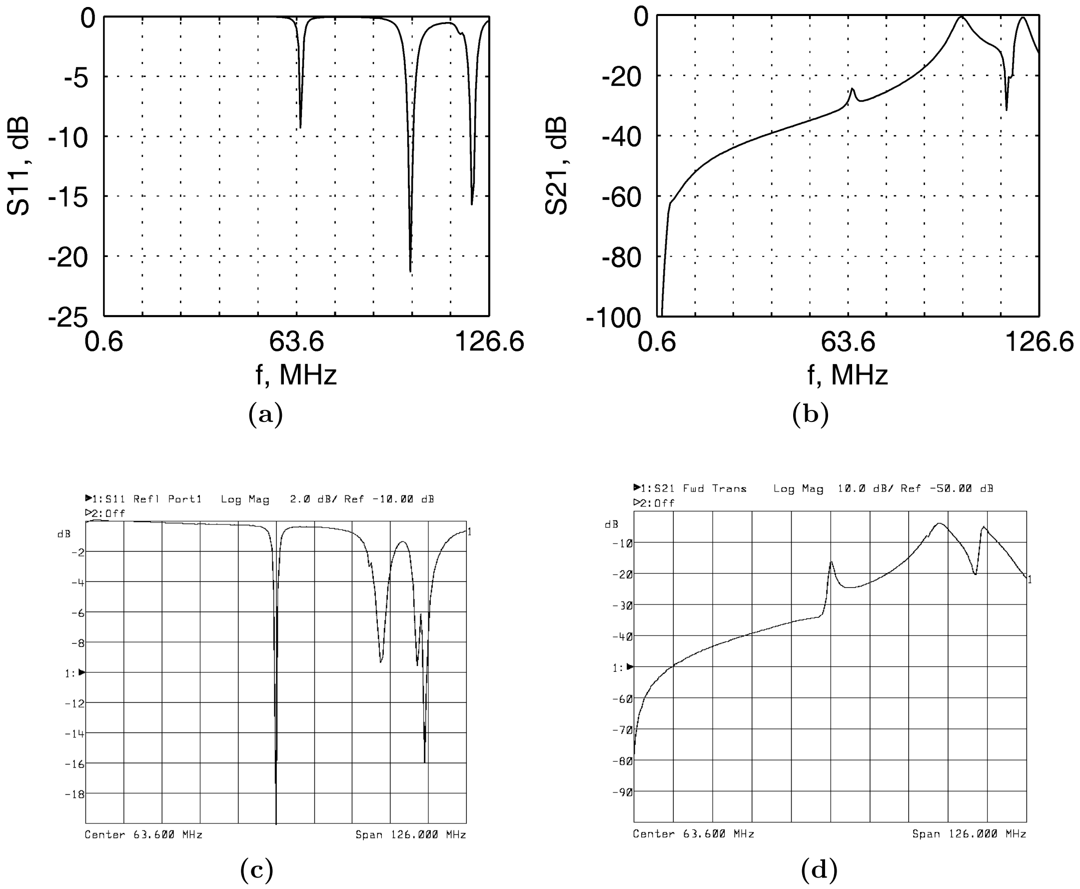

(a) (b)

(c) (d)

Figure 4.24: Simulated and measured **S** parameter plots: (a) simulated S_{11}, (b) simulated S_{21}, (c) measured S_{11} and (d) measured S_{21}.

viewing Fig.4.24, we observe that the profiles of the S_{11} and S_{21} curves are very similar in simulation as well as in actual physical measurements. This undoubtedly provides the necessary validity of our MoM implementation of the Surface-Volume integral equation. In summary, we have demonstrated the ability to efficiently and effectively simulate the frequency response of loaded MRI RF coils using the Method of Moments.

Chapter 5

4-Channel Breast MRI Coil Design

In this chapter, we discuss the development of a 4-channel RF coil for breast imaging in a 1.5T clinical MRI system. The 4-channel breast coil is essentially a localized receive-only RF coil that improves upon the design proposed in [75] in order to facilitate bilateral imaging of the breast. The design methodology was inspired by the multi-channel array concept, where multiple conductive strips are arranged in an anatomically conforming profile with the goal of improving sensitivity and filling factor. The 4-channel RF coil system is made up of two RF coils with each coil providing two independent receive channels. The unique design of the coil system facilitates its operation in a dual-channel configuration since each RF coil provides two resonant modes that can be combined in single-channel quadrature configuration, thus providing a high SNR in conjunction with good $\mathbf{B}_1$ field coverage across the region of interest.

5.1 Design

The 4-channel RF breast coil was developed specifically for screening women with a D cup bra size [76], although it can also be used for screening women with lower sizes. The spatial configuration and geometric orientation of the RF coil closely conforms to the shape of the female breast, thus increasing its sensitivity and filling factor for maximum SNR gains. The symmetric nature of the design guarantees extendability, scalability to various breast sizes, and flexibility of use with existing MRI systems with $\mathbf{B}_0$ field strengths in the range from 0.5T to 3.0T. The design explicitly targeted conventional 1.5T MRI breast screening systems with a corresponding resonance frequency of 63.6MHz.

The basic geometric profile of the 4-channel breast coil is shown in Fig.5.1. The structure features an anatomically correct cup-coil configuration that can be realized using conductive strips. The coil profile of the 4-channel breast coil was realized using the dual-channel configuration of Fig.5.2(a). The unique design of the dual-channel coil configuration has already been shown to possess high SNR in conjunction with good $\mathbf{B}_1$ field coverage [75] and [77]. In effect, we essentially combined two dual-channel coils on a common conductive strip along their flattened base ring member. The base ring member has been flattened to facilitate side access to the breast tissue during biopsy. The is an improvement over the original design proposed in [75] which

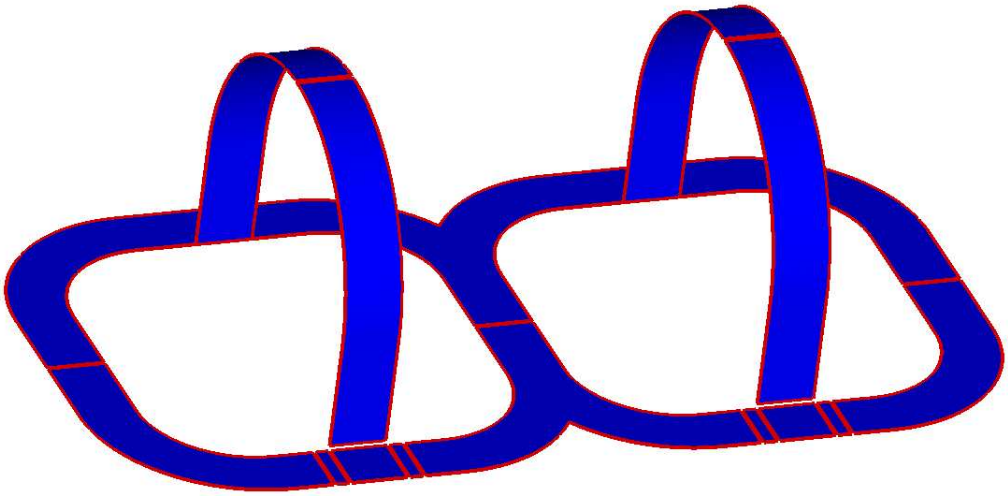

Figure 5.1: Geometric profile of the 4-channel breat coil.

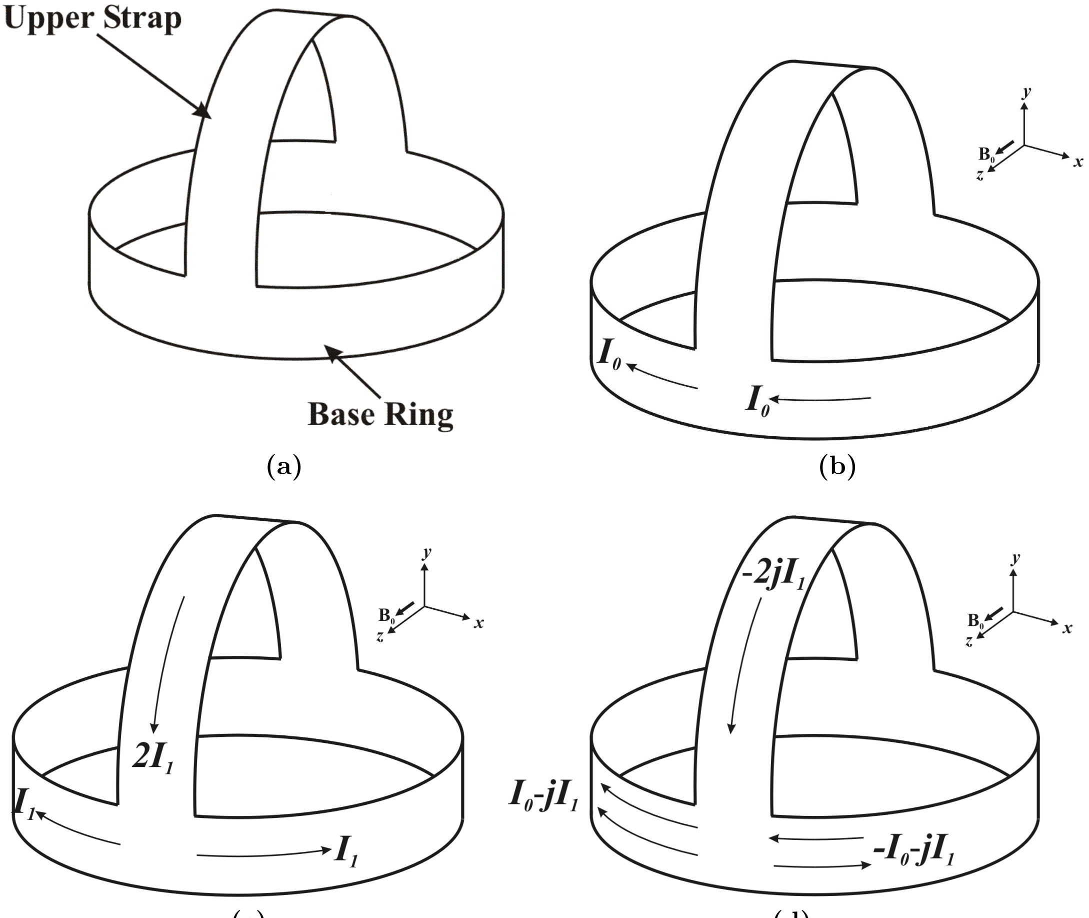

Figure 5.2: Basic dual-channel RF coil configuration [75]: (a) basis structure definition, (b) definition of base ring mode, (c) definition of strap mode and (d) definition of combined mode.

does not allow for easy access to the breast tissue during biopsy. The basic principle of operation of each dual-channel coil can be explained by referring to diagrams in Fig.5.2(b)-(d). Each dual-channel coil possesses a segmented coil profile that offers two basic resonant receiving modes that can be operated in a quadrature configuration. These receiving modes are defined along the current paths described by the base ring member and the strap member as shown in Fig.5.2(b) and Fig.5.2(c). The first resonance mode is termed Mode 0, and it is characterized by induced current flow I_0 only in the base ring member as shown in Fig.5.2(b). On the other hand, the second resonance mode is characterized by induce current flow I_1 in all conducting members, where the magnitude of the induced current in the strap member is twice that in the base ring member as shown in Fig.5.2(c). This resonance mode is termed Mode 1 and it can be combined in quadrature with Mode 0 as shown in Fig.5.2(d). Thus, if four receive channels are not available, the 4-channel breast coil can be operated in a dual-channel configuration.

5.2 Design Considerations

The 4-channel breast coil is a receive-only RF coil that is to be integrated into an existing clinical MRI system. Most clinical MRI systems feature a body resonator coil that generates the required RF transmit pulses. As such, the 4-channel breast coil must be detuned when the body resonator coil is generating the RF transmit pulse. In addition, the impedance of the 4-channel breast coil must be made large enough during transmit in order to suppress the large circulating currents that will be induced in the coil. Another issue of concern is the minimization of coupling between coil members that are more distant neighbors, in this case the strap members of each dual-channel coil. Conventional decoupling techniques such as overlapping of nearest-neighbor coils or reactive decoupling cannot be applied in this case since the coils are not close to one another. These issues constitute some of the most important design considerations in the development of the 4-channel breast coil. In this section, we will discuss the implemented solutions that address these issues.

5.2.1 Passive Detuning

Passive detuning is a simple circuit implementation that utilizes passive electrical components to detune an RF coil and also create the high impedance necessary to reduce circulating current during transmit. A simple passive detune implementation is shown in Fig.5.3. In this circuit implementation, the inductor L and capacitor C are chosen so that they form a parallel resonating circuit at the required RF frequency, in our case 63.6MHz. A pair of back-to-back diodes D_1 and D_2 are connected in series with the inductor L as shown in Fig.5.3. When the transmit RF coil is active, the induced voltages in the receive coil are large enough to easily forward-bias diodes D_1 and D_2. The resulting effect is that L and C will be in parallel resonance at the resonance frequency with an open circuit or high impedance across their terminals. If the circuit in Fig.5.3 is connected in series with the conductive strips of the receiving RF coil, then an open circuit or high impedance state is guaranteed in the receiving RF coil during transmit. Thus, large induced current are effectively suppressed in the receiving RF coil when the transmit RF coil is active. Now when the receiving coil is active, the induced NMR signal are very weak and are not able to forward-bias

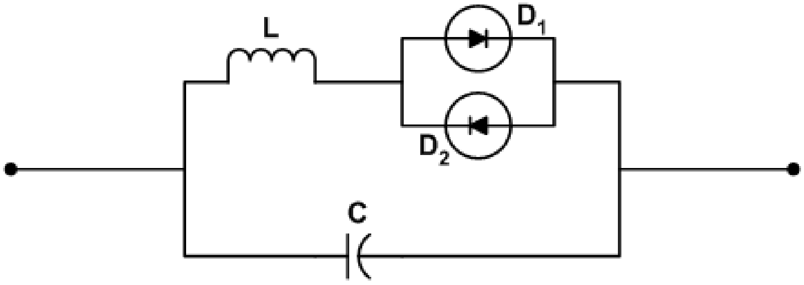

Figure 5.3: Passive detune circuit implementation.

diodes D_1 and D_2. Hence, the inductor L is cut-off from the circuit and the parallel resonance effect is essentially neutralized. In addition, capacitor C is also chosen to resonate with the receiving RF coil, so with L cut-off the resonance of C with the receiving RF coil will be unaffected.

5.2.2 Active Detuning

The active detuning circuit implementation is essentially identical with the passive detuning implementation shown in Fig.5.3 except for the fact that the back-to-back diodes D_1 and D_2 are now replaced by a single pin diode. A pin diode is a special type of semiconductor diode that functions as a current controlled variable resistor at RF frequencies. The pin diode presence a low impedance to an RF circuit when forward-biased with appropriate bias current. [78]. Under the application of a reverse-bias, the pin diode is turned off and exhibits a high impedance. Using this property of the pin diode, the inductor L can be connected or disconnected from the circuit by applying a forward or reverse bias to the pin diode. As discussed previously, when the inductor L is connected to the circuit, it resonates with the capacitor C to form an open circuit or high impedance that effectively suppresses induced RF currents in the receiving coil when the transmit RF coil is active. After transmission, the pin diode is reversed-biased and this disconnects inductor L from the circuit allowing capacitor C to resonate with the receiving RF coil at the NMR signal frequency.

5.2.3 Preamplifier Decoupling

Preamplifier decoupling is a technique that can be used to decouple nearest or more distant coils in an RF coil array. This technique was first reported by [10] who used low input impedance preamplifiers and overlapping of adjacent coils in a coil array to eliminate interference among nearest and more distant neighboring coils. Decoupling becomes important in the design of RF coil arrays because the coupling between coils

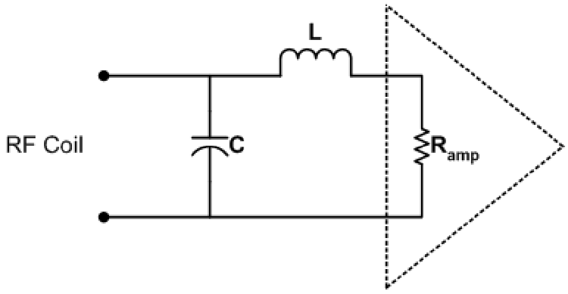

Figure 5.4: Preamplifier decoupling circuit interface [10].

results in a splitting of the resonances which in turn causes a loss in sensitivity at the required resonance frequency [10]. The basic preamplifier decoupling interface is shown in Fig.5.4. This interface connects the input port of the receiving RF coil to the low input impedance preamplifier. From Fig.5.4, we observe that if the input impedance R_{amp} of the preamplifier is ideally zero, the inductor L and the capacitor C form a parallel resonating circuit at the input port of the receiving RF coil. This effectively suppresses the flow of induced currents in the receiving coil as a result of mutual coupling. Furthermore, we would like to point out that suppressing the induced current flow has no effect on NMR signal reception since the preamplifier is a voltage amplification device. In this configuration, all coils in the coil array receive independently because there is very little current flow. This results in no signal coupling between coils. In a practical implementation, the input impedance R_{amp} of the preamplifier is not ideally zero so there exists very minimal coupling between coils. In effect, the lower the input impedance of the preamplifier, the greater the amount of decoupling that can be achieved.

5.3 Coil Simulation

The simulation model used in the determination of the circuit parameters for the 4-channel breast coil is shown in Fig.5.5. The model consists of a 3D surface mesh that describes the conductive surfaces of the 4-channel breast coil and a 3D volume mesh

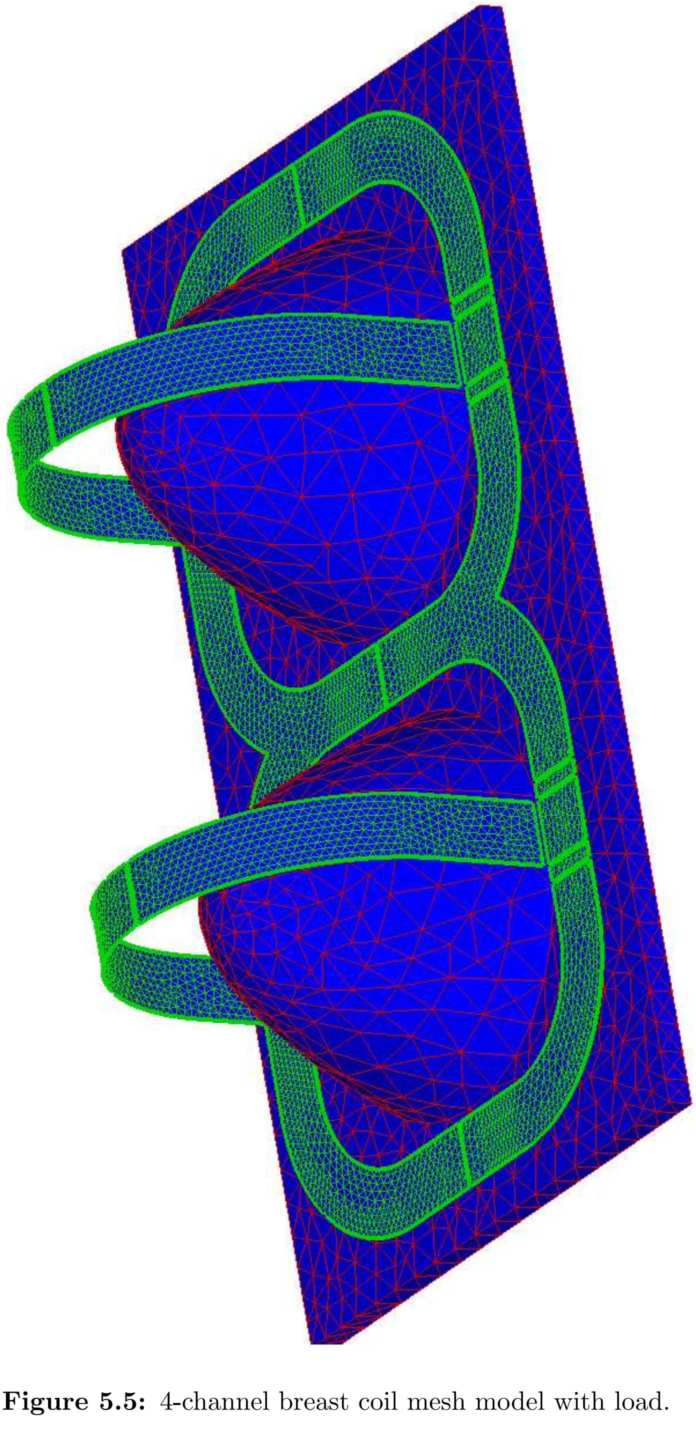

Figure 5.5: 4-channel breast coil mesh model with load.

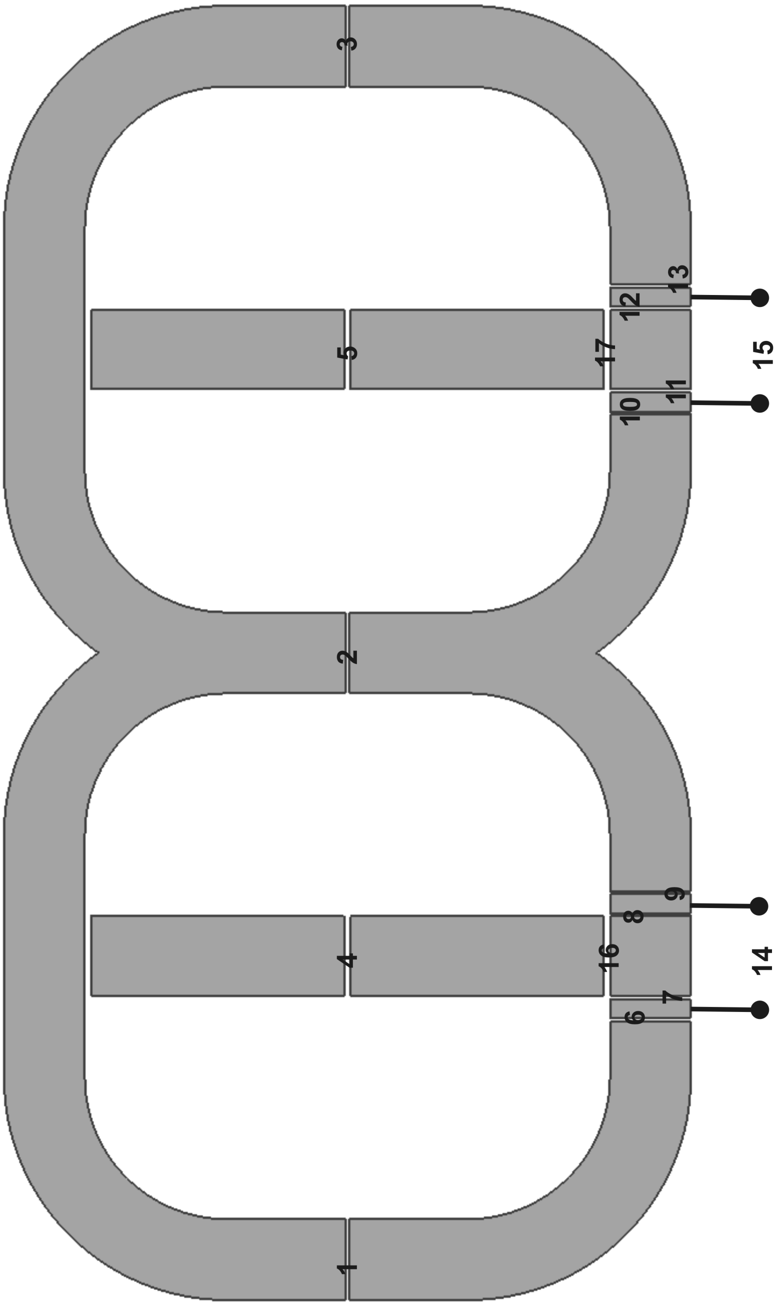

Figure 5.6: Definition of ports used in the determination of the **S** matrix.

that defines an appropriate biological load. The dimensions used in the construction of the 3D surface mesh is given in Fig.A.1 and Fig.A.2. The 3D surface mesh resulted in 5495 nodes with 9618 triangles that yielded 13774 RWG elements. Similarly, the volume mesh encompassed 2555 nodes, 13326 edges and 8692 tetrahedra that resulted in 10774 independent basis edges. The dielectric properties of the biological load was chosen to be identical to those of breast fat at 63.6MHz [79, 80]. This is deemed a good approximation since the breast is mainly made up of fat. The 63.6MHz frequency corresponds to the center frequency at 1.5T of a clinical Siemens MRI system. The surface resistivity of the conductive surface of the coil was chosen to that of copper at 63.6MHz. A total of 17 excitation ports were defined along the conductive surface of the coil. Only 4 of these ports are truly voltage excitation ports, the remainder will define position along the coil surface where capacitive elements will be located. It is essential to define these locations as ports so that we can determine the required capacitive values from the resulting **S** matrix, in this case the initial 17×17 **S** matrix will eventually be reduced to a 4×4 **S** matrix using (4.23). The 17 excitation ports were defined as shown in Fig.5.6. With this definition, we setup our MoM simulation to determine the **S** matrix of the coil model. This was done using the definition of the **S** matrix as presented in (4.2). We arbitrarily chose one port as the excitation port while all other ports are terminated in matched loads of 50Ω. A voltage of 1V at a frequency of 63.6MHz is applied across the excitation port in series with a 50 Ω impedance and the resulting model is simulated using our implementation of the MoM. This process is repeated until all ports have been excited in turn on an arbitrary basis with all other ports terminated by match loads. From the results of the MoM simulations, we constructed the required 17×17 **S** matrix using (4.4) and (4.7). Once the **S** matrix is constructed, it becomes a template for the determination of all required coil capacitances. The main coil capacitances are shown in the simplified circuit schematic of Fig.5.7. We have the main decoupling capacitor C_2 that decouples

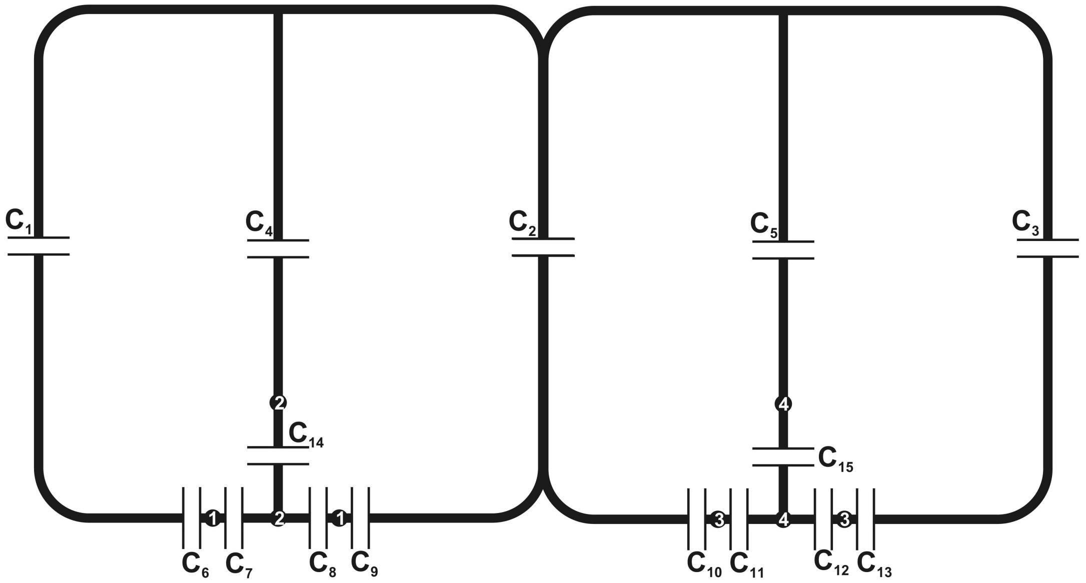

Figure 5.7: A simplified circuit schematic of the 4-channel breast coil. The 4 channels or receiving ports are labeled as 1–1, 2–2, 3–3 and 4–4. The base ring channels are identified as 1–1 and 3–3 while the strap channels are denoted by 2–2 and 4–4.

the 2 base ring channels. In addition, capacitors C_1 and C_3 are used to ensure that the base ring channels are well balanced and properly decoupled from the strap channels. They should have the same capacitance as the decoupling capacitor C_2 to ensure a proper balance. Furthermore, capacitors C_4 and C_5 are the tuning capacitors of the strap channels while capacitors C_6, C_9, C_{10} and C_{13} are used to tune the base ring channels respectively. Similarly, capacitors C_{14} and C_{15} are the matching capacitors of the strap channels while C_8, C_9, C_{11} and C_{12} serve as matching capacitors for the base ring channels. In order to determine the decoupling capacitor C_2, we reduced the original 17×17 **S** matrix into a 3×3 **S** matrix by terminating ports 1, 3, 6, 9, 10 and 13 by a short circuit, and ports 4, 5, 7, 8, 11, 12, 16 and 17 by an open circuit. The only remaining ports are 2 and the base ring channels at port 10 and 15 respectively. Next, we terminate port 2 by a varying capacitance while observing the transmission coefficient between ports 10 and 15. A graph of the transmission coefficient between port 10 and 15 versus the capacitance at port 2 is shown in Fig.5.8. The value of the capacitance at port 2 that minimizes the transmission coefficient

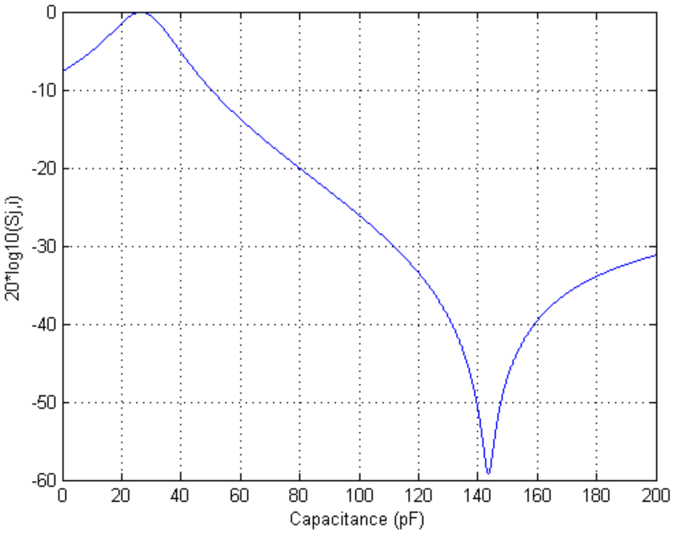

Figure 5.8: Transmission coefficient of the base ring channels versus terminating capacitance.

between port 10 and 15 is the required decoupling capacitance. From Fig.5.8, this value was determined to be 143.56pF and it resulted in a transmission coefficient of -59.2156dB. We now replaced the short circuits at port 1 and 3 with this value of capacitance and observed no changes in the decoupling. With capacitors C_1, C_2 and C_3 defined, we proceed to determine the tuning and matching capacitors of the base ring channels. We terminated the base ring channel at port 15 by an open circuit and determine the impedance looking in at port 10. After the impedance is determined, we use the formulas presented in [10] to determine the tuning and matching capacitors C_6, C_9, C_7 and C_8 as 51.82pF, 51.82pF, 322.9pF and 322.9pF respectively. Because of symmetry capacitors C_{10}, C_{13}, C_{11} and C_{12} were chosen to be of the same capacitances as capacitors C_6, C_9, C_7 and C_8, in the same order. Similarly, we terminate all channels by open circuits, except the strap channel defined at port 16. The impedance looking into port 16 was then determined, and with the help of the formulas in [10], we found the required tuning and matching capacitance C_4 and C_{14} of the strap channel to be 35.75pF and 290.5pF. The other strap channel will have similar values of capacitance because of symmetry. With these values of external components, we determined the $\mathbf{B}_1$ field distribution of the 4-channel breast coil as shown in Fig.5.9. The result shows ample $\mathbf{B}_1$ field coverage in the ROI. Also, the surface current distribution for the strap and ring modes are shown in Fig.5.10 and Fig.5.11, with the streamlines indicating the direction of current flow. This is consistent with the definition of current flow as depicted in Fig.5.2(b) and Fig.5.2(c). Next, we consider the determination of the resistive and reactive components at all 17 ports, in order to model the frequency response of the RF coil. These can be found from the original **S** matrix using procedures described in [68]. Afterwards, we vary these components with frequency in the original **S** matrix, while terminating all ports with their respective capacitances. This reduces the **S** matrix into a 4×4 matrix. The corresponding frequency sweep of the resulting **S** matrix elements is shown in Fig.5.12. This procedure is only an approximation of the **S** parameter sweep. However, it works especially at frequencies in the 3dB bandwidth as demonstrated in [74]. Furthermore, this techniques provides significant savings in computation time required to perform an actual sweep of frequencies.

5.4 Coil Construction

The 4-channel RF breast coil will be housed in a mechanical holder to provide patient comfort and support during the imaging process. The physical dimensions of the mechanical holder is shown in the CAD model of Fig.A.3. The CAD model was designed as a template for the machining of the mechanical holder using a Computer Numerical Control (CNC) machine. The model was created using the commercially available CAD package SolidWorks® design suite. We chose to machine the holder out of cast acrylic since cast acrylic is relatively inexpensive and durable with very good electrical insulating properties at relatively moderate frequencies. It is also shatter resistant and very easy to fabricate on a CNC machine.

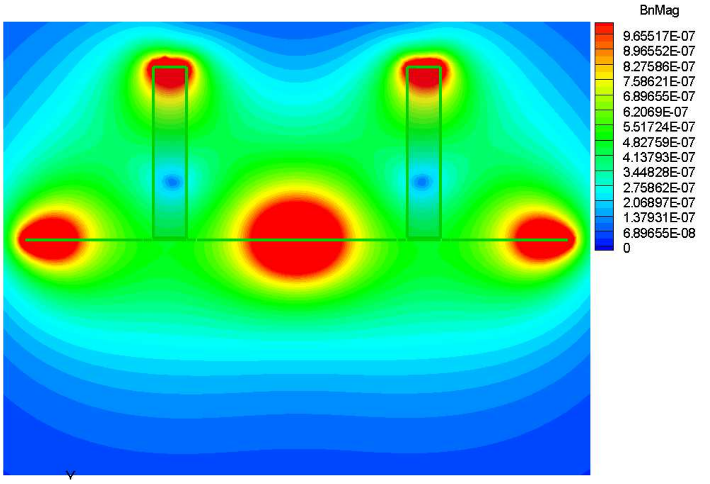

(a) Axial view

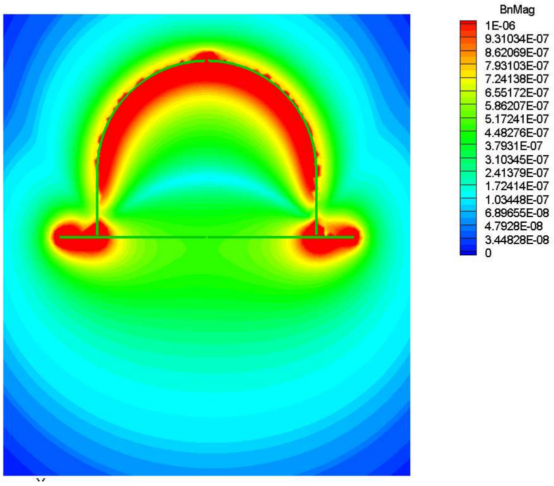

(b) Sagittal view

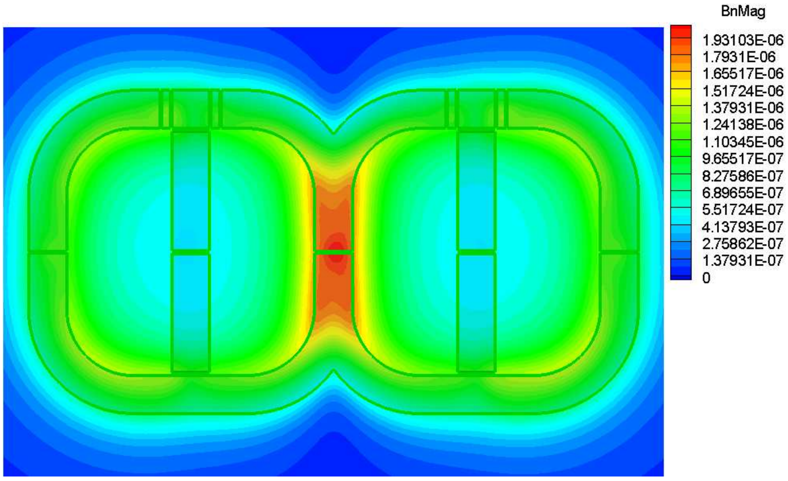

(c) Coronal view

Figure 5.9: $\mathbf{B}_1$ field distribution of the 4-channel breast coil: (a) axial view, (b) sagittal view, and (c) coronal view. The $\mathbf{B}_1$ field is measured in Tesla.

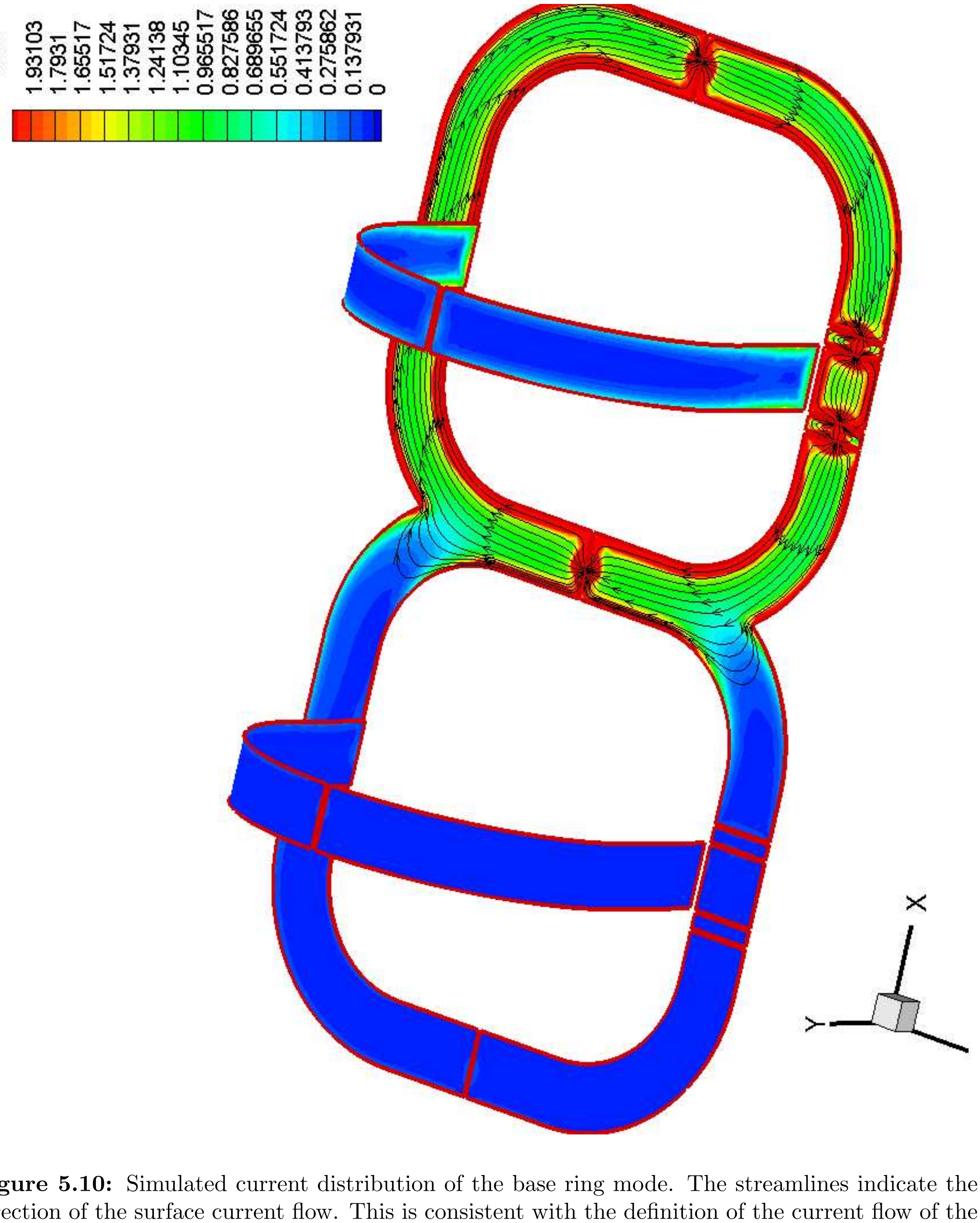

Figure 5.10: Simulated current distribution of the base ring mode. The streamlines indicate the direction of the surface current flow. This is consistent with the definition of the current flow of the base ring mode as shown in as depicted in Fig.5.2(b)

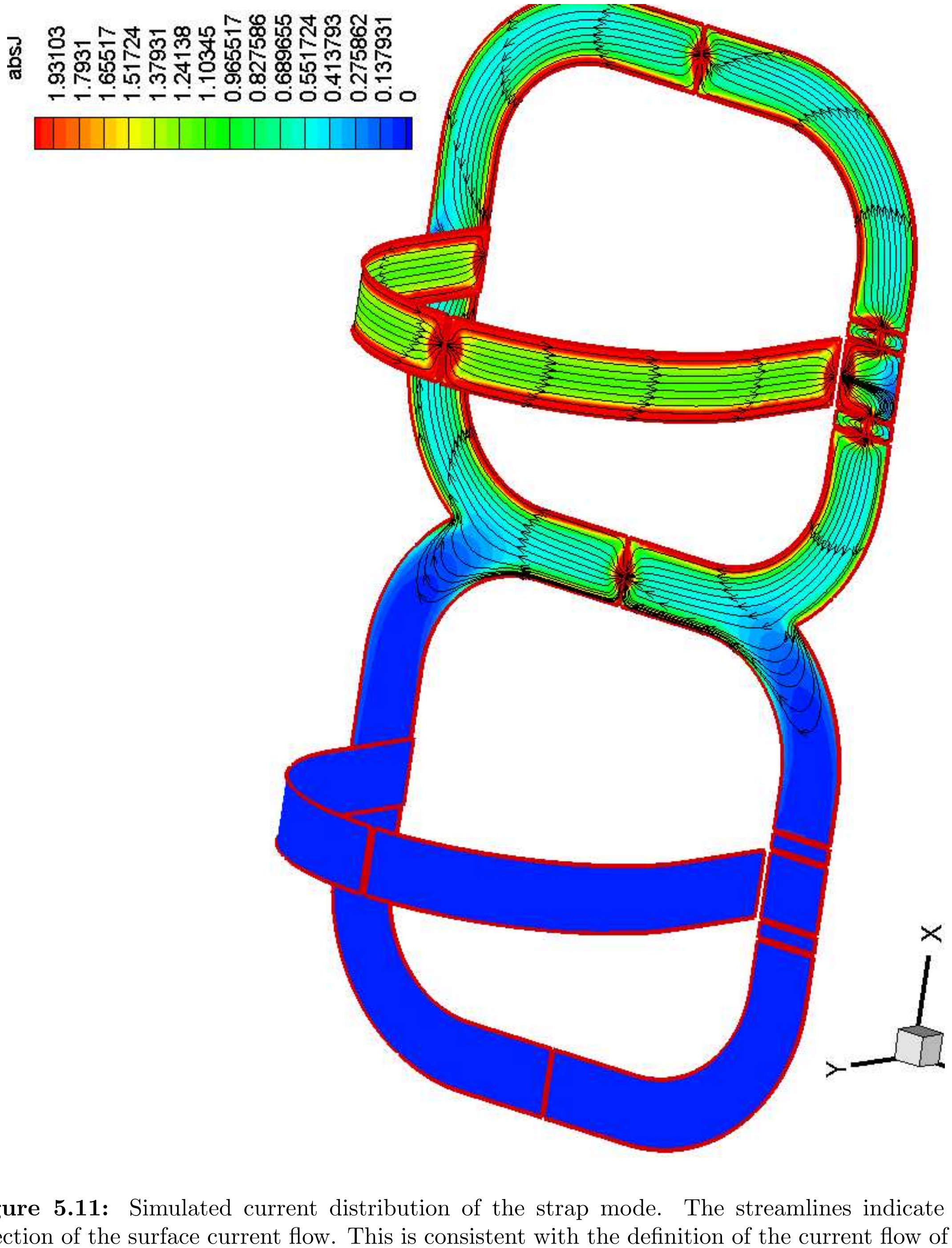

Figure 5.11: Simulated current distribution of the strap mode. The streamlines indicate the direction of the surface current flow. This is consistent with the definition of the current flow of the base ring mode as shown in as depicted in Fig.5.2(c)

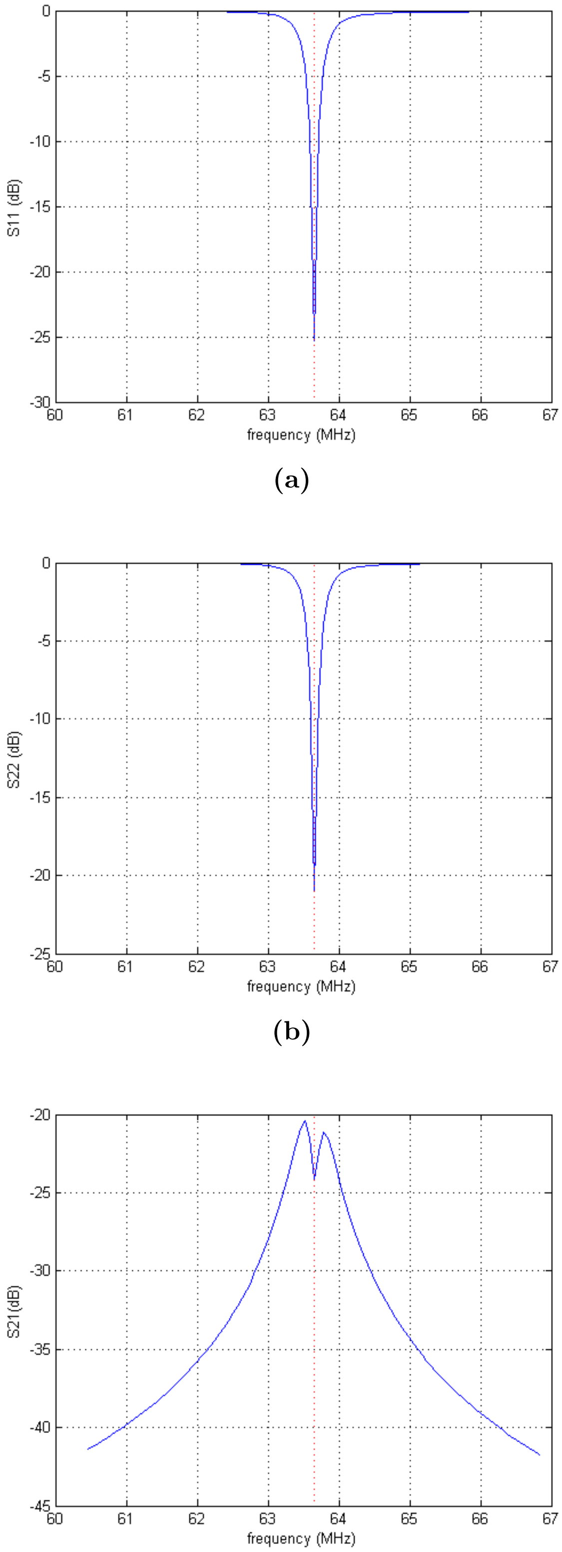

(a)

(b)

(c)

Figure 5.12: Simulated **S** parameter frequency sweeps: (a) S_{11} sweep, (b) S_{22} sweep and (c) S_{21} sweep.

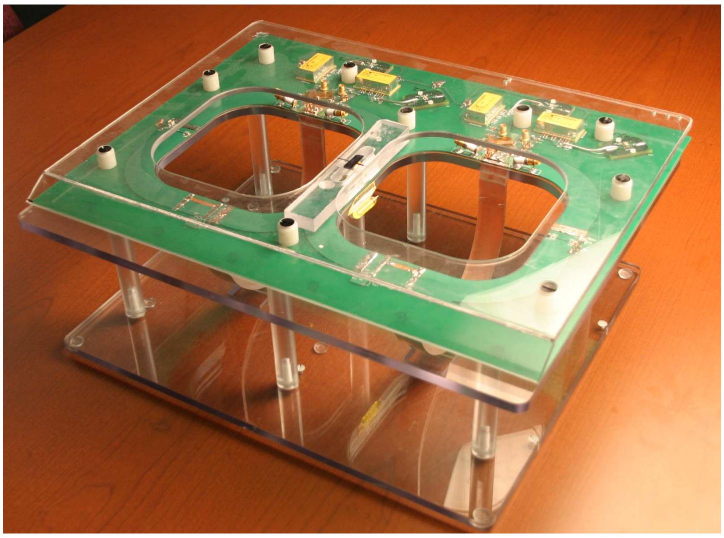

Figure 5.13: Photograph of the completed 4-channel RF breast coil prototype.

After the machining and assembly of the mechanical holder, adhesive copper tapes were placed on the external surfaces of the strap members of the holder to form the strap channel conductors. The dimensions of the strap member of the mechanical holder is shown in Fig.A.1. The copper tape was segmented by a tiny gap of 2mm between segments where the tuning capacitors of the strap channels would be soldered. Also, this would serve as the location of the passive detune circuit components of the strap channels. The thickness of the copper tape was 38μm which is sufficient to allow RF propagation and impede lower frequency eddy currents caused by switching gradient fields. The dimensions and circuit schematic of the base ring channels and associated circuit components are shown in Fig.A.2 and Fig.A.4. All circuit components are non-magnetic since the coil will be placed in a strong magnetic field of strength 1.5T. The schematic was used in the construction of the printed circuit board (PCB) shown in Fig.A.5. The PCB was eventually populated and fastened to the mechanical holder using plastic screws. Finally, the ends of the strap channel conductors were soldered on the PCB to complete the fabrication of the 4-channel breast coil. The photograph of the completed prototype can be seen in Fig.5.13. A detailed listing of circuit components is available in Appendix B.

5.5 Bench Measurements

After completing construction on the prototype coil, we must tune and match the loaded coil before it can be used in an MRI scanner. Before proceeding, we must verify all connections on the PCB and ensure that they are as specified in the circuit schematics. Also, we must ensure that all circuit components are fully functional and are operating as specified. After the verification process, the coil is loaded and connected to a network analyzer for tuning and matching analysis. The base ring channels must be tuned and matched before any of the strap channels. This is essential and greatly simplifies tuning and matching of the strap channels, because the strap channels share the same capacitors used in tuning and matching the base ring channels. Tuning and matching involves adjusting the tuning and matching capacitors until there is a dip in the reflection coefficient at the resonance frequency for the specified port channel, while the coil is loaded with a human subject. Once the base ring channels have been tuned and matched to the load, we proceed to tune and match the strap channels. Essentially, we followed the same steps in tuning and matching the base ring channels until we observed the dip in reflection coefficient at the resonance frequency of 63.6MHz. During the tuning and matching process, we captured some screen shots of the **S** parameter sweeps from the network analyzer. The measured response is shown in Fig.5.14. We observe that the isolation between the base ring and strap channel can be adjusted to fall between -18 and -35dB, depending on the load conditions. This indicates that there is adequate decoupling between the base ring and strap channels. Also, we observed that the percentage bandwidth of the prototype coil seem to vary between 3.0% and 5.1% depending on the loading conditions. In addition, we can see that the simulated response of Fig.5.12 compares very well with the measured response from the network analyzer. This is viewed as further validation of our MoM simulations of RF coils. Finally, we would like to note that although we were able to accurately predict the tuning capacitors of the base


Tr1 S11 Log Mag 5.000dB/ Ref -25.00dB
Tr2 S22 Log Mag 5.000dB/ Ref -25.00dB
Tr3 S21 Log Mag 5.000dB/ Ref -25.00dB

1 Center 63.6 MHz IFBW 30 kHz Span 20 MHz

2007-12-28 11:03

(a)

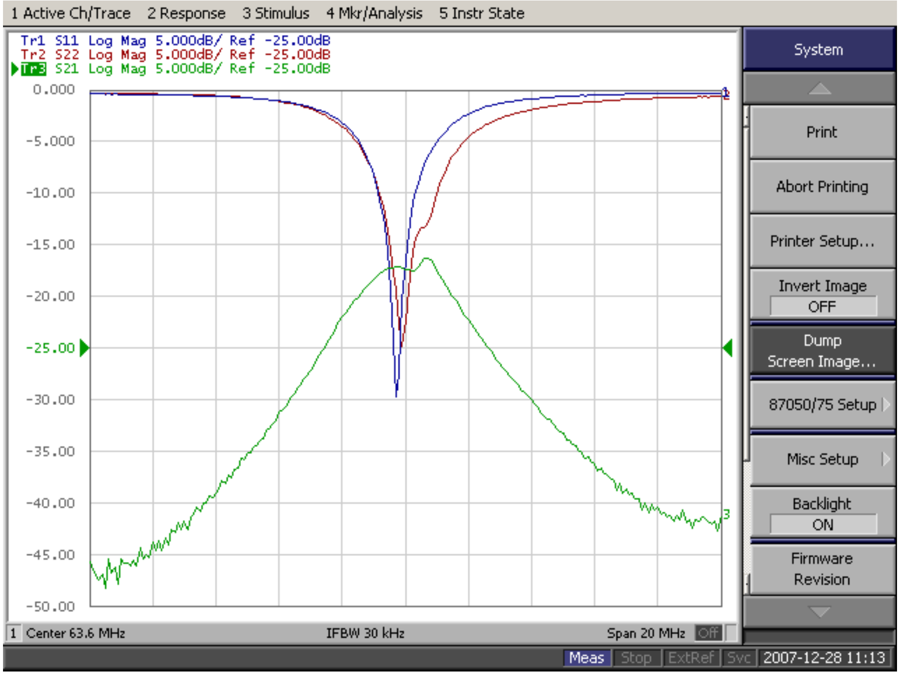
Tr1 S11 Log Mag 5.000dB/ Ref -25.00dB
Tr2 S22 Log Mag 5.000dB/ Ref -25.00dB
Tr3 S21 Log Mag 5.000dB/ Ref -25.00dB

1 Center 63.6 MHz IFBW 30 kHz Span 20 MHz

2007-12-28 11:13

(b)

Figure 5.14: Measured **S** parameter frequency sweeps: (a) **S** parameter sweeps for channel 1 and 2, and (b) **S** parameter sweeps for channel 3 and 4.

ring channels as well as the decoupling capacitors between these channels, there were differences between simulated and actual matching capacitors of the base ring channels as well as both tuning and matching capacitors of the strap channels. For the base ring channels, we predicted matching capacitance of 322.9pF but we deployed only 200pF for matching in the actual prototype. Furthermore, because the tuning and matching capacitors of the base ring channels are shared by the strap channels, we expect similar discrepancies in both tuning and matching capacitance for the strap channels. For the strap channels, we predicted tuning and matching capacitances of 35.75pF and 290.5pF but we deployed 58pF and 161pF in the prototype. The discrepancy between simulated and actual capacitances is attributable to the fact that we used a very simple human breast fat model for our MoM simulations. As such, the resistances at the receiving ports used in the calculation of matching capacitors [10] will be less than in the actual loaded prototype, since losses in our breast fat model are smaller than losses in an actual human breast.

5.6 Imaging

All image acquisitions were performed on a clinical 1.5T Siemens MRI system. For preliminary imaging, a simple water based phantom was utilized. Water based phantoms are considered to be heavy loads for most MRI RF coils because of the high conductance of water compared to most body tissues [80]. The imaging protocol used for the acquisition of the phantom dataset is given in Table.5.1. The goal of preliminary imaging is to determine the image uniformity and signal-to-noise ratio (SNR) of the RF coil under load conditions. We employed two different methods to measure the image SNR from the phantom dataset. These methods are referred to as the NEMA MS 1 and NEMA MS 6 standards; they are part of a series of test standards specifically developed by the medical diagnostic imaging industry as part of the National

Table 5.1: Imaging protocol used for the acquisition of the phantom dataset.

Parameter	**Dimension**
Pixel bandwidth (Hz/pixel)	260
Voxel dimensions (mm)	1.5625 × 1.5625
Slice thickness (mm)	2
Sequence repetition time, TR (ms)	100
Echo delay time, TE (ms)	10
Number of signal averaged (NSA)	1
Data acquisition matrix size	256 × 256
Field of view (mm)	400 × 400

Electrical Manufacturers Association (NEMA) for the determination of performance parameters governing the quality of images from clinical MRI systems [81]. These test procedures are normally carried out using the standard clinical operating modes of the MRI system. Standard clinical operating modes include standard calibration routines, standard clinical sequences and standard reconstruction procedures. The major advantage of the first method is that it allows for the use of standard clinical scanning procedures in the evaluation of SNR performance. The main drawback to this method is that it can be very sensitive to system instabilities during image acquisition. As such, the alternative method has been designed to be less vulnerable to system instabilities. Next, we determine the image SNR using the first method as outlined in the NEMA MS 1 standard [81] for the data acquired from the imaging phantom as shown in Fig.5.15(a). The measurement region of interest (MROI) for

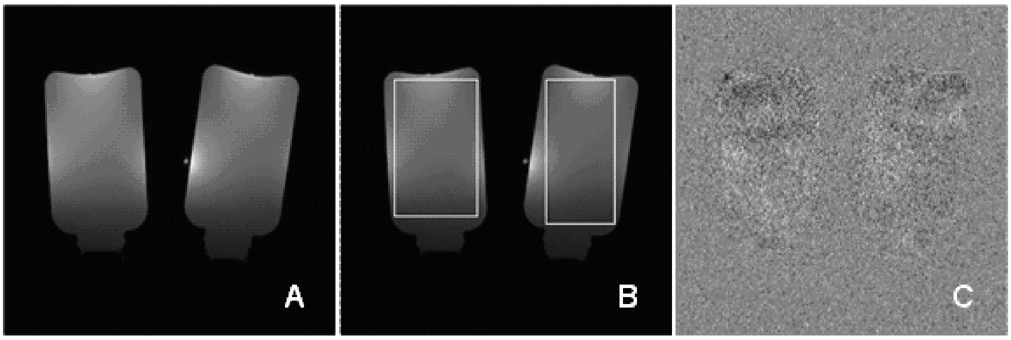

Figure 5.15: MROIs used for NEMA MS 1 SNR measurement for the 4-channel breast coil: (a) image obtained using coil, (b) MROIs, and (c) subtraction image.

the phantom dataset encloses a $10.0 \times 16.6\text{cm}^2$ area for the right phantom and a $8.3 \times 17.5\text{cm}^2$ area for the left phantom. These MROI are as shown in Fig.5.15(b). The SNR in the MROI was determined according to the NEMA MS 1 standard as follows:

- Determine the mean pixel value (S) within MROI.
- Create the subtraction image (Fig.5.15(c)) and allow for negative values.
- Calculate the standard deviations σ_1 and σ_2 using the two equations specified in NEMA MS 1 for the first method.
- Calculate the image noise, $\eta = \sigma/\sqrt{2}$ for each standard deviation.
- Determine the SNR as S/η for each standard deviation and compare.

The SNR measurements for the phantom dataset are shown in Table.5.2. The results from Table.5.2 indicate SNR values ranging from 175.2 to 201.5. These values are much higher, about 7 to 9 times higher than those obtained from commercially available clinical 4-channel MRI RF coils [75]. We now continue with SNR measurements on the phantom dataset using the second method as outlined in the NEMA MS 6 standard. We defined two MROIs for each phantom image which enclosed a 7×7 pixel area ($10.94 \times 10.94\text{mm}^2$) and an 11×11 pixel area ($17.9 \times 17.9\text{mm}^2$) centered at the reference positions. The MROIs for the phantom dataset are shown in Fig.5.16.

Table 5.2: SNR measurements using the NEMA MS 1 standard.

Measurements	**Right Phantom**	**Left Phantom**
S	1109.1	1025.4
σ_1	7.8	7.4
σ_2	9.0	8.1
η_1	5.5	5.2
η_2	6.3	5.8
SNR_1	201.5	195.7
SNR_2	175.2	178.3

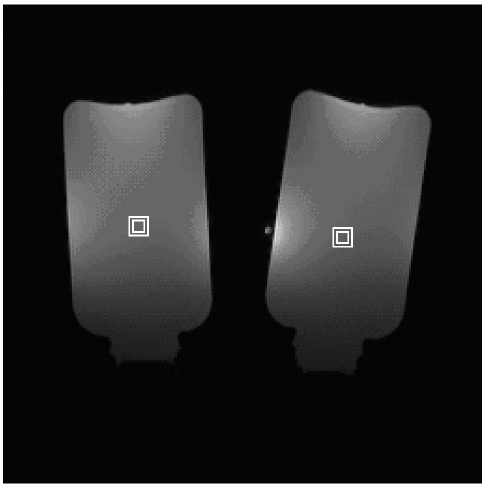

Figure 5.16: MROIs used for NEMA MS 6 SNR measurement for the 4-channel breast coil.

The SNR was determined for the MROIs of Fig.5.16 according to the NEMA MS 6 standard as follows:

- Determine the mean pixel value (S) within MROI.
- Create the subtraction image.
- Calculate the standard deviations σ_1 within the MROI of the subtracted image.
- Calculate the preliminary image noise estimate, $P = \sigma_1/\sqrt{2}$.
- Define the noise evaluation area and calculate the standard deviation σ_2 within this area.
- Determine the SNR as $S * \sqrt{2}/\sigma_2$

Table 5.3: SNR measurements using the NEMA MS 6 standard.

Measurements	**Right Phantom**	**Left Phantom**
S	1157.7	1071.6
σ_1	6.1	6.8
P	4.3	4.8
σ_2	8.5	7.1
SNR	192.5	213.7

The SNR measurement results from the NEMA MS 6 standard is shown in Table.5.3. SNR values for the phantom dataset were 192.5 for the right phantom and 213.7 for the left phantom respectively. These results compare well with those in Table.5.2. These SNR measurements clearly indicate superior performance of the 4-channel breast coil when compared with other commercially available 4-channel MRI RF coils.

Next, we consider the determination of image uniformity using the 4-channel breast coil prototype. In this case, the image uniformity was measured using the method outlined in the NEMA MS 3 standard for the phantom dataset. The image was pre-processed by a 2D convolution with a nine point low-pass filter as specified in NEMA MS 3, §2.3.1. The MROI for the phantom dataset encloses a $10.0 \times 16.6\text{cm}^2$ area for the right phantom and an $8.3 \times 17.5\text{cm}^2$ area for the left phantom. The MROIs for the dataset are shown in Fig.5.15(b). The peak deviation uniformity measure was determined for the MROIs according to the NEMA MS 3 standard as follows:

- Determine the maximum and minimum pixel values (S_{max}, S_{min}) within the MROIs specified.
- Calculate $\delta = (S_{max} - S_{min})/2$.
- Calculate $S = (S_{max} + S_{min})/2$.
- Determine the peak deviation uniformity measure, $N = 100 * \delta/S$.

The measured peak deviation uniformity (N) for the coil was found to be 69.6 and 72.0 for the right and left phantoms respectively, as shown in Table.5.4. The results

Table 5.4: Image uniformity calculations using NEMA MS 3.

Measurements	**Right Phantom**	**Left Phantom**
S_{min}	301.0	271.5
S_{max}	1681.1	1669.0
δ	690.1	698.8
S	991.1	970.3
N	69.6	72.0

obtained from SNR measurements and measured peak deviation uniformity of the 4-channel breast coil loaded with a water base phantom indicate that the distinctive anatomical design offers superior SNR as well as good $\mathbf{B}_1$ field uniformity and coverage across the region of interest. The distinctive anatomically conforming profile of the 4-channel breast coil is protected under US patent 7,084,630.

Finally, we consider human clinical imaging with the 4-channel breast coil. We obtained the Institutional Review Board (IRB) approval from Massachusetts General Hospital in Boston, MA, and an informed written consent from our human patient in order to proceed with limited human imaging experiments. Single accumulation high resolution T_1 weighted images of the human subject were acquired with acquisition parameters TR=450ms, TE=14ms, 256×256 matrix, 40cm FOV and a slice thickness of 2mm. An axial view of one such high resolution image is shown in Fig.5.17.

In summary, we have presented an MoM implementation that is very suitable for the development of MRI RF coils. We applied our formulation in the design of a 4-channel receive-only MRI RF coil for breast imaging at 1.5T. The coil profile closely conformed to the shape of the female breast, and thus demonstrated improved sensitivity and filling factor.

Figure 5.17: An axial view of a high resolution T_1 image of the human breast.

Chapter 6

Conclusion

6.1 Summary

In this dissertation, we presented a unique approach to the modeling of loaded MRI RF coils using the Method of Moments. The method combined a surface integral formulation with a volume integral formulation in order to qualitatively describe the interaction between biological tissues and the electromagnetic fields produced by MRI RF coils. Our approach is based on formulating an electromagnetic scattering problem and providing a solution of the electric field in terms of the current density. As such, two distinct basis function definitions were developed in an effort to describe the surface current density on the RF coil, and the sum of the volume current density and the displacement current density in the inhomogeneous biological tissue. We discussed the development of the modified RWG basis function, and the use of the impedance concept to account for conduction losses in the MRI RF coil. In addition, we showed that the total current density in an inhomogeneous material volume is strictly divergence-free, and can be conveniently represented using the low-order solenoidal basis function. The use of this low-order solenoidal basis function necessitated the development of a unique algorithm for identifying the linearly independent basis functions in the solenoidal basis set. The novel algorithm utilized a non-algebraic approach that is dependent only on the properties of the solenoidal basis function, thus providing substantial savings in computational resources. The combined MoM based formulations were developed into a multi-threaded software implementation on a massively parallel computer system and validated against several analytical models as well as measurements from actual physical prototypes. The results showed good agreement and help establish the validity of our modeling technique.

To demonstrate a practical design implementation from concept to prototype construction, a 4-channel receive-only RF coil was developed for clinical breast imaging at 1.5T. The coil featured two resonant receiving modes that can operate in quadrature, and an anatomically conforming profile for improved sensitivity and filling factor. In addition, the coil structure was designed around an open breast coil concept in order to facilitate MRI-guided biopsy and patient comfort. From simulations of the loaded 4-channel RF coil, we were able to accurately determine its frequency response as well as optimum values of tuning, matching and decoupling capacitors. Imaging tests were conducted on a pair of phantoms as well as on a human patient after obtaining the proper authorization. The tests indicated that the 4-channel RF coil achieved good field uniformity and high SNR in the region of interest. Furthermore, performance comparisons with existing clinical 4-channel RF breast coils indicate superior SNR in conjunction with good $\mathbf{B}_1$ field homogeneity over the entire region of interest.

6.2 Further Research

Based on problems encountered during the development and implementation of this work, recommendations for further research should be directed towards:

- The development of a more accurate MoM resistance models for the conductors of the RF coil. Currently, the impedance concept was used to account for losses in the coil, but this model introduces small errors when used to create an SNR map in the region of interest.

- Simulations of complex biological tissues in the development of RF transmit coils. Our current MoM formulation is capable of simulating the interactions between electromagnetic fields and complex biological tissues, but such simulations do not radically affect the performance and safety of MRI RF receiver coils. As such, further investigations into tissue-field interactions as well as in the creation of more realistic models is warranted as part of the development of RF transmit coils.

- Development of specialized anatomically shaped MRI RF coils for localized imaging of other regions of the human body. We have shown that anatomically shaped coils offer improved SNR as well as good field uniformity in the region of interest. This principle can be applied in the development of localized coils for other regions of the body.

- Investigation of the optimum strip width that maximizes SNR for a specific configuration of the MRI RF coil. The strip width of the conductors used in the design of RF coils influences the SNR in the region of interest. Too large a strip width implies more signal but also more noise from switching gradients.

Bibliography

[1] S. K. Moore. Better Breast Cancer Detection, Medical Imaging Series. *IEEE Spectrum*, page 50, May 2002.

[2] A. Howseman et al. Improvements of Snap-shot Nuclear Magnetic Resonance Imaging. *The British Journal of Radiology*, 61(729):822–828, July 1988.

[3] R. J. Ordidge et al. Snapshot Imaging at 0.5t Using Echo-Planar Techniques. *Magnetic Resonance in Medicine*, 10:227–240, May 1989.

[4] R. E. Wysong et al. Cardiac imaging using biplanar gradient at 4.0 tesla. *Proceedings of the Society of Magnetic Resonance and the European Society for Magnetic Resonance in Medicine and Biology*, page 956, August 1995.

[5] P. J. Keller. Basic Principles of Magnetic Resonance Imaging. *GE Medical System*, June 1988.

[6] J. Jin. *Electromagnetic Analysis and Design in Magnetic Resonance Imaging.* CRC press LLC, Florida, 1999.

[7] C. E. Hayes et al. An Efficient Highly Homogeneous Radio Frequency Coil for Whole-Body NMR Imaging at 1.5 T. *Journ. Magn. Resn.*, 62:622–628, 1985.

[8] J.T. Vaughan, H.P. Hetherington, J.O. Out, J.W. Pan, and G.M. Pohost. High Frequency Volume Coils for Clinical NMR Imaging and Spectroscopy. *Magn. Resn. Med.*, 32:206–218, 1994.

[9] Gene Bogdanov. Radio-frequency coil design for high field magnetic resonance imaging. Phd, Worcester Polytechnic Institute, April 2002.

[10] P. Roemer et al. The NMR Phased Array. *Magn. Resn. in Med.*, 16:192–225, 1990.

[11] W. T. Soblo. Dedicated Coils in Magnetic Resonance Imaging. *Reviews of Magnetic Resonance in Medicine*, 1(2):181–224, 1986.

[12] R. Pascone, T. Vullo, J. Farrelly, and P.T. Cahill. Explicit Treatment of Mutual Inductance in Eight-Column Birdcage Resonators. *Magn. Resn. Imag.*, 10:401–410, 1992.

[13] M.D. Harpen. Equivalent Circuit for Birdcage Resonators. *Magn. Resn. Med.*, 29:263–268, 1993.

[14] C.L. Leifer. Resonant Modes of the Birdcage Coil. *Journal of Magnetic Resonance*, 124:50–60, 1997.

[15] J. Tropp. Mutual Inductance in the Birdcage Resonator. *Journal of Magnetic Resonance*, 126:9–17, 1997.

[16] Johnson J. H. Wang. *Generalized Moment Methods in Electromagnetics*. John Wiley & Sons, 1991.

[17] J. Chen, Z. Feng, and J.M. Jin. Numerical Simulation of SAR and $\mathbf{B}_1$-Field Inhomogeneity of Shielded RF Coils Loaded with the Human Head. *IEEE Trans. Bio. Eng.*, 45(5):650–659, 1998.

[18] O.P. Gandhi and X.B. Chen. Specific Absorption Rates and Induced Current Densities for an Anatomy-Based Model of the Human for Exposure to Time-Varying Magnetic Fields of MRI. *Magn. Resn. Med.*, 41:816–823, 1999.

[19] C.M. Collins and M.B. Smith. Signal-to-Noise Ratio and Absorbed Power as Functions of Main Magnetic Field Strength, and Definition of 90° RF Pulse for the Head in the Birdcage Coil. *Magn. resn. Med.*, 45:684–691, 2001.

[20] D. Simunic, P. Wach, W. Renhart, and R. Stollberger. Spatial Distribution of High-Frequency Electromagnetic Energy in Human Head During MRI: Numerical Results and Measurements. *IEEE Trans. Bio. Eng.*, 43:88–94, 1996.

[21] C. Guclu, G. Kashmar, A. Hacinliyan, and O. Nalcioglu. An FEM Approach for the Characterization of the RF Field Homogeneity at High Field. *Magn. Resn. Med.*, 37:76–83, 1997.

[22] S. Wang and J. H. Duyn. Analyzing Radio-Frequency Coil Arrays in High-Field Magnetic Resonance Imaging by the Combined Field Integral Equation Method. *Phys. Med. Biol.*, 51:3211–3229, June 2006.

[23] F.-H. Lin ; W.-P. Kuan, S.-K. Jeng, and J.-H. Chen. Quantitative Spectral/Spatial Analysis of Phased Array Coil in Magnetic Resonance Imaging Based on Method of Moment. *IEEE Trans. Med. Imaging*, 18(12):1129–1137, December 1999.

[24] J.-H. Chen, S.-K. Jeng, F.-H. Lin, and W.-P. Kuan. Quantitative Analysis of Magnetic Resonance Radio-Frequency Coils Based on Method of Moments. *IEEE Trans. Magn.*, 35(3):2118–2127, May 1999.

[25] D Jiao and J Jin. Fast Frequency-Sweep Analysis of RF Coils for MRI. *IEEE Trans. Bio. Eng.*, 46(11):1387–1390, Nov 1999.

[26] F. Liu, B. Beck, B. Xu, J. Fitzsimmons, S. Blackband and S. Crozier. Numerical Modeling of 11.1T MRI of a Human Head using a MoM/FDTD Method. *Concepts in Magn. Resn. Part B*, 24B(1):28–38, 2005.

[27] M. W. Ali, T. H. Hubing, and J. L. Drewniak. A Hybrid FEM/MoM Technique for Electromagnetic Scattering and Radiation from Dielectric Objects with Attached Wires. *IEEE Trans. Elect. Compat.*, 39(4):304–313, November 1997.

[28] D. H. Schaubert D. R. Wilton and A. W. Glisson. A Tetrahedral Modeling Method for Electromagnetic Scattering by Arbitrarily Shaped Inhomogeneous Dielectric Bodies. *IEEE Trans. Ant. & Prop.*, AP-32:77–85, Jan 1984.

[29] A. W. Glisson S. M. Rao, D. R. Wilton. Electromagnetic Scattering by Surfaces of Arbitrary Shapes. *IEEE Trans. Ant. & Prop.*, 30(3):409–418, May 1982.

[30] L. de Souza Mendes S. A. de Carvalho. Scattering of EM Waves by Inhomogeneous Dielectric with the use of the Method of Moments and the 3D Solenoidal Basis Function. *Micro. & Opt. Tech. Letters*, 23(1):42–46, Oct. 1999.

[31] F. Lui et al. A Theoretical Comparison of Two Optimization Methods for RF Drive Schemes in High Frequency Mri Resonators. *Phys. Med. Biol.*, pages 5281–5291, Oct. 2005.

[32] R. Lemdiasov, A. Obi, R. Ludwig. Time Domain Formulation of the Method of Moments for Inhomogeneous Conductive Bodies at Low Frequencies. *IEEE Trans. Ant. & Prop.*, 54(2):706–714, Feb. 2006.

[33] Constantine A. Balanis. *Advance Engineering Electromagnetics*. John Wiley & Sons, Hoboken, NJ 07030, 1989.

[34] N. A. Demerdash et al. Three Dimensional Finite Element Vector Potential Formulation of Magnetic Fields in Electrical Apparatus. *IEEE Trans. PAS.*, 100(8), March 1981.

[35] O. Biro et al. On the Use of the Magnetic Vector Potential in the Finite Element Analysis of 3-Dimensional Eddy Current. *IEEE Trans. Magn.*, 25(4), July 1989.

[36] D. R. Corson P. Lorrain. *Electromagnetism, Principles and Applications*. W H Freeman and Company, 2^{nd} edition, 1997.

[37] D. M. Drury. The Unification of the Lorentz and Coulomb Gauges of Electromagnetic Theory. *IEEE Trans, Edu.*, 43(1), Feb. 2000.

[38] S. Kulkarni et al. Mom Volume Integral Equation Solution for an Isolated Metal-Dielectric Resonator with the Edge-Based Basis Function. *IEEE Trans. Ant. & Prop.*, 53(4):1566, April 2005.

[39] R. Lemdiasov, R. Ludwig. The Determination of Linearly Independent Rotational Basis Function in Volumetric Electric Field Integral Equations. *IEEE Trans. Ant. & Prop.*, 54(7):2166, July 2006.

[40] L. Yaxun et al. Comparison of SIE-MoM and VIE-MoM for determination of complex resonant frequency of dielectric resonators. *IEEE Ant. & Prop. Int. Symp.*, 1:641–644, June 2003.

[41] T. K. Sarkaret al. Electromagnetic Scattering and Radiation from Finite Microstrip Structures. *IEEE Trans. Micro. Theory Tech.*, 38:1568–1575, Nov 1990.

[42] R. F. Harrington. *Field Computation by Moment Methods.* Macmillian, 1968.

[43] M. Davidovitz and Y.T. Lo. Rigorous Analysis of a Circular Patch Antenna excited by a Microstrip Transmission Line. *IEEE Trans. Ant. & Prop.*, 37(8):949–958, 1989.

[44] A. A Kishk G. P Junker and A. W Glisson. A Novel Delta Gap Source Model for Center Fed Cylindrical Dipoles. *IEEE Trans. Ant. & Prop.*, 43:537–540, May 1995.

[45] M.B Dragovic B.D Popovic and A.R. Djordjevic. *Analysis and Synthesis of Wire Antenna.* John Wiley & Sons Inc., 1982.

[46] S. N Makarov. *Antenna and EM Modeling with MATLAB.* Wiley, 2002.

[47] M. G Duffy. Quadrature over a Pyramid or Cube of Integrands with a Singularity at a Vertex. *SIAM J. Numer. Anal.*, 19:1260–1262, December 1982.

[48] L. Rossi and P. J Cullen. On the Fully Numerical Evaluation of the Linear-Shape Function Times the 3-D Green's Function on a Plane Triangle. *IEEE Trans. Micro. Theory & Tech.*, 47(4):398–402, April 1999.

[49] D. Moreno S. Caorsi and F. Sidoti. Theoretical and Numerical Treatment of Surface Integrals involving the Free-Space Green's Function. *IEEE Trans. Ant. & Prop.*, 41(9):1296–1301, September 1993.

[50] P Yla-Oijala and M askinen. Calculation of CFIE Impedance Matrix Elements With RWG and $n\times$ RWG Functions. *IEEE Trans. Ant. & Prop.*, 51(8):1837–1845, August 2003.

[51] A Tzoulis and F Eibert. Review of Singular Potential Integrals for Method of Moments Solutions of Surface Integral Equations. *Advances in Radio Science*, 2(93):93–99, 2004.

[52] M Taskinen S Jarvenpaa and P Yla-Oijala. Singularity extraction techinque for integral equation methods with higher order basis functions on plane triangles and tetrahedra. *Int. J. Numer. Meth. Enging*, 58:1149–1165, November 2003.

[53] R Graglia. On the numerical integration of the linear shape function times the 3-d Green's function or its gradient on a plane triangle. *IEEE Trans. Ant. & Prop.*, 41(10):14481455, October 1993.

[54] D. Wilton et al. Potential integrals for uniform and linear source distributions on polygonal and polyhedral domains. *IEEE Trans. Ant. & Prop.*, 32(3):276–281, March 1984.

[55] R Graglia. Static and dynamic potential integrals for linearly varying source distributions in two- and three-dimensional problems. *IEEE Trans. Ant. & Prop.*, 35(6):662–669, 1987 1987.

[56] T Eibert and V Hansen. On the calculation of potential integrals for linear source distributions on triangular domains. *IEEE Trans. Ant. & Prop.*, 43(12):1499–1502, December 1995.

[57] R. Cools. An Encyclopedia of Cubature Formulae. *J. Complexity*, 19:445–453, 2003.

[58] D. Livesay and Kun-mu Chen. Electromagnetic Fields Induced Inside Arbitrarily Shaped Biological Bodies. *IEEE Trans. On Micro. Theory & Techn.*, 22(12):1273–1280, December 1974.

[59] R. L. Rivest T. H. Cormen, C. E. Leiserson. *Introduction to Algorithms*. MIT Press, Cambridge, MA, 1990.

[60] A. S. Tanenbaum. *Structured Computer Organization*. Prentice-Hall Inc., New Jersey, 4th edition, 1999.

[61] H. Deitel and P. Deitel. *C How to Program*. Prentice Hall, 5th edition, August 2006.

[62] Microsoft Windows Operating System.
`http://www.microsoft.com`.

[63] SGi Altix and SGi ProPack.
`http://www.sgi.com`.

[64] OpenGL Graphics Library.
`http://www.opengl.org`.

[65] B. Lewis and D. J. Berg. *Threads Primer: A Guide to Multithreaded Programming*. Prentice Hall, 1st edition, October 1995.

[66] Intel Math Kernel Library.
`http://www.intel.com`.

[67] Tecplot Visualization Software.
`http://www.tecplot.com`.

[68] David M. Pozar. *Microwave Engineering*. John Wiley & Sons Inc., 2nd edition, 1998.

[69] R. Ludwig and P. Bretchko. *RF Circuit Design and Applications*. Prentice Hall, NJ, 2000.

[70] Frederick W. Grover. *Inductance Calculations, working formulae and tables*. Dover Publications, Mineola, NY, 1945.

[71] B. Niceno. *Easymesh: A Two-Dimensional Quality Mesh Generator*. http://www-dinma.univ.trieste.it/nirftc/research/easymesh/easymesh.html.

[72] J. A. Stratton. *Electromagnetic Theory*. McGraw-Hill Inc., 1941.

[73] Per-Olof Persson and G. Strang. A Simple Mesh Generator in MATLAB. *SIAM Review*, 46(2):329–345, 2004. http://wwwmath.mit.edu/~persson/mesh/.

[74] A. A. Obi et al. Modeling Loaded RF Coils using the Method of Moments. *Proc. Intl. Soc. Mag. Reson. Med.*, May 2007.

[75] A. Obi et al. A New Dual-Channel Array Coil for Breast Imaging at 1.5/3.0T. *Proc. Intl. Soc. Mag. Reson. Med.*, May 2005.

[76] Breast Form FAQ: How to measure for a Bra. http://www.eskimo.com/~bloo/bformfaq/measure.html.

[77] Aghogho Obi. A Novel Radio Frequency Coil Design for Breast Cancer Screening in a Magnetic Resonance Imaging System. Master's thesis, Worcester Polytechnic Institute, December 2003.

[78] Bill Doherty. *MicroNote #710: NanoMount Switches for Microwave Applications*. www.microsemi.com.

[79] R.W.Lau S.Gabriel and C.Gabriel. The Dielectric Properties of Biological Tissues: II. Measurements in the frequency range 10 Hz to 20 GHz. *Phys. Med. Biol.*, 41:2251–2269, 1996.

[80] An Internet Resource for the Calculation of the Dielectrical Properties of Body Tissues, 1996. http://niremf.ifac.cnr.it/tissprop/.

[81] NEMA Standards Publication MS. *Determination of Signal-to-Noise Ratio (SNR) in Diagnostic Magnetic Resonance Imaging*. National Electrical Manufacturers Association, 1300 North 17th Street, Suite 1847, Rosslyn, VA 22209, 2001. http://www.nema.org/.

Appendix A

Coil Specification

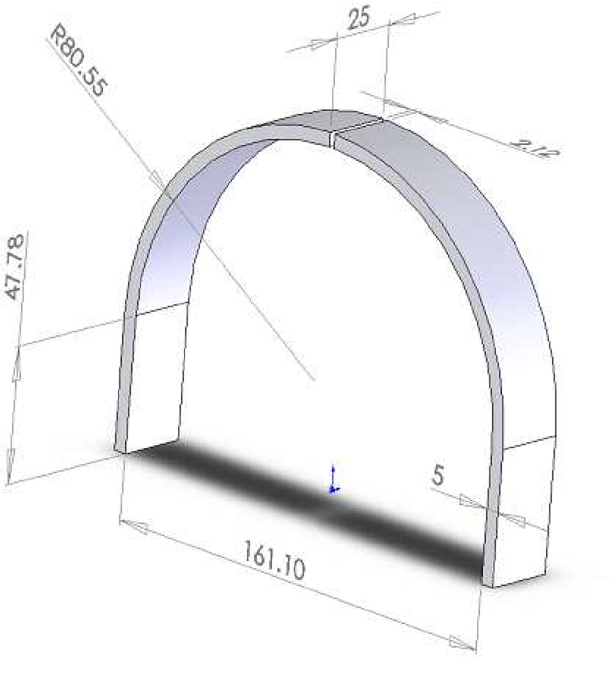

Figure A.1: Dimensions of the strap member of the 4-channel breast coil. All dimensions are in mm

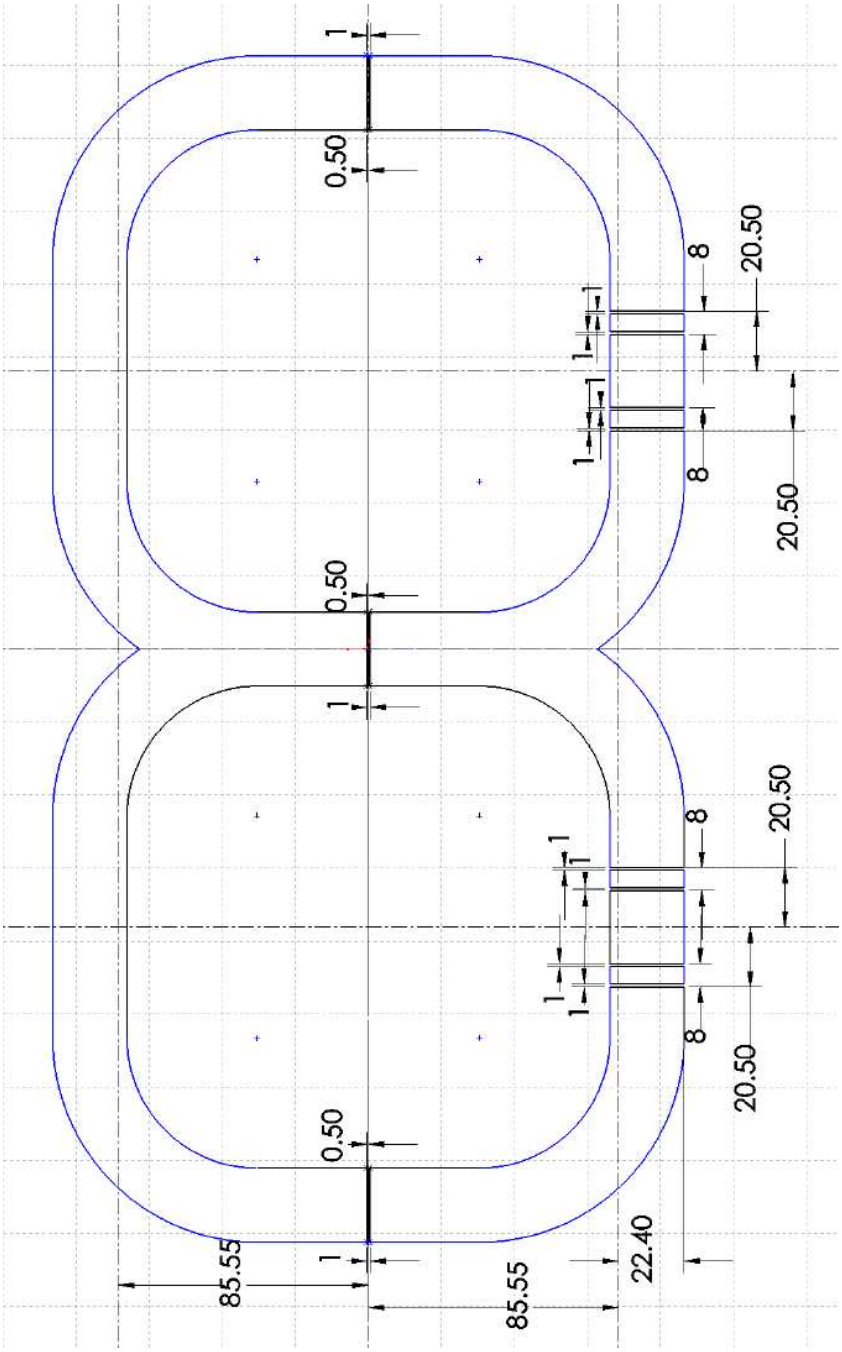

Figure A.2: Dimensions of the combined base ring member of the 4-channel breast coil. All dimensions are in mm

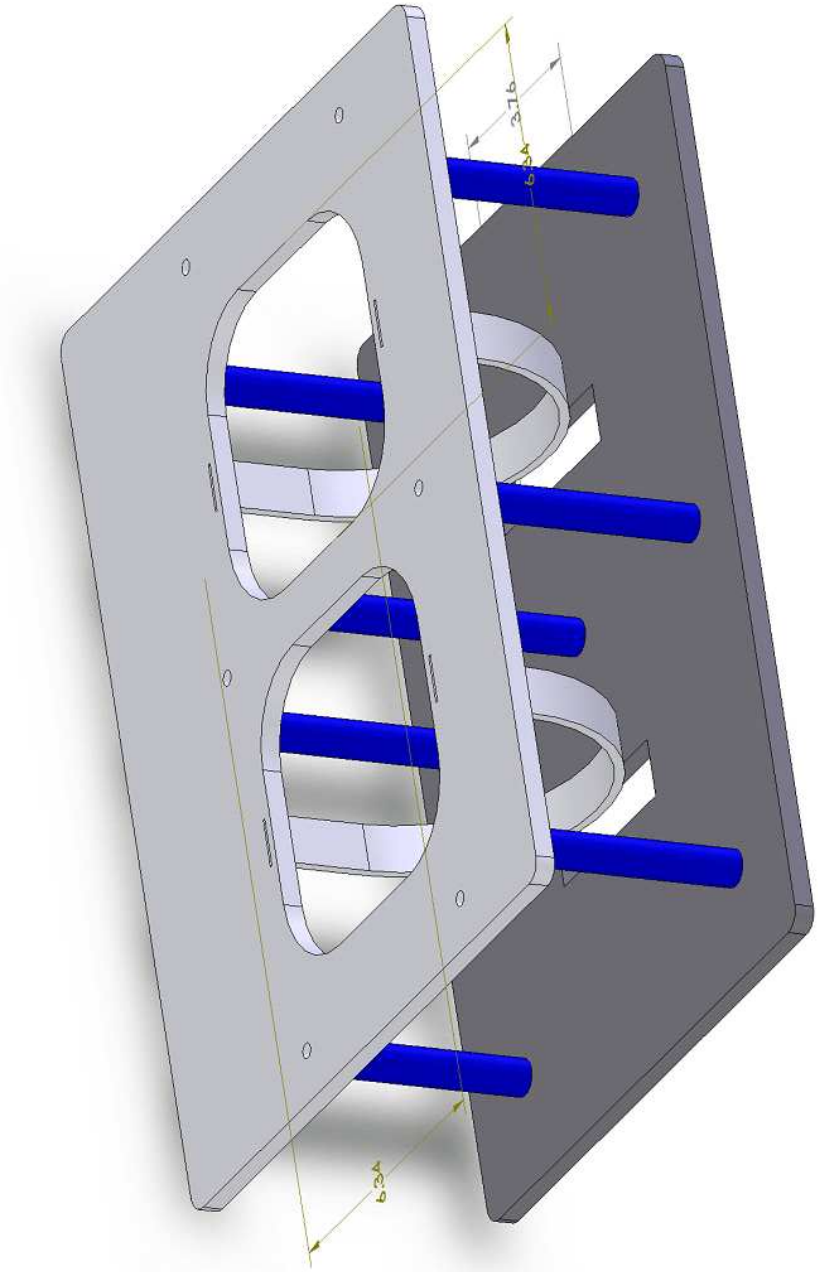

Figure A.3: 4-channel breast coil former.

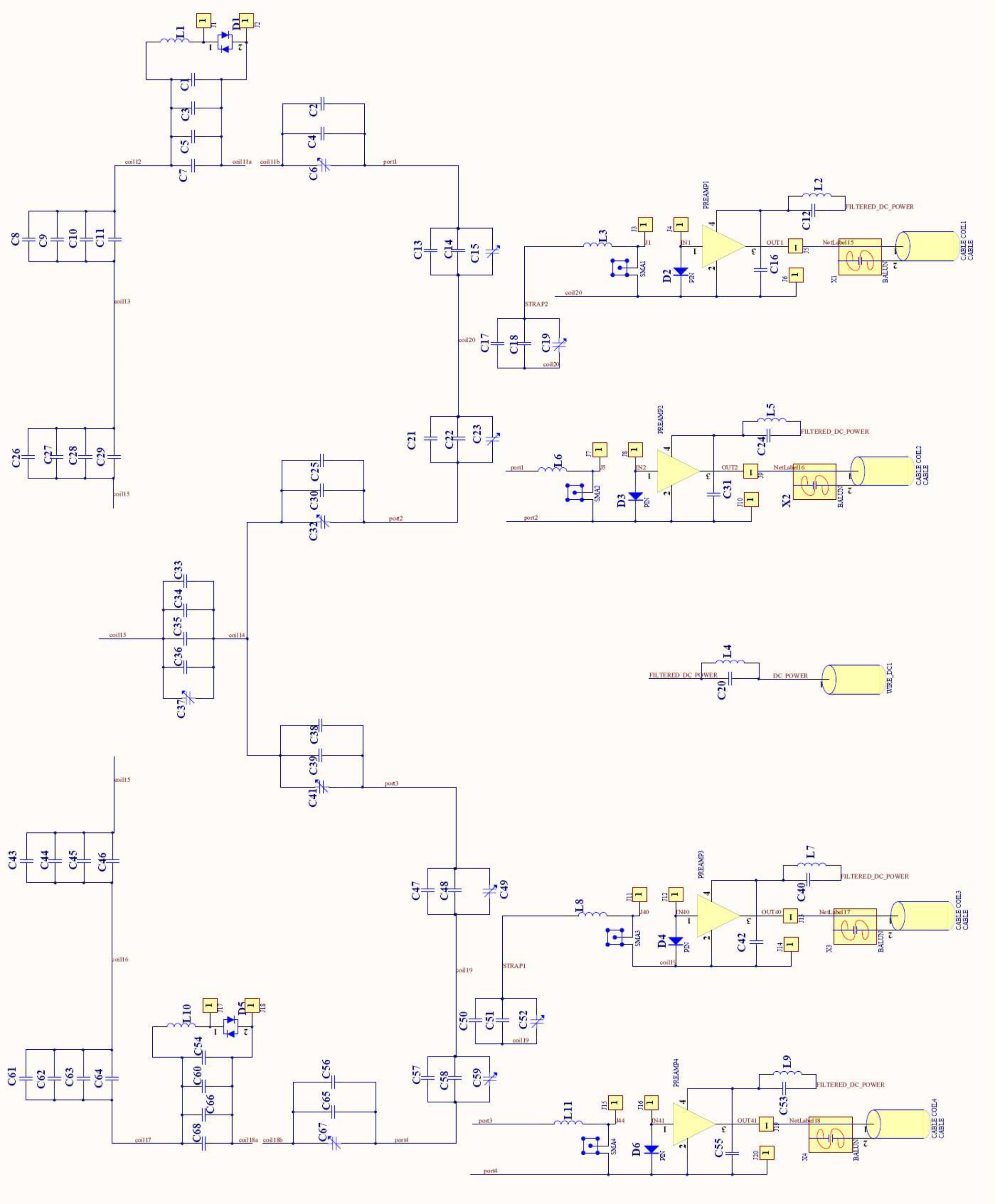

Figure A.4: Circuit schematics of the 4-channel breast coil.

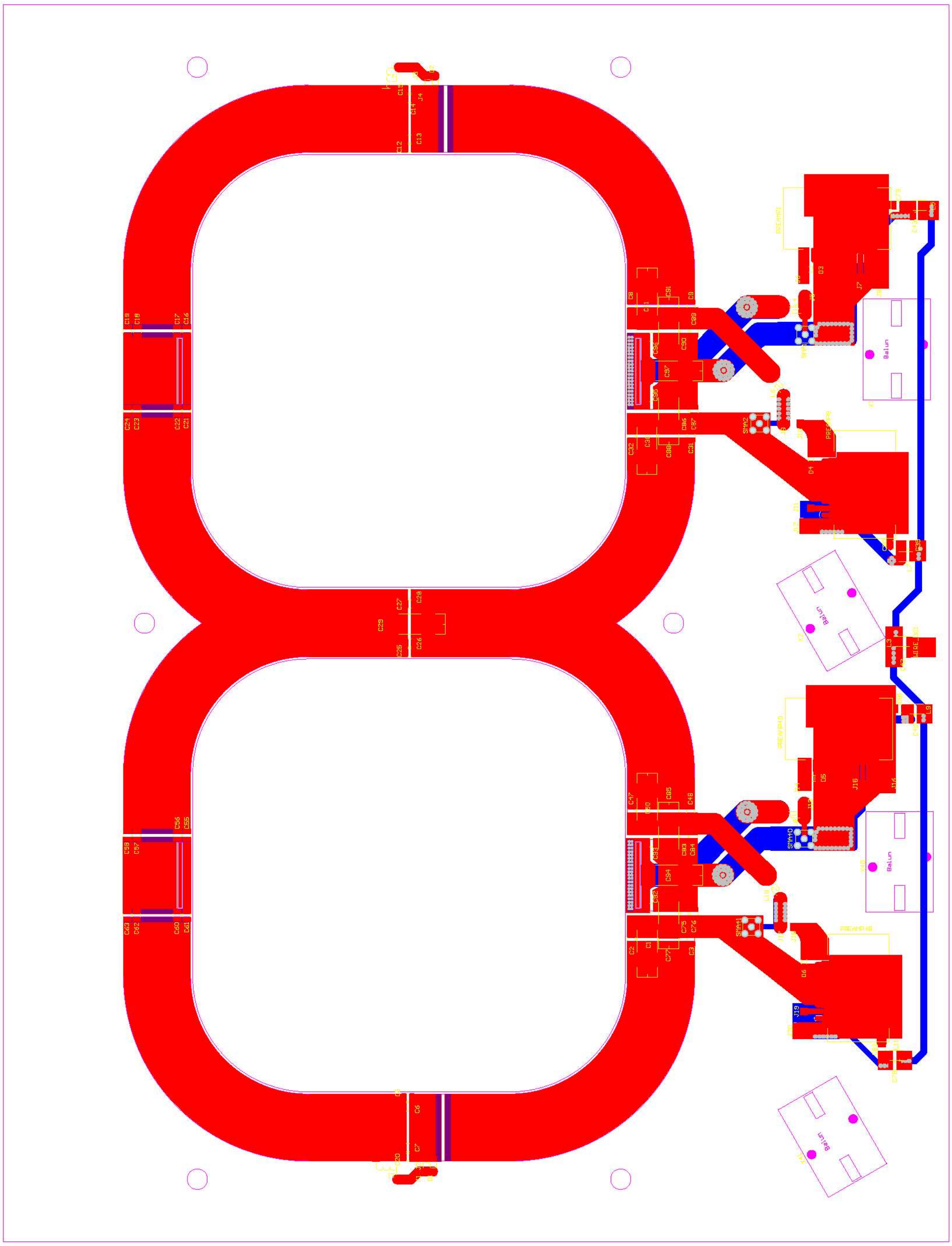

Figure A.5: PCB prototype of the 4-channel breast coil.

Appendix B

Parts List

Table B.1: Component Listing.

Part Number	Description	Qty	Manufacturer
NMAP30	Cap Trimmer (1–30pF)	5	Voltronics
9694	Cap Trimmer (1–50pF)	2	Johanson
V21G 200F	Chip Cap (20pF)	6	Voltronics
V450 121G	Chip Cap (120pF)	4	Voltronics
V219 360J	Chip Cap (36pF)	3	Voltronics
V547 101J	Chip Cap (100pF)	2	Voltronics
V470 130J	Chip Cap (13pF)	2	Voltronics
D334 201 J	Chip Cap (200pF)	4	Voltronics
ATC 161G	Chip Cap (160pF)	2	ATC Corp
1812CS	Inductor (1.8μH)	5	
UMX9989AP	Diode	4	Microsemi
1072	Pin Diode	4	Microsemi
PREAMP–E2V	Preamplifier	4	E2V